Lifetime limiting effects in pre-commercial solid oxide cell devices

Skafte, Theis Løye

Publication date:
2017

Document Version
Publisher's PDF, also known as Version of record

Lifetime limiting effects in pre-commercial solid oxide cell devices

Theis Løye Skafte

February 28^{th}, 2017

Technical University of Denmark *Haldor Topsoe A/S*

Author

Theis Løye Skafte
SOC & Electrification
Research & Development
Haldor Topsoe A/S

Applied Electrochemistry
Department of Energy Conversion and Storage
Technical University of Denmark
E-mail: tlsk@dtu.dk

Supervisors

Johan Hjelm
Senior Scientist, Applied Electrochemistry
Department of Energy Conversion and Storage
Technical University of Denmark
E-mail: johh@dtu.dk

Christopher R. Graves
Senior Scientist, Applied Electrochemistry
Department of Energy Conversion and Storage
Technical University of Denmark
E-mail: cgra@dtu.dk

Peter Blennow
Principal Research Engineer, SOC & Electrification
Research & Development
Haldor Topsoe A/S
E-mail: pebl@topsoe.com

Release date: February 28^{th}, 2017

Version: 1.00

Submitted in partial fulfillment of the requirements for the degree Doctor of Philosophy

Preface

This thesis is submitted to the Technical University of Denmark as partial fulfillment of the requirements for obtaining the PhD degree. The work is based on three years of studies of the solid oxide electrochemical cell technology, with a primary focus on durability and lifetime limiting effects of the devices. The industrial PhD project constituted a collaboration between the Technical University of Denmark and Haldor Topsoe A/S. A four months external research stay at Stanford University, CA, USA, was part of the project.

Theis Løye Skafte, February 28^{th} 2017

Acknowledgments

I am truly grateful for the immense support I have received from a great number of people.

First and foremost, I want to thank my supervisors for countless discussions about solid oxide cells, technology in general and the scientific method; Dr. Christopher Graves, Dr. Peter Blennow and Dr. Johan Hjelm. Your guidance was truly priceless and an irreplaceable part of this project.

At DTU I would especially like to thank Henrik Henriksen for teaching me how to set up and test single cells and for assisting me when I was abroad or elsewhere. A sincere thank you to Heidi Adler Berggren for helping me with practical issues. I would also like to thank Prof. Anne Hauch, Dr. Ming Chen, Prof. Mogens Mogensen, Maria Navasa, Lev Martinez, Dr. Karl Tor Sune Thydén, Dr. Karin Vels Hansen, Prof. Anke Hagen, Dr. Jimmi Nielsen, Dr. Søren Højgaard Jensen, and Søren Koch, for valuable discussions, assistance and advice throughout my time at DTU Energy.

At Haldor Topsoe A/S I would like to thank the entire SOEC groups; Dr. Rainer Küngas, Dr. Søren Primdahl, Dr. Jeppe Rass-Hansen, Tobias Holt Nørby, Thomas Heiredal-Clausen, Torben Nielsen, and Claus Rasmussen. Also a thank you to Allan Pomiklo for manufacturing specialized cells for me, and to Jørgen Hvass for helping me with stack infiltration. I thank many of the people previously at Topsoe Fuel Cell A/S for discussions and advice, especially Dr. Patrick Mühl and Dr. Per Hjalmarsson.

I thank Prof. Jens Nørskov and Dr. Thomas Bligaard at SUNCAT Center for Interface Science and Catalysis for hosting myself and Dr. Christopher Graves during the external research stay at Stanford University. I would like to extend a profound thank you to Prof. William C. Chueh at Stanford for guiding me in the world of synchrotron x-ray photoelectron spectroscopy, and the entire Chueh group for welcoming me and helping me along the way with both practicalities, theory and analysis, especially Zixuan Guan, Michael Machala, Dr. C. B. "BG" Gopal, Dr. Matteo Monti, and Dr. Liming Zhang.

Most importantly I appreciate the support of my family, friends and my girlfriend.

Financial funding

Colleagues and I gratefully acknowledge financial support from Haldor Topsoe A/S, Innovation Fund Denmark, the Danish Agency for Science, Technology and Innovation (grant no. 5176-00001B and 5176-00003B), and Energinet.dk under the projects ForskEL 2014-1-12231 and ForskEL 2015-1-12276.

Abstract

The solid oxide electrochemical cell technology is promising for efficient energy storage, especially when the share of intermittent renewable electricity production is high. The technology is being commercialized in niche markets, but large-scale employment is still hindered by limited durability of the devices. The lifetime limiting mechanisms are addressed in this work.

A general introduction into mechanisms limiting the durability is presented. A database of more than 50 parameters from 150 publications and 1 000 000 hours of accumulated testing was established, and a quantitative analysis of degradation and lifetime was conducted. It is shown that the technology is approaching the official targets required for commercialization, but that work remains to be done.

It is further recognized that targeting niche applications initially will allow for employment of economies of scale, which will bring down costs and facilitate entry into larger markets. Here, we examine electrochemical reduction of CO_2 to CO and one of the main failure mechanisms related to it. Carbon formation on the nickel electrocatalyst can be detrimental to the microstructural integrity of the cell. It is found that the possible operating window is severely limited due to gradients of temperature, gas concentration and overpotential across the electrode. These affects also apply to stack- and system-level, and the results obtained are combined with modeling and stack testing experiences. Thus, on account of this mechanism the possible outlet CO concentration is limited by up to 50% below the thermodynamic carbon deposition threshold based on the inlet temperature, depending on design and operating strategy.

Replacement of the Ni electrocatalyst would increase the stability towards this issue and may improve the robustness in other ways as well. Ceria has been reported as a potential candidate in such endeavors. Thin film electrodes of nickel and ceria are therefore studied as model systems using near-ambient pressure x-ray photoelectron spectroscopy to further the fundamental understanding of the carbon formation mechanism. The reaction occurs further from the thermodynamic threshold on ceria, and fundamental mechanisms for electrochemically driven carbon growth are suggested based on observed adsorbate species.

By infiltrating ceria after degradation has already occurred, the robustness and lifetime of the cells are increased. Complete reactivation of the fuel electrode is achieved after otherwise detrimental failure mechanisms have occurred, such as reactant starvation and carbon formation. Moreover, the degradation of the electrode over the course of nearly 2500 hours is essentially eliminated by infiltrating after microstructural stabilization had occurred. Lastly, the method is scaled up by replicating the positive effects of post-degradation infiltration on an 8-cell stack.

List of included publications

Paper I: Skafte, T. L., Hjelm, J., Blennow, P., and Graves, C. Quantitative review of degradation and lifetime of solid oxide cells and stacks. *EFCF 2016 Proceedings*, (B0501), 8–26 (2016).

Paper II: Skafte, T. L., Graves, C., Blennow, P., and Hjelm, J. Carbon deposition and sulfur poisoning during CO_2 electrolysis in Ni-based solid-oxide-cell electrodes. *In manuscript* (2017).

Paper III: Skafte, T. L., Guan, Z., Machala, M., Gopal, C. B., Monti, M., Martinez, L., Zhang, L., Stamate, E., Sanna, S., Crumlin, E., Bluhm, H., Chueh, W. C., and Graves, C. Electrochemically driven carbon deposition from CO_2 on nickel and ceria electrodes: Reaction and inhibition mechanisms. *In manuscript* (2017).

Paper IV: Skafte, T. L., Hjelm, J., Blennow, P., Høgh, J., & Graves, C. Eliminating fuel electrode degradation and reactivating solid oxide cells and stacks. *In manuscript* (2017).

List of additional publications

Paper V: Navasa, M., Graves, C., Chatzichristodoulou, C., Skafte, T. L., Sundén, B., and Frandsen, H. L. A Three Dimensional Multiphysics Model of a Solid Oxide Electrochemical Cell for Degradation Studies. *In manuscript* (2017).

Paper VI: Navasa, M., Frandsen, H. L., Skafte, T. L., Sundén, B., and Graves, C. Localized Carbon Deposition in Solid Oxide Electrolysis Cells Studied by Multiphysics Modeling. *In manuscript*, (2017).

Comments on my contribution to publications

Paper I: All of the literature gathering, analysis and the majority of writing.

Paper II: All of the experimental work, analysis and the majority of writing.

Paper III: Majority of the experimental work, all of the analysis and the majority of writing.

Paper IV: Majority of the experimental work, all of the analysis and the majority of writing.

Paper V: Supplied experimental data for the validation of the model.

Paper VI: Supplied experimental data for the validation of the model and provided minor input to the analysis.

Contents

1 Introduction

It was Svante Arrhenius who first proposed in 1896 that human activity could lead to climate change [1]. The occurrence of the phenomenon has since then been established as "extremely likely" by modern climate science [2]. Current weather anomalies with extremes in temperature and precipitation are considered early warning signs of climate destabilization, and one threshold towards high-risk scenarios was crossed already in mid-2015 (400 ppm carbon dioxide, CO_2 [3]). The consequences for all living beings will likely be catastrophic; increased social conflict, species extinction, loss of ecosystems and so on. The monetary costs for the human economy are expected to far exceed the cost of curbing the crisis [4].

Fortunately, the majority of nations and industries have realized the costs as well as the new opportunities. The problem can be solved by applying the right technologies. The cost of renewable electricity drops off exponentially with time, and the cost of solar power, for instance, has been shown to drop by 21% for each doubling of cumulative installed capacity [5]. Solar power is already cheaper than new fossil fuel capacity in more than 30 countries [6]. When market forces take over, it will simply become a matter of time before the energy demands of the human race transition into sustainability.

However, there is another piece to the puzzle. The storage of electrical energy is, and will increasingly become, a key issue. Most of our needs have been accustomed to the high energy capacity and flexibility of fossil fuels. We can store increasingly larger amounts of energy in batteries, but fossil fuels are difficult to replace entirely. The convenience of fossil fuels is especially exploited in the industry-, agriculture- and transportation-sectors, which together made up 59% of global greenhouse gas emissions in 2010 [7]. Ideally we would continue using our current infrastructure and fossil fuels, but without the harmful emissions of greenhouse gases.

One potential strategy to realize such a scenario is by recycling the CO_2 that we emit in a smaller loop than how nature does it [8]. This would require capturing the gas from point sources at first, and later from air [9]. By sequestering CO_2 captured from air we would decrease the already too high CO_2 content in the atmosphere. It is not unrealistic to assume that this will be necessary in the long term once we have crossed the thresholds for what is known as "very high

risks"-scenarios. Now, instead of carbon-sequestration as usually discussed [10], we would rather recycle CO_2 into storable, useful fuel. Unknown to many, this is actually possible with current technology.

There are a lot of potential technologies capable of bridging the gap between electrical and chemical energy. The solid oxide cell (SOC) is noteworthy, since it has high theoretical efficiency and many potential applications. It is capable of electrochemically converting water into hydrogen (H_2) and CO_2 into carbon monoxide (CO) [11, 12]. In fact, it can do both simultaneously during so-called co-electrolysis. In the process of doing so, the device requires electricity. However, as established earlier, there will likely be an excess of electricity in the near future, and a desire to convert that power into storable fuel. Lastly, the produced CO and H_2 can be converted into hydrocarbons or alcohols by means of Fischer-Tropsch and related processes [13, 14], the H_2 can be used alone to upgrade biogas [15, 16], or the CO can be used alone in the chemical industry. The electrolysis process strips oxygen-ions from H_2O and CO_2, producing pure oxygen on the other side of the cell. Clean, silent production of oxygen is attractive in military operations or during interplanetary space exploration [17, 18].

SOCs work well today, but large-scale commercialization has not occurred. As will be discussed during this dissertation, the device does not fulfill the lifetime required, i.e. it breaks down before a profit is made. The lifetime requirement can be lowered by decreasing the capital cost of the device (the operational cost is controlled by gas and electricity prices), or by increasing the value of the final product. A higher output value relative to the input value can be achieved by increasing the efficiency towards the theoretical maximum or by increasing the lifetime. In order to increase lifetime, the technical mechanisms responsible for degradation or complete failure of the device must be identified and addressed.

An alternative approach would be to tailor the product to a specific market. Customers with unconventional requirements currently unmet by other technologies are willing to pay more. Such niche markets can be considered shortcuts to market penetration. Once a revenue stream has been established, further research and development can be funded - now by the industry rather than by the government. It is a well-known phenomenon in any development of products or technologies, e.g. the aforementioned solar panels for which market forces are now taking over.

Here, we will investigate the technical issues related to one such niche market, namely the production of pure CO for the specialty chemicals industry. Industrial production of CO is highly localized at large plants and the gas is then transported by tube-trailer to the destination. Unfortunately, CO is an extremely dangerous gas, toxic to humans and difficult to detect. This raises the safety requirements and thus also the cost of transportation. Since SOCs are highly modular, a CO-producing SOC system can be custom-built to the desired specifications at

the location. This eliminates the transportation risks and costs, and adds the security of self-sufficiency. Thus, SOCs are cost-competitive compared to the traditional production method within this market. However, to open up other, larger markets, an improvement in the lifetime of the devices is required.

1.1 Scope of thesis

The objective of this dissertation is to investigate the technical issues currently hindering a widespread employment of the technology. High cost is the overall limitation to commercialization, and this can be overcome by lowering fabrication costs (raw materials, labor, system complexity) or by increasing the value output of the product. The latter can in turn by addressed by increasing efficiency or lifetime, and this is the route chosen in this project.

1.2 Outline

The thesis will present findings in a top-down and then a bottom-up approach. Starting with a general overview, we thereafter zoom in on a specific utilization strategy and the related issues on cell level. To understand and solve the problems we zoom even further in and study the very surface of the relevant materials in model cells. Lastly, we zoom back out, and will attempt to apply the newly acquired knowledge to increase the lifetime of the devices on cell and even stack level. Here follows a more detailed outline of the thesis.

First, a brief introduction to the subject matter and the main techniques employed is given. This is followed by a general study of degradation mechanisms and lifetime in chapter 2, where more than 150 long-term cell and stack tests published in literature were analyzed. Thus, data from more than 1 000 000 cumulative test hours is extracted and quantified. This investigation was carried out to understand the current status of the technology and the main technical lifetime-limiting effects.

Next, we turn our attention to a specific niche case, which has a promising commercial perspective. One of the main technical obstacles preventing the realization of this business case is addressed in chapter 3, a critical failure mechanism causing the device to break down. Under certain operational conditions carbon will form on the electrocatalyst, Ni, in the electrode. An *operando* technique was developed capable of reproducibly detecting the operating conditions which caused cell failure on account of this specific mechanism. Attempts at preventing carbon

formation failed, but the newly obtained knowledge can be used to optimize the efficiency and thereby increase the value-output of the device.

A more fundamental understanding was required to solve the problem. In chapter 4 the elementary reactions of carbon formation were examined on different model electrodes. A collaboration with William C. Chueh and his group at Stanford University was initiated and the work was carried out during an external stay at Stanford. This furthered the understanding of how ceria inhibits the formation of carbon in an operating cell, compared to nickel.

Lastly in chapter 5 we employ the well-known technique of wet infiltration in a novel way so as to increase lifetime instead of enhancing initial performance. Reactivating, or repairing, the electrode in this manner proved to be promising. We were able to mitigate long-term generic degradation as well as reactivate cells after specific failure mechanisms had occurred, e.g. carbon formation. The method was scaled up to stack level with similar promising results.

1.3 The solid oxide cell

The SOC is an electrochemical device capable of converting chemical energy into electrical energy or vice verca. It does so by reducing or oxidizing the reactants by means of electrons at high temperature. In this way, it is possible to oxidize gaseous H_2 (eq. 1.1) or CO (eq. 1.2) into H_2O or CO_2, respectively, and in the process of doing so, force electrons to run in an external circuit, powering a load. When operating the device in this mode, it is called a solid oxide fuel cell (SOFC). In practice, the input is a gas with high energy content, H_2 or CO, and the main desired output is electricity, as well as oxygen and heat. The device can also be run in reverse, which is called a solid oxide electrolysis cell (SOEC). The input is then a gas with lower energy content, H_2O or CO_2, and electricity and heat, and the output is a gas with higher energy content, H_2 or CO. The basic working principles for both modes of operation are illustrated in Fig. 1.1.

$$H_{2(g)} + \frac{1}{2}O_{2(g)} \rightleftharpoons H_2O_{(g)} \qquad \text{(eq. 1.1)}$$

$$CO_{(g)} + \frac{1}{2}O_{2(g)} \rightleftharpoons CO_{2(g)} \qquad \text{(eq. 1.2)}$$

The device works by separating a positive and a negative electrode with an electron blocking electrolyte. As the name indicates, all components in a SOC are

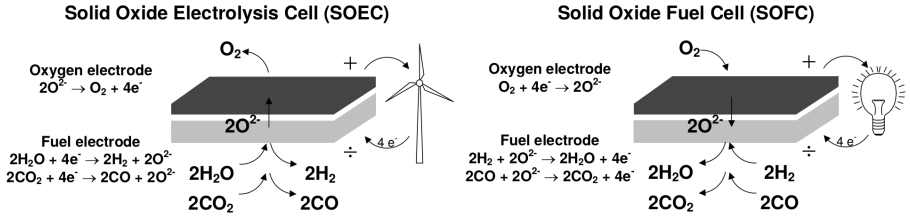

Figure 1.1: The basic working principles of a SOEC and a SOFC. Reproduced with permission from Ebbesen et al. [19]. Copyright 2013, The Electrochemical Society.

solid and the electrolyte only allows oxide ions to pass. Thus, the reduction can take place in one electrode and the oxidation in the other.

When a potential difference is applied between the two electrodes, oxide ions are produced by reduction of the species in the reducing electrode (also known as the negative electrode or as it will be called henceforth, the fuel electrode), as exemplified with the CO/CO_2-case in eq. 1.3. These ions are then forced through the electrolyte on account of the potential difference. When they reach the other side, they combine to form oxygen in the oxidizing electrode (also known as the positive electrode or as it will be called henceforth, the oxygen electrode), as shown in eq. 1.4.

$$CO_{2(g)} + 2e^- \rightleftharpoons CO_{(g)} + O^{2-} \qquad \text{(eq. 1.3)}$$

$$O^{2-} \rightleftharpoons \frac{1}{2}O_{2(g)} + 2e^- \qquad \text{(eq. 1.4)}$$

1.3.1 Thermodynamics

The energy, or reaction enthalpy (ΔH), required to drive the electrolysis reactions is 248.1 kJ mol^{-1} and 282.5 kJ mol^{-1}, for steam and CO_2 respectively, at 750 °C. The cell is operated at high temperature (500 °C - 900 °C), so it is possible to cover some of the energy demand for the reaction by heat energy ($T\Delta S$), as shown in Fig. 1.2 for SOEC operation with both H_2O and CO_2. The heat energy can be supplied from external sources, or internally from unavoidable Ohmic heating of

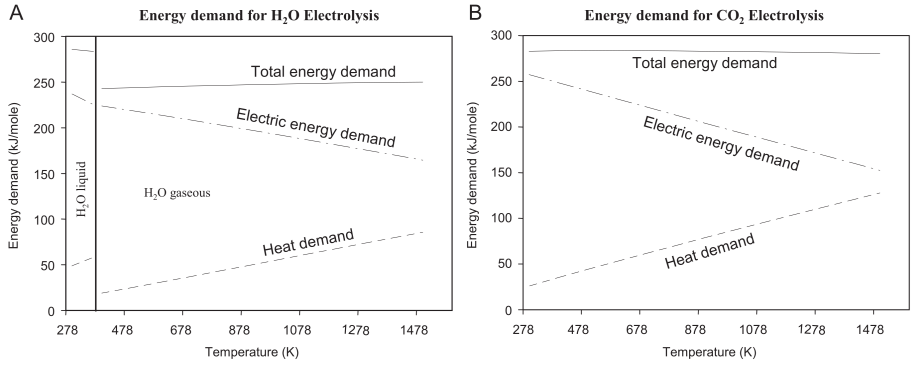

Figure 1.2: The energy demand for A, eq. 1.1, and B, eq. 1.2 at higher temperature. Reproduced with permission from Jensen et al. [20]. Copyright 2007, Elsevier.

the cell components. The rest must be covered by Gibbs free energy (ΔG) and in this case electrical energy. The minimum voltage required for the reactions to proceed at atmospheric pressure is given by the Nernst equation, eq. 1.5, and is also called the open-circuit voltage (OCV).

$$V_0 = \frac{\Delta G}{nF} - \frac{RT}{nF} ln \left(\frac{y_{CO_2}}{y_{CO}\sqrt{y_{O_2}}} \right) \qquad \text{(eq. 1.5)}$$

Where n is the number of electrons (in this case, two), F is Faraday's constant, R is the gas constant, T is the temperature and y_x is the partial pressure of specie x. Thermoneutral operation can be achieved at a specific voltage (V_{tn}), determined by $\frac{\Delta H}{nF}$. Below this voltage (1.285 V and 1.464 V for steam and CO_2, respectively, at 750 °C) the cell will cool and above, it will heat. In practice, thermoneutral operation is achieved when the cooling effect of the endothermic electrolysis operation is exactly balanced by the Ohmic heating.

The efficiency is, as always, defined as the output over the input (eq. 1.6). In this case, the output is the lower heating value of the gas, which is defined as the change in enthalpy, $\frac{\Delta H}{nF}$. So it is seen that the output is the same as V_{tn}. If the heat demand is covered by external or internal sources, the required input is only electricity, i.e. the operating voltage. Thus, it is realized that the electrical efficiency of the device can be high, and if operated thermoneutrally, it can be 100%. This is not merely theoretical, close to 100% electrical efficiency has been

realized in practice when gas leakage, heat loss and electronic leakage across the electrolyte is minimized. The high electrical efficiency is a distinct advantage over other similar technologies.

$$\eta = \frac{E_{out}}{E_{in}} = \frac{E_{gas}}{E_{elec}} = \frac{V_{tn}}{V_{op}} \qquad \text{(eq. 1.6)}$$

Where V_{op} is the operating voltage.

1.3.2 Materials

The cell is usually composed of ceramic materials, each of which is chosen to increase the performance and robustness of the device. The electrolyte is a dense membrane with negligible electronic conductivity, so that the electrons are forced through the external circuit. Typically yttria-stabilized zirconia (YSZ) is used, due to the low electronic conductivity, the high oxygen ion conductivity and the high mechanical robustness.

Both electrodes are porous to allow for gas permeability. The fuel electrode typically consists of a combination of a ceramic and a metallic material (cermet); YSZ and nickel (Ni). Ni supplies the electronic conductivity and the electrocatalytic activity, both of which are required for the fuel electrode reactions to occur. These will then occur where electrons, oxygen ions and gas can meet, i.e. where the Ni-phase, the YSZ-phase and the pore-phase, respectively, are in contact. This line of contact is known as the triple-phase-boundary (3PB) line.

The oxygen electrode typically consists of an oxide material with a perovskite-structure and with mixed ionic- and electronic conductivity (MIEC), such as lanthanum strontium cobalt ferrite (LSCF) in combination with gadolinium-doped ceria (CGO). Since these materials are MIECs, the reactions can take place where two phases meet, the MIEC-phase and the gas-phase. This is called a double-phase-boundary (2PB).

1.3.3 Design

Multiple designs are possible, but today the prevalent one is the planar, square cell design (Fig. 1.3). Other design parameters such as component thicknesses, porosity, cell area and so on, are also important for the performance, robustness and longevity of the cell.

Figure 1.3: From cell to stack to system.

Since the output of a single cell is small, several cells are combined in a stack to increase the power (SOFC-mode) or gas (SOEC-mode) output. In the stack, the two electrodes of two stacked cells must naturally be separated. This is done with a metallic interconnect (IC), which also collects or supplies the electrons to the cell and adds further mechanical robustness. The metal is exposed to exceptionally harsh conditions, i.e. 500 °C - 800 °C and partial oxygen pressure (pO_2) of 10^{-20} atm on one side and 0.21-1 atm on the other. Therefore it is often coated with a thin protective layer to decrease the risk of unwanted reactions. Moreover, the cell can also have other layers, e.g. barrier layers between the components to hinder unwanted solid state reactions there, or contact layers on the electrodes to increase the bonding and electronic conductivity between the cell and the interconnect.

In addition to the many different possibilities for designing the cell, now comes also the design of the interconnect. Furthermore, the cells and interconnects are usually enclosed in some type of container, which adds another dimension of design possibilities. Finally, the enclosed stack is placed in a system with heating, gas pipes, mass-flow controllers and many other components, which increases the complexity and cost. Ultimately, it is evident that the final system is incredibly complex and can be designed in an almost infinite number of ways. As will be seen in chapter 2 this complicates the comparison of different systems, but it also allows for many different applications of the technology.

1.4 Characterization techniques

A large number of characterization techniques were employed during the course of this work. The theory behind three of the main ones are described in the following. Description of experimental approaches in practice are described in more detail for chapter.

1.4.1 Electrochemical impedance spectroscopy

Electrochemical impedance spectroscopy (EIS) is a powerful technique for analysis of performance and degradation of SOCs. In this work the technique is merely used as a tool, so the detailed theory is omitted [21–23]. However, a brief overview follows.

The total resistance of a SOC is often separated into a number of processes and components. In the most simple approach we separate the resistance into Ohmic resistance, R_s, and polarization resistance, R_p. The impedance can then be further reduced into multiple processes, the main ones being gas diffusion ($R_{diff.}$) [24], gas conversion ($R_{conv.}$) [25, 26] and electrochemical reactions ($R_{elec.}$), as seen in eq. 1.7. Each electrode contribute to these processes, and by using EIS we can discern between these processes and learn about which electrode dominates the contribution [27, 28].

$$R = R_s + R_p = R_s + R_{diff.} + R_{conv.} + R_{elec.} \qquad \text{(eq. 1.7)}$$

By applying a periodic sinusoidal current or voltage of small amplitude (mA or mV) we can perturb the steady-state system slightly. By measuring the response of the system as a function of frequency, valuable information can be obtained. The resulting impedance magnitude and phase angle is converted to complex impedance, which is commonly plotted as the real part, Z_{real}, against the negative imaginary part, -$Z_{imag.}$, a so-called Nyquist plot. In Fig. 1.4 an example of such a plot is given, where the contribution of the Ohmic and the polarization resistance has been illustrated. The key output is Z_{real}, which is normalized by area and then called area-specific resistance (ASR) with the units Ω cm^2. Z_{real} can also be plotted against the frequency, in a Bode plot. Processes related to high-temperature SOCs usually occurs within the frequency range 1 mHz - 1 MHz.

Data treatment

The impedance response can then be modeled by a series of equivalent electrical circuit modules in a complex nonlinear least squares fitting routine. This can yield information about the number of processes occurring and the magnitude of the resistance contribution from each process. These are often modeled by a resistor (R) in parallel with a constant phase element (Q), which in a Nyquist plot would produce a depressed semi-circle. The Ohmic resistance of the cell is modeled by a R, in accordance with Ohm's law. An R circuit element will shift Z_{real} on the x-axis, or in other words, the Ohmic resistance of a high-temperature SOC is the real impedance at a frequency of roughly 1 MHz, $R_s = Z_{real}\,(f \rightarrow 1MHz)$.

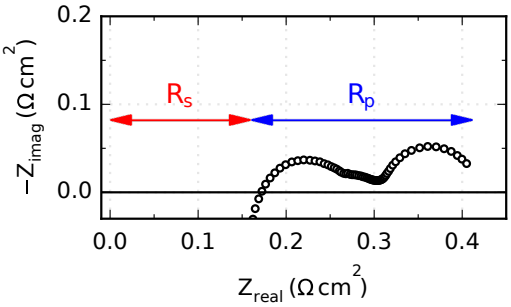

Figure 1.4: Raw impedance data from a SOC tested in CO/CO_2 at 750 °C, separated into Ohmic resistance, R_s, and polarization resistance, R_p.

An inductance element is also used to model the self-inductance of the device or stray-inductance from wires and other auxiliaries. Thus, a very simple model of a full SOC could be represented by a so-called L-R-RQ-RQ-RQ-RQ-RQ model. Such a model fit is illustrated in Fig. 1.5, where each RQ module correspond to one of the processes in eq. 1.7 from either electrode. The fitting error is also shown in Fig. 1.5c, where low relative residuals and a non-systematic variance is desired. More complex models exists, which utilize physical parameters as input [29]. Such state-of-the-art models can thus reveal information about the actual physical properties of the system, e.g. porosity, tortousity, etc. Both types of models are used in chapter 5, and examples are shown in the Supporting Information section of chapter 5.

Distribution of relaxation times (DRT) is a data analysis method which can increase the resolution of the time/frequency-domain [27]. It does so by exploiting that the impedance can be simulated by a sum of infinitesimally small resistor-capacitor modules. It can be used to discern between processes occurring at similar time-scales in the two electrodes. Furthermore, by integration of a DRT peak, the magnitude of the contribution can be estimated. Examples are given in the Supporting Information section of chapter 5. Another useful method for increasing the usefulness of the data is the Kramers-Kronig transformation [30]. Since an inductor mathematically only has an imaginary part, it will not comply with the requirements for the Kramers-Kronig transformation; linearity, causality, finiteness and stability [22]. Therefore, the method can be used to estimate and subtract any stray inductance which has not already been removed by the experimental test-setup. This will considerably increase the accuracy of analyzing the impedance of processes occurring at high frequency, i.e. Ohmic resistance and the electrochemical contribution of the fuel electrode. This is illustrated in

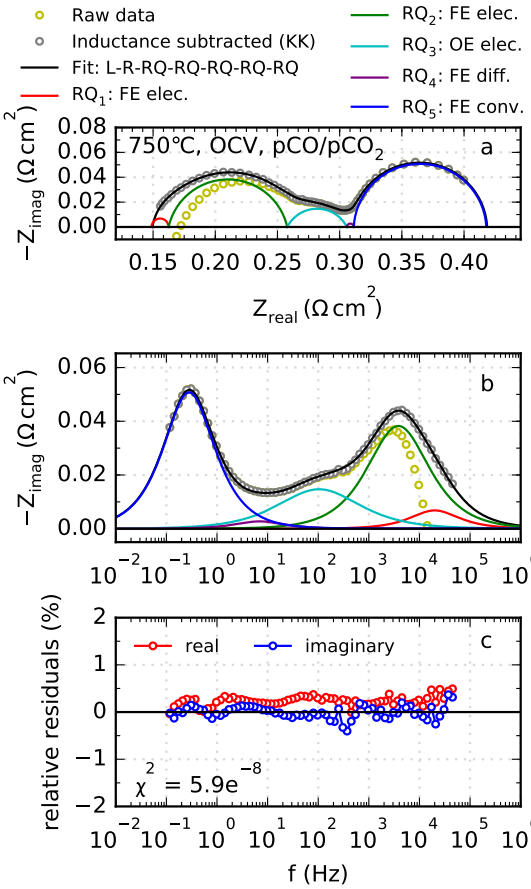

Figure 1.5: An example of area-corrected impedance data and data treatment for a SOC operated at 750 °C, in an $p\mathrm{CO}/p\mathrm{CO_2}$-atmosphere of 0.5/0.5, with no current flowing through the cell (OCV), except that applied periodically by the EIS measurement. a, Nyquist plot where the raw data, the Kramers-Kronig inductance corrected data and the total fit is shown. The most relevant processes of each electrode are also modeled by RQ elements. b, Bode plot. c, relative residuals between the real and imaginary impedance for the data and the fit. KK: Kramers-Kronig, FE: fuel electrode, OE: oxygen electrode, elec.: electrochemical, diff.: diffusion, conv.: conversion.

Fig. 1.5a-b, where the difference for the raw data and the Kramers-Kronig inductance corrected data is seen at high frequency. Kramers-Kronig transformation can also be used to estimate the quality of the data, since it is possible to deduct Z_{real} from $Z_{imag.}$, and vice versa.

Lastly, it is noted that data analysis throughout this work has been carried out with the software package, RavDav [31].

1.4.2 Scanning electron microscopy

With scanning electron microscopy (SEM) it is possible to learn about the microstructure of the cells at the µm-range. This can yield vital information about degradation and failure mechanisms, which are often occurring and visible at this scale. A brief introduction into the theory of how SEM works as well as some practical experiences regarding sample preparation, image acquisition and data analysis is given in the following. A non-traditional way of using the microscope to discern between percolating phases is also described here, as this will be utilized in chapter 5.

Electrons are drawn from an electron source, often tungsten, and accelerated through condenser and objective lenses, scan coils and an aperture before finally hitting the specimen. For more information on the workings of the various components of the microscope, the reader is referred to Chapter 4 in Goodhew et al. [32]. Once the electron beam hits the target, the electrons will interact with the sample material elastically or inelastically, thereby sending off x-rays and Auger-, backscattered- and secondary-electrons. These are converted to a digital image after being detected by specific detectors. Depending on energy and type, the signal will originate from different depths of the material, as illustrated in Fig. 1.6. The interaction volume is thus related to the spatial resolution of the specific signal.

Backscattered electrons (BSE) are incoming electrons that have interacted elastically through Coulombic forces with the nucleus or the surrounding electrons of the sample material and are then returning towards the electron beam and the detectors. Secondary electrons (SE) have interacted inelastically with the atoms of a material once or numerous times and ultimately return towards the detectors.

The total electron yield from a specimen is the sum of BSE and SE. The latter can be further classified into SE of the incident beam (SE1), SE generated from the outgoing backscattered electrons (SE2) and secondary electrons generated by backscattered electrons from the sample surface which hit the pole pieces near the incoming electron beam in the microscope (SE3).

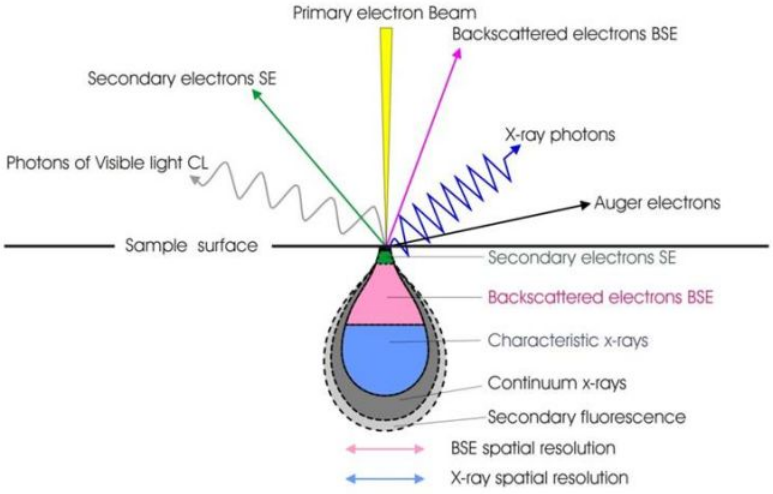

Figure 1.6: The incoming electron beam in a SEM interacts with the sample and the outgoing signal will originate from varying depth and have different spatial resolution. From [33].

The primary microscope employed in this work was a Zeiss Supra 35, equipped with a field emission gun, GEMINI electron-optics, a BSE detector, a lateral SE detector (Everhart-Thornley) and an in-lens SE detector. In addition it also has various other features, e.g. an energy-dispersive x-ray detector, electron backscatter diffraction analysis detector and others.

Electrons returning from the sample surface will be collected by an electrostatic lens and focused and accelerated back up the beam path. The SE in-lens detector is positioned here and will collect the electrons. The setup with the electrostatic lens and the in-lens detector will result in high detection efficiency even for low acceleration voltages [34].

Low-voltage SEM

The method of using low-voltage SEM (LV-SEM) to study percolating Ni was developed by Karl Tor Sune Thydén from DTU Energy [35]. I am thankful that I was so privileged to learn the technique from Karl himself.

In order to study the three phases present in the fuel electrode (Ni, YSZ and pores), one could resort to optical microscopes where a polished cross-section covered with an interference film of Fe_2O_3 [36] will make Ni appear bright, but

these microscopes are limited by their resolution (theoretically ≥ 0.2 µm). Particles and particle necking in the nanometer range will be present, so a resolution of 10-100 nm is necessary. X-ray mapping also has low spatial resolution, as well as low depth resolution. Focused ion beam microscopy can also be used in combination with SEM to distinguish between all three phases at high resolution and in three dimensions, but this technique is so time consuming that statistical conclusions are difficult to draw. The same applies to the technique of transmission electron microscopy. In the middle of the pack lies SEM.

The issue with studying Ni-YSZ cermets using SEM at ordinary acceleration voltages (10-20 kV) is that Ni and YSZ have similar backscatter coefficients (η), which makes distinguishing between the two difficult. Generally, η is considered dependent on number of protons (i.e. which material it is), but actually this is an approximation. It depends on the number of electrons [37]. η is also generally considered independent of acceleration voltage, but only at 5 kV or more. Below 5 kV, the opposite is true [38]. While a regular backscatter detector is not efficient at such low acceleration voltages, a lateral SE detector can pick up the difference between Ni and YSZ.

The main advantage of LV-SEM is that instead of just considering the three phases (Ni, YSZ and pores) as the other microscopy techniques do, with LV-SEM it is possible to characterize the electrode by four components (percolating Ni, non-percolating Ni, YSZ and pores). Percolating Ni can be distinguished as a bright phase in contrast to non-percolating Ni, which will appear dark gray. Other advantages of LV-SEM is increased surface sensitivity due to the reduced irradiated volume, and less charging effects [39].

Sample preparation

The samples are quite delicate, as they consist of porous cermets of materials with quite different physical characteristics. To avoid introducing artifacts from polishing or in other ways altering the sensitive morphology, the samples were mounted under vacuum in epoxy (Struers Epofix). Then the surface of the sample was metallographically grinded with SiC-paper and polished using cloths with diamond abrasive down to 1 µm.

The sample is coated using physical vapor deposition with a conducting 1-15 nm layer of carbon (or gold) in order to avoid charging of the sample. Carbon tape is also used to ensure electrical connection between the sample stage and the conducting carbon layer. Specific for LV-SEM, all of the epoxy must be covered by carbon tape due to the low voltage, and the carbon coating cannot be applied. Before inserting the sample in the microscope, it is cleaned with N_2 so as to remove dust particles.

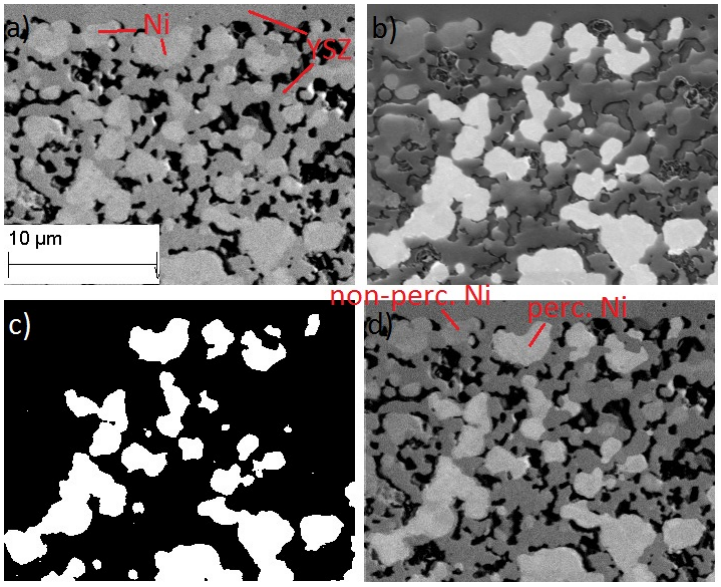

Figure 1.7: The same area imaged by a) the lateral SE detector and b) the in-lens detector. In c) a binary image from the in-lens detector is seen and in d) a combination of images from the lateral SE detector and the in-lens detector.

Image analysis

As can be seen in Fig. 1.7a, in an image taken with the lateral SE detector, it is possible to discern between three phases, Ni, YSZ and pores. As seen in Fig. 1.8a, the peaks of YSZ and non-percolating Ni are rather close in intensity, though, so putting a threshold between these two intensity peaks is difficult and thus quantification using a threshold-method is impossible. With the in-lens detector, Fig. 1.7b, it is also possible to distinguish percolating Ni. As seen in Fig. 1.8b, the intensity peak for percolating Ni is quite easy to threshold and thus, quantify. It is, however, now difficult to discern between YSZ and non-percolating Ni. In Fig. 1.7c, the binary image created by setting a threshold in the minimum between the two peaks in the histogram is seen. This can be overlaid on the image from the lateral SE detector and a visualization of the four phases is possible. However, this does not help with the quantification issue regarding non-percolating Ni and YSZ, as described above.

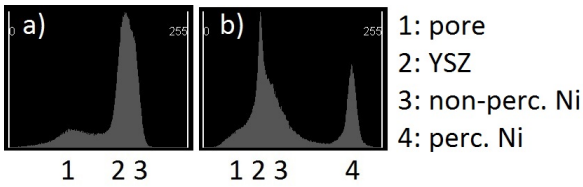

Figure 1.8: Histograms of the images in Fig. 1.7 from a) the lateral SE detector and b) the in-lens detector. The intensity peaks or shoulders have been labeled.

1.4.3 X-ray photoelectron spectroscopy

Instead of probing the surface with electrons, we can also use x-rays. This can reveal radically different information due to the difference in interaction with the molecules. Furthermore, as will be described, we will be able to examine the first couple of atomic layers of surfaces, thereby unlocking another scale for our complete analysis.

While electrons interact elastically or inelastically, in x-ray photoelectron spectroscopy (XPS), the x-rays will be absorbed by the molecule or atom and a photoelectron is emitted. The method is largely non-destructive, and requires no modification of the surface. The kinetic energy (KE) of the emitted photoelectron can be determined from the incoming x-ray ($h\nu$) and the binding energy (BE) of the electron with eq. 1.8.

$$E_{KE} = h\nu - E_{BE} \qquad \text{(eq. 1.8)}$$

The BE is characteristic of the specific atom and orbital from which the electron is emitted. Thus, in simple terms it can be said that by knowing the incident energy and measuring the energy of the outgoing particle, the elemental surface chemistry can be determined.

The BE is referenced to the Fermi level of the sample, E_F, and the KE is referenced to the vacuum level of the electron energy analyzer (Fig. 1.9). Moreover, the work function of the analyzer, ϕ_{ana}, must also be included in eq. 1.8, but in practice it is intrinsically included by routine calibration. In conventional XPS, the sample surface and the analyzer are Fermi-equilibrated, but in chapter 4 we will be applying an electrical bias to the sample. As will be shown, this will shift the Fermi level for insulator- and semiconductor-materials, but not for conductors as charge does not build up.

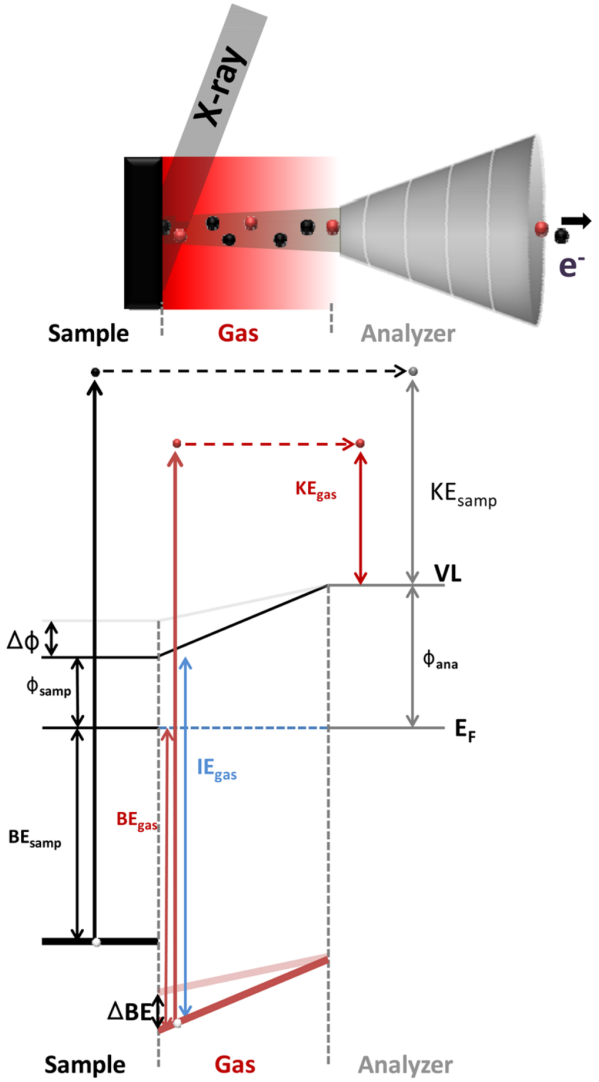

Figure 1.9: Illustration of the XPS system and schematic drawing of energy levels for a solid sample, gas atmosphere and an analyzer. An x-ray beam hits the sample surface at an angle and photoelectrons are emitted, transmitted through a gas atmosphere, and collected by an electron energy analyzer. Binding energy, BE_{samp}, is referenced to a fixed Fermi level, E_F, and the kinetic energy of the sample, KE_{samp}, is referenced to a fixed vacuum level (VL). Reproduced with permission from Axnanda et al. [40]. Copyright 2013, American Chemical Society.

Usually the BE is calibrated to the electrons emitted from the 1s orbital of carbon (C 1s). Since samples are almost always exposed to atmospheric air during preparation, adventitious carbon will be deposited and will give a strong BE peak at 284.8 eV. Again, the work carried out in chapter 4 is unconventional as we were studying carbon deposition and could not use C 1s as the reference. Instead the BE was calibrated to a gold (Au) reference.

The signal depth is strongly dependent on KE, and less so on the material. Even though the incoming photons can penetrate relatively deep into the solid sample, the emitted electrons are easily scattered. Effectively the signal depth is thus only a few atomic layers [41], which makes XPS highly surface sensitive. This makes the technique especially relevant for (electro-)catalysis as the majority of reactions occur at the surface of the materials. However, the surface must be directly available for both the incoming and outgoing signal, so porous electrodes are difficult to study. In this work we have employed model electrodes as described in more detail in chapter 4.

The electrons are also scattered by gas between the sample and the analyzer. To obtain a useful signal, conventionally this is solved by pumping the sample chamber to ultra-high vacuum ($<10^{-8}$Torr). However, in (electro-)catalysis the surface reactions are dependent upon the density of gas molecules available as reactants. By moving the electron analyzer close to the sample, the number of gas molecules scattering the signal can be minimized. Since the analyzer must still be kept at ultra-high vacuum, this requires a complex differential pumping system. This approach is known as near-ambient pressure XPS (NAPXPS), although the current technology still only allows for a pressure of a few Torr (1 Torr = 1.33 mbar).

The conventional x-ray source is aluminum or magnesium, placed in laboratory x-ray tubes. The metals are hit by high-energy electrons and inner-shell electrons are emitted. The electron vacancies are quickly filled by electrons from outer shells, transitions that will emit x-rays. However, to increase the brilliance, polarization, wave-length tunability and to obtain the possibility of x-ray pulses, one can utilize synchrotron facilities. By accelerating electrons radially at relativistic speeds using bending magnets, electrons will emit x-ray radiation of sufficiently high quality. With extremely precise insertion devices (undulators and wigglers) the x-ray quality can be even further optimized. Thus, in a short amount of acquisition time, high-quality data can be gathered. This is required to discern between closely spaced BE peaks. Furthermore, the spatial resolution is high (compared to laboratory sources), and the BE can be tuned precisely.

Data treatment

The desired KE spectrum is scanned and the intensity of collected photoelectrons is measured throughout. The output is a plot of KE or BE against the intensity, as seen in Fig. 1.10. Each specific element with a particular electron composition present on the surface will yield a peak in intensity at the characteristic BE. After calibration to a reference BE (Au in this case), the peak can be fitted to quantify the intensity, full-width-half-maximum (FWHM) and peak BE.

In chapter 4 we will be using synchrotron-assisted *operando* NAPXPS to study carbon formation on model SOCs. As hinted at above, this approach is at the very forefront of surface science and electrocatalysis.

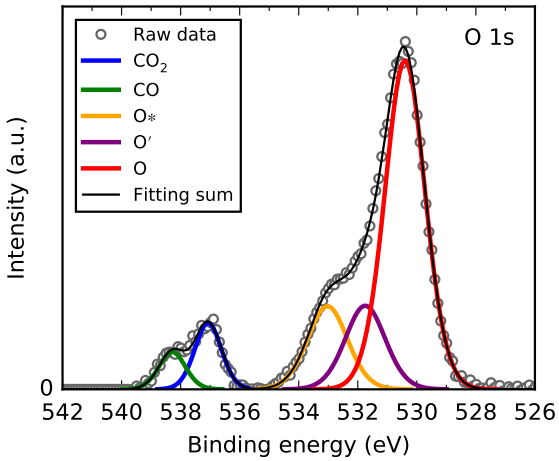

Figure 1.10: XPS spectrum of O 1s. The raw data (excl. background and after calibration to Au) is fitted to several peaks, each one representing a characteristic element or molecule.

1.5 References

1. Arrhenius, S. On the influence of carbonic acid in the air upon the temperature of the ground. *Philosophical Magazine Series 5* **41,** 237–276 (Apr. 1896).
2. Stocker, T. *et al.* in *Climate Change 2013 - The Physical Science Basis* 1–30 (Cambridge University Press, 2015).
3. Dlugokencky, E. & Tans, P. *Recent Global CO_2 from NOAA/ESRL.* 2016.
4. Ackerman, F. & Stanton, E. A. *NRDC: The Cost of Climate Change* tech. rep. May (2008).
5. Cellere, G. *et al. International Technology Roadmap for Photovoltaic* tech. rep. (2015).
6. Bleich, K. & Guimaraes, R. D. *Renewable Infrastructure Investment Handbook: A Guide for Institutional Investors* tech. rep. December (2016).
7. Edenhofer, O. *et al. IPCC, 2014: Summary for Policymakers* tech. rep. (2014).
8. Graves, C., Ebbesen, S. D., Mogensen, M. & Lackner, K. S. Sustainable hydrocarbon fuels by recycling CO_2 and H_2O with renewable or nuclear energy. *Renewable and Sustainable Energy Reviews* **15,** 1–23 (Jan. 2011).
9. Lackner, K. S. Capture of carbon dioxide from ambient air. *European Physical Journal: Special Topics* **176,** 93–106 (2009).
10. Metz, B., Davidson, O., de Coninck, H., Loos, M. & Meyer, L. *IPCC, 2005: IPCC Special Report on Carbon Dioxide Capture and Storage* tech. rep. (2005).
11. Isenberg, A. Energy conversion via solid oxide electrolyte electrochemical cells at high temperatures. *Solid State Ionics* **3-4,** 431–437 (Aug. 1981).
12. Ebbesen, S. D. & Mogensen, M. Electrolysis of carbon dioxide in Solid Oxide Electrolysis Cells. *Journal of Power Sources* **193,** 349–358 (Aug. 2009).
13. Jensen, S. H., Høgh, J. V., Barfod, R. & Mogensen, M. B. High temperature electrolysis of steam and carbon dioxide. *Risø International Energy Conference* **1405,** 204–215 (2003).
14. Frost, L. High temperature co-electrolysis of steam and carbon dioxide to produce synthesis gas for Fischer Tropsch synthetic fuels. *2008 AIChE Spring National Meeting, Conference Proceedings* (2008).
15. Ebbesen, S. D., Hansen, J. B. & Mogensen, M. Biogas Upgrading Using SOEC with a Ni-ScYSZ Electrode. *ECS Transactions* **57,** 3217–3227 (Oct. 2013).

16. Hansen, J. B. Solid oxide electrolysis - a key enabling technology for sustainable energy scenarios. *Faraday Discuss.* **182,** 9–48 (2015).

17. Sridhar, K. & Vaniman, B. Oxygen production on Mars using solid oxide electrolysis. *Solid State Ionics* **93,** 321–328 (1997).

18. Hartvigsen, J., Elangovan, S. E., Elwell, J., Larsen, D. & Clark, L. Development of solid oxide electrolysis for oxygen production from mars atmosphere carbon dioxide. *EFCF 2016 proceedings,* A1403 (2016).

19. Ebbesen, S. D. & Mogensen, M. Kinetics of Oxidation of H_2 and Reduction of H_2O in Ni-YSZ based Solid Oxide Cells. *ECS Transactions* **50,** 167–182 (Apr. 2013).

20. Jensen, S. H., Larsen, P. H. & Mogensen, M. Hydrogen and synthetic fuel production from renewable energy sources. *International Journal of Hydrogen Energy* **32,** 3253–3257 (Oct. 2007).

21. Barsoukov, E. & Macdonald, J. *Impedance Spectroscopy: Theory, Experiment, and Applications* (Wiley, 2005).

22. Orazem, M. E. & Tribollet, B. *Electrochemical impedance spectroscopy* (Wiley, 2008).

23. Lasia, A. *Electrochemical Impedance Spectroscopy and its Applications* (Springer, 2014).

24. Primdahl, S. Gas Diffusion Impedance in Characterization of Solid Oxide Fuel Cell Anodes. *Journal of The Electrochemical Society* **146,** 2827 (1999).

25. Primdahl, S. & Mogensen, M. Gas Conversion Impedance: A Test Geometry Effect in Characterization of Solid Oxide Fuel Cell Anodes. *Journal of The Electrochemical Society* **145,** 2431–2438 (July 1998).

26. Jacobsen, T., Hendriksen, P. V. & Koch, S. Diffusion and conversion impedance in solid oxide fuel cells. *Electrochimica Acta* **53,** 7500–7508 (2008).

27. Schichlein, H. & Ivers-tiffe, E. Deconvolution of electrochemical impedance spectra for the identification of electrode reaction mechanisms in solid oxide fuel cells. *Journal of Applied Electrochemistry* **32,** 875–882 (2002).

28. Ivers-Tiffee, E., Leonide, A., Schichlein, H., Sonn, V. & Weber, A. in *Fuel Cell Science and Engineering* (eds Stolten, D. & Emonts, B.) 439–467 (2012).

29. Graves, C. & Hjelm, J. Advanced impedance modeling of solid oxide electrochemical cells. *EFCF 2014 proceedings,* B1203 (2014).

30. Boukamp, B. A. A Linear Kronig-Kramers Transform Test for Immittance Data Validation. *Journal of The Electrochemical Society* **142,** 1885 (1995).

31. Graves, C. *RAVDAV data analysis software, version 0.9.8* 2015.

32. Goodhew, P. J., Humphreys, J. & Beanland, R. *Electron microscopy and analysis* 66–121 (2000).

33. Www.gla.ac.uk. *Scanning Electron Microscopy - Imaging Spectroscopy and Analysis Centre*

34. Ackermann, J. *Manual for the SUPRA (VP) and ULTRA Scanning Electron Microscopes. SmartSEM V. 05.00* (2005).

35. Thyden, K. *Microstructural degradation of Ni-YSZ anodes for solid oxide fuel cells* Ph.D. thesis (Technical University of Denmark, 2008).

36. Simwonis, D., Tietz, F. & Stöver, D. Nickel coarsening in annealed Ni/8YSZ anode substrates for solid oxide fuel cells. *Solid State Ionics* **132,** 241–251 (2000).

37. Donovan, J. J., Pingitore, N. E. & Westphal, A. Compositional Averaging of Backscatter Intensities in Compounds. *Microscopy and Microanalysis* **9,** 202–215 (June 2003).

38. Joy, D. *Compiled experimental electron scattering data* tech. rep. (2006).

39. Cazaux, J. About the role of the various types of secondary electrons (SE1; SE2; SE3) on the performance of LVSEM. *Journal of microscopy* **214,** 341–7 (June 2004).

40. Axnanda, S. *et al.* Direct Work Function Measurement by Gas Phase Photoelectron Spectroscopy and Its Application on PbS Nanoparticles. *Nano Letters* **13,** 6176–6182 (Dec. 2013).

41. Briggs, D. & Seah, M. P. *Practical surface analysis: by auger and x-ray photo-electron spectroscopy* (Wiley, 1983).

2 Degradation mechanisms and lifetime

One of the main obstacles for large-scale commercialization of the technology has been identified; lifetime. A vast amount of mechanisms occurring in the cells and stacks cause degradation or failure, and many of these will be introduced in this part of the dissertation. The limited lifetime is here confirmed to be an issue by quantifying the amount of time that single cell and stack tests typically run for, as reported in literature. The complexity of SOC systems causes great variance in tests conducted, making it difficult to pinpoint specific mechanisms that hinder commercialization in general. For subsets of systems and operating modes, the exact mechanisms can more easily be identified and mitigated. This type of focus will be applied in chapter 3 and chapter 4. However, despite the difficulty in standardizing testing, there is no reason that the reporting of tests is not standardized. This topic will also be addressed in this chapter.

The following pages are based on the 1^{st} publication: Quantitative review of degradation and lifetime of solid oxide cells and stacks.

2.1 Abstract

A comprehensive review of degradation and lifetime for solid oxide cells and stacks has been conducted. Based on more than 50 parameters from 150 publications and 1 000 000 hours of accumulated testing, this chapter presents a quantitative analysis of the current international status of degradation and lifetime in the field. The data is used to visualize specific trends regarding choice of materials, operating conditions and degradation rates. The average degradation rate reported is decreasing and is quickly approaching official targets. The database is published online for open-access and a continued updating by the community is encouraged. Furthermore, the commonly reported test parameters and degradation indicators are discussed. The difficulty in standardizing testing due to variations in cell and stack design, materials and intended purpose of the system is acknowledged. A standardization of reporting of long-term single-cell- and stack-tests is proposed.

2.2 Introduction

To reach market penetration for the solid oxide cell technology, three aspects are often mentioned as deciding factors: performance, lifetime and costs [1]. These are naturally interlinked, but in truth the situation is far more complicated. On the most fundamental level only one single question needs to be considered, but the answer is not straightforward: Is the value gain higher for this technology compared to an alternative technology? The gain depends on the application, but it will either be electricity (SOFC) or a gas (SOEC). The value of this product depends on the price of electricity and gas in that given situation, but also on other factors, which are relevant for that specific application. The system is thus economically viable if either the product price is higher than the cost of obtaining the product and lower than what the alternative technology can deliver, or if the technology can deliver certain advantages which other, perhaps cheaper, technologies cannot. It quickly becomes complex to consider the cost paid to obtain the product, as such cost analysis would not only need to include fuel gas, raw materials, operation costs, production machinery, research instruments, labor and so forth in the calculations, but also technical parameters such as initial performance (or efficiency), degradation and lifetime of the system.

To assess how far the technology is from a commercial breakthrough and thereby justify further funding, both economic and technical studies are necessary. These are naturally strongly interrelated and both can change the intended business case. Basically, any action taken to improve the business case must be held up against all other possibilities and the one that brings the most value must be prioritized. The present study attempts to map out the current international status of the solid oxide cell technology regarding three of the main technical aspects, namely the initial performance, the degradation, and the lifetime of cells and stacks.

This study was carried out in a quantitative manner, which to the authors' best knowledge has not been conducted before. The database contains an excess of 1 000 000 accumulated test hours from more than 150 tests, and has been published as open-access [2]. The intention was to obtain insights into the most deciding operation- and design-parameters of a SOC device. This would bring vital information for assessing and mitigating degradation and increasing lifetime, and thus bring down costs of the product. It turned out to be quite challenging, mainly due to how the reporting of degradation and lifetime is approached in the SOC community. This issue will be discussed and a standardized protocol for reporting long-term tests will be suggested, so as to raise awareness of how best to assess degradation and lifetime, and compare results between different tests and systems.

2.3 Degradation mechanisms

Because of the inherent complexity and interrelation between various parts of a cell and even more so, a stack, there exist a multitude of degradation mechanisms that can decrease the value-output of the system. The purpose of this study is not to describe every possible mechanism – as has already been done well by other authors (SOC [3], SOFC [4–8], SOEC [9–12]) – but a brief introduction to some of the most well-known degradation mechanisms follows and these mechanisms are illustrated in Fig. 2.1.

2.3.1 Interconnects and oxidant side

For the ferritic stainless steel based IC, the most well-known mechanisms are chromia scale growth and simultaneous volatilization of the protective chromia scale that forms on its surface during operation. The chromia scale itself has low electronic conductivity where interdiffusion of cation species like Cr, Co, Fe, Mn and Sr at the IC and oxygen electrode (or contact layer) interface will create layers with increased ohmic resistance [13]. For further information the review paper by Shaigan et al. is recommended [14].

The oxygen electrode and surrounding layers often suffers from Cr poisoning [15–19] from the IC and other upstream hot steel components. In fact, this is one of the most often mentioned degradation mechanisms in recent long-term stack tests [20–23] and an effective blocking coating layer is highly desired. Other impurities forming insulating phases are S, P, Cl, Na and Si [24, 25]. Phase instabilities and kinetic demixing due to evaporation or enhanced mobility of certain elements is also possible [15].

For cobaltite/ferrite oxygen electrodes, without a barrier layer or with a poor, porous barrier layer, La [26] and Sr [27, 28] may cause reactions between the oxygen electrode and the electrolyte. However, the commonly employed barrier layer of CGO and popular oxygen electrode LSCF may also suffer from La, Sr and Gd interdiffusion [29, 30]. Under high electrolysis current density, formation of micro-bubbles have been reported at the electrolyte interface, but this phenomenon has largely been mitigated by switching from the La-Sr-Mn-oxide (LSM) oxygen electrode to LSCF [31].

2.3.2 Electrolyte and fuel side

Aside from the aforementioned La- and Sr-reactions, the main problems for the electrolyte are related to mechanical or processing issues causing cracks and pin-

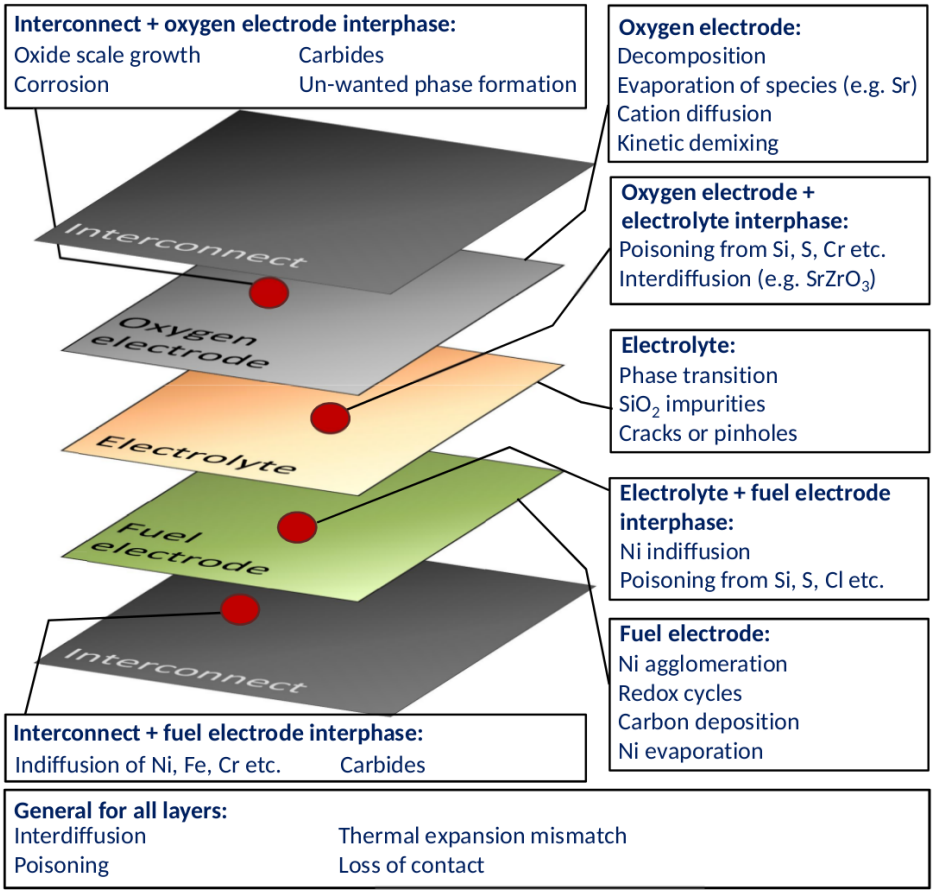

Figure 2.1: A simplified exploded view of a single-repeating unit (SRU) and a few of the possible degradation mechanisms. A SRU may involve additional layers such as multi-layered electrodes, barrier layers, coatings, sealing layers and/or contacting layers, which are not included in this example.

holes, which can lead to other issues such as re-oxidation of reduced Ni. However, the electrolyte can also be affected by impurities, e.g. SiO_2 collecting in the grain boundaries or incorporation of Mn from the oxygen electrode [32].

In many recent single-cell-tests with LSCF oxygen electrodes the component responsible for the highest degradation rate is the fuel electrode. The commonly used composite, Ni-YSZ, can cause catastrophic failure by re-oxidation [33–35] or carbon deposition [36–38], or degrade more gradually by Ni agglomeration [39–

41], leading to loss of electrical percolation and 3PB length, and by poisoning from impurities [42–44], i.e. S [45–47], Si [48], P [49, 50] and Cl [51–53].

On the fuel side of the IC, Ni interdiffusion and austenite formation [54], carbide formation [55], sigma-phase formation and oxide scale growth [56, 57] can all lead to an increased degradation rate.

In general for all interfaces there may be issues with interdiffusion layers, poor adhesion and loss of contact, especially between the electrodes and the IC. Impurities brought in from the original material, the gasses supplied or during manufacturing processes, are likewise important to consider.

2.4 Quantitative analysis

The general lack of published data became apparent while collecting data for the following analysis. The intent was to collect data specified in Tab. 2.1 for each test.

Table 2.1: Test information that was logged. **Bold** indicates that the information is often, but not always, available.

General	**Cell and/or stack producer, testing organization, year of publication**
Cell/stack	**Design type**, components (incl. IC's), **materials**, layer-thickness, -porosity and -tortuosity, particle sizes
Operation	**Testing temperature, length of test, number of cells, size of cells, current density, initial and final voltage**, initial ASR, **gas types**, gas flow rates, gas purities, gas utilization (e.g. fuel utilization, FU), number of thermal- and load-cycles
Degradation	Long-term degradation in mV/kh, **V%/kh**, mΩ cm^2/kh and mΩ cm^2 %/kh

Unfortunately this is far from possible in every reported test. Often, only the information in **bold** in Tab. 2.1 was available, but sometimes essential information such as number of cells or operating temperature is missing. In Fig. 2.2 the number of articles explicitly and implicitly (calculated from other parameters) stating specific parameters is shown for single-cell- and stack-tests. As seen, there is a noticeable lack of attention given to the ASR and in most cases the initial

ASR, the degradation rate in terms of mΩ cm^2/kh, and open-circuit voltage are in almost every reporting only accessible by estimation using Ohm's law, the Nernst equation and e.g. the Cantera software [58] (and thereby not accounting for any leaks). Certain information is understandably confidential by nature, but the widespread use of V%/kh as an indicator of degradation has already been questioned [59], and will be discussed further in sec. 2.6. Likewise, the lack of data reported will be addressed.

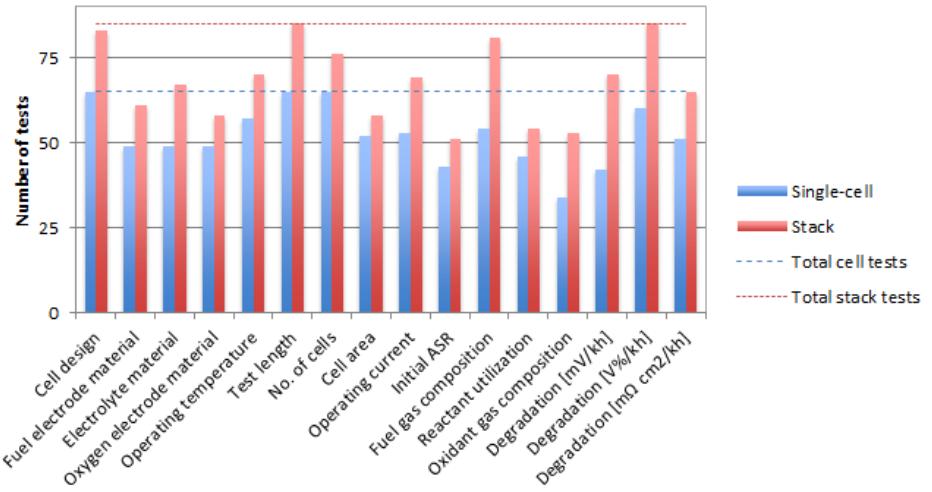

Figure 2.2: Data obtained from articles on single-cell or stack tests, either mentioned explicitly or calculable from other data mentioned.

2.5 Results

The number of accumulated test hours in this study is approximately 1 000 000 h, collected from 150 single-cell- and stack-tests. Please see the uploaded open-access database [2] for references and more details (download it for proper formatting). The data was mainly based on published articles, but conference proceedings and data from workshop presentations are included as well. Unpublished data from DTU, Topsoe Fuel Cell A/S and Haldor Topsøe A/S are included in the plots of this paper, but not in the open-access database. Only tests above 1 kh are included, and there has only been one prioritization, namely recently published articles. It should be kept in mind that most of the data originates from 2011-2015. It must also be noted that in the calculation of many of these values, a linear

degradation is assumed between initial and final voltage measurement. This is of course a simplification, but a necessary one considering the amount of data.

In the following section a number of plots based on the collected information are given. There are many arguments against blindly comparing very different tests, which will also be discussed later in the chapter. For instance, a 120-cell stack with 550 cm^2 active area cells running with natural gas cannot be directly compared to a 2-cell stack with 80 cm^2 active area cells running with H_2. Even if the latter has a much lower degradation rate and longer lifetime, the former is obviously closer to successful commercialization (depending on the intended application). Despite this, some interesting observations can still be made. Lastly, it is noted that not all companies are represented in the data due to lack of recent publications, e.g. major ones such as Bloom Energy, Acumentrics, Aisin, GE, Redox Power Systems, etc. This will naturally decrease the accuracy of any predictions.

2.5.1 Degradation rate and lifetime

The degradation rate reported for stack tests are shown in Fig. 2.3 with the degradation indicators V%/kh and mΩ cm^2/kh against the estimated test start date.

In fuel cell mode, for both indicators, the degradation rate appears to be decreasing with time. Using a simple linear regression one can estimate the average degradation rate of the reported tests, excluding outliers of Fig. 2.3, to reach 0.25 V%/kh or 0.11 V%/kh by year 2017 and 2019, respectively. These numbers represent respectively the former NEDO target, 40 kh lifetime with end-of-life (EoL) of 90% of initial voltage [20, 60, 61], and the new NEDO target, 90 kh and 90% of initial voltage [62]. The US Department of Energy has a similar target of 60 kh lifetime and an EoL of 82% of initial voltage by 2020 [63], i.e. 0.3 V%/kh. The SECA program reported similar targets [64]. The only mentioned ASR target of 4 mΩ cm^2/kh [3] is here predicted to be reached by year 2024. However, for a commercial breakthrough the average degradation rate does not necessarily need to reach the targets, it will likely be enough that just one or a few companies do so. On the other hand, a low degradation is not all that matters. The stack needs to be operated successfully for e.g. 40 kh or even 90 kh with the appropriate fuel gas type, and probably also with a certain number of thermal- and load-cycles. It is also noted that it is unknown if there is a tendency in the community to only report improvements, thereby skewing the trends observed here.

For reasons discussed in this paper it is near impossible to impose a fair “score” on a given test due to the multitude of influencing parameters and considerations. The authors of this paper hesitate to even mention the “best” tests, but in the published database the three longest running stack tests and the three stack tests

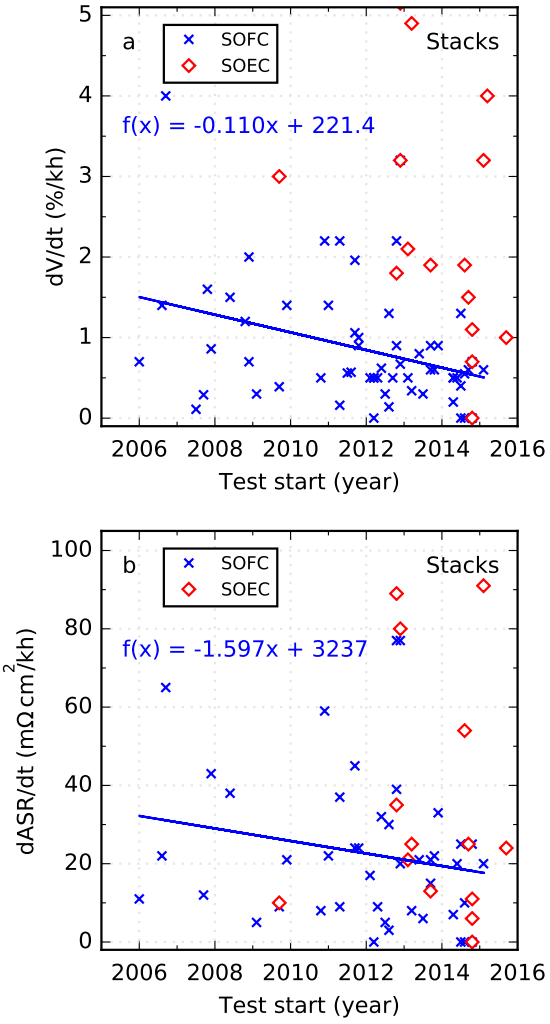

Figure 2.3: Degradation rate in a, V%/kh, and b, mΩ cm^2/kh against the date the stack test was started (estimated by publication year and test length). The legend indicates the operation mode.

with lowest degradation, for each category, are given. At the time of writing, for test length of SOFC stacks, Forschungszentrum Jülich (FZJ) [20] and HEXIS [65]

tops the chart with 65.2 kh (published) and 37 kh, respectively (see Fig. 2.5a). In terms of degradation, several have published apparent zero degradation (MHI [66], SOLIDpower [67], Elcogen [68]), albeit only with 7 kh, 4.2 kh and 2 kh test length, respectively. In electrolysis mode, fewer tests have been reported. The degradation rate is generally higher than it is for fuel cell mode and is quite scattered. For SOEC stacks, EIfER have reported 10 kh and 8.2 kh for stacks produced by SOLIDpower [67] and Topsoe Fuel Cell [69], respectively. Degradation of SOEC stacks is topped by FZJ [70] with negative degradation rate (activation) and 11 mΩ cm^2/kh degradation in two ~2 kh tests. For single-cell tests, please see the database.

One can also estimate the predicted lifetime of each test if linear degradation and an EoL are estimated, in this case to 90% of initial voltage for SOFC mode and 1.5 V for SOEC mode. These somewhat arbitrary values can be changed in the uploaded database if desired. This approach is probably overly optimistic, as it does not account for emergency shutdowns or accelerated degradation later in the stack's life etc. Also, tests with a reported degradation rate of 0 mV/kh or even activation has here been approximated to an estimated lifetime of 90 kh, which may be unrealistic. In any case, as seen in Fig. 2.4, the average estimated lifetime is increasing in recent years and for SOFC mode, again assuming a linear improvement and excluding tests with excessive degradation (>5 V%/kh), the average estimated lifetime will reach 40 kh by year 2018 and 60 kh by 2026. However, it becomes clear that to reach 90 kh in the foreseeable future, we would need to improve the lifetime faster than linearly. Again, the same arguments apply concerning a technology breakthrough based on the community average vs. just a single company reaching these targets.

2.5.2 Cell design

The planar fuel electrode supported cell design type is heavily favored among both cell- and stack-producers worldwide, which is reflected in Fig. 2.5. However, it does not seem that one design is more suited for long-term testing than another, but rather that all types of design work. It is also seen that although the average estimated lifetime has reached 30 kh (Fig. 2.4), the actual test length is rarely above 10 kh for both stack- and single-cell-tests. Long-term tests are expensive, especially for stacks, and time-consuming in nature, which is why degradation rate indicators and the estimated lifetime discussed before are interesting alternative measures to actually testing until the stack or cell fails. It is noted that tests showing high degradation rates initially would tend to be terminated prematurely, so the apparent correlation between low degradation rate and long test length may be tainted.

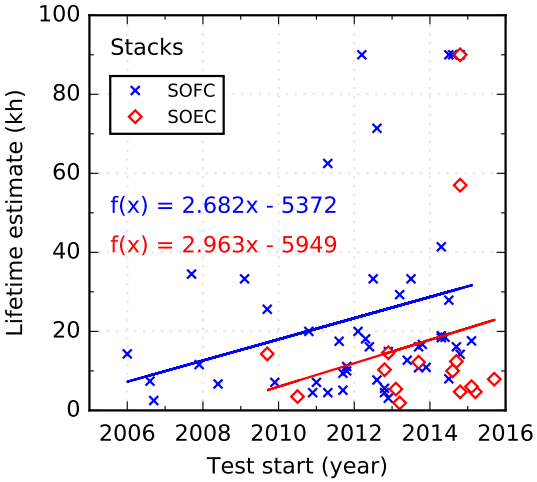

Figure 2.4: Estimated lifetime of each test against the estimated start date of the test. The legend indicates operation mode.

2.5.3 Electrode materials

As seen in Fig. 2.6, the more recently employed oxygen electrode material, LSCF, is commonly utilized in lower operation temperature tests, 700-750 °C, while LSM and other materials are commonly used at higher temperatures. This illustrates that, once again, lifetime and degradation rate is not all that matters.

Producers are well aware that a lower operating temperature is also desired, as this will allow for e.g. cheaper IC materials and a simpler balance-of-plant. As seen in Fig. 2.6, one reported test sticks out. Elcogen reported a stack test operating at 650 °C with La-Sr-Co oxygen electrodes with approximately zero degradation during the 2 kh the test ran for [68]. For further details, please see the mentioned database. In Fig. 2.7 the overwhelming popularity of Ni-containing fuel electrodes is clear. It is also seen that the degradation rate is generally lower for tests operated with pure reactant or natural gas, although the difference is minor.

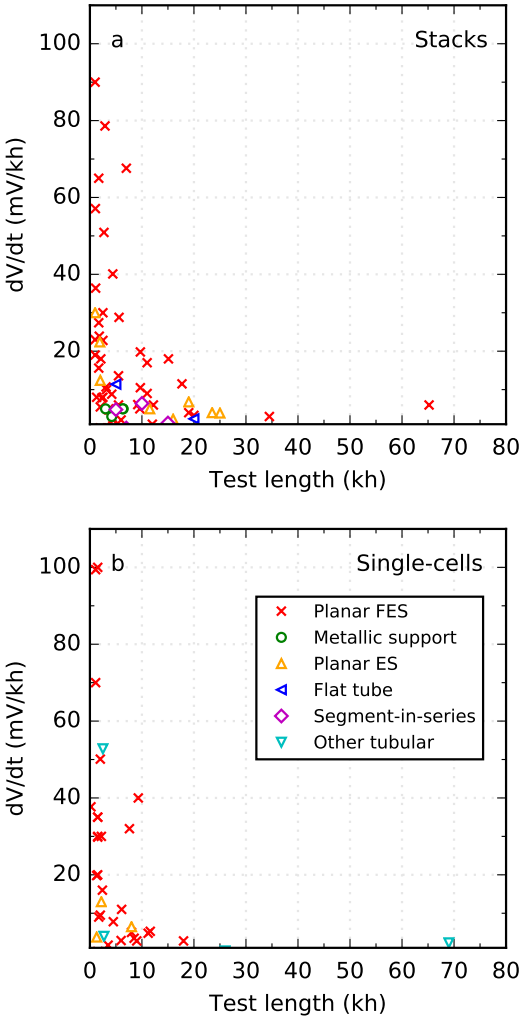

Figure 2.5: Degradation rate in mV/kh against length of the reported (a) stack- or (b) single-cell-test. The legend indicates the design of the cells, where FES stands for fuel electrode supported and ES for electrolyte supported.

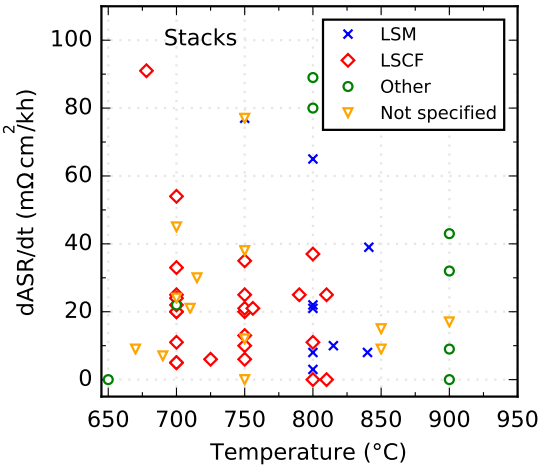

Figure 2.6: Degradation rate in mΩ cm^2/kh against temperature for the most common oxygen electrode materials.

2.5.4 Area-specific resistance

For some time now it has been speculated that many degradation mechanisms are overpotential driven [31, 46, 71, 72], e.g. a higher overpotential of the fuel electrode will lead to more degradation of the fuel electrode. Most reports about long-term tests do not include information as to the separation of resistance or degradation for each component, but in many cases the ASR under current right at the start of the test is calculable using Ohm's law. Plotting this initial ASR value against the overall degradation rate, Fig. 2.8a, seems to confirm that lower resistance will lead to a lower degradation rate. In Fig. 2.8b, it is observed that most SOFC tests are operated with an overvoltage of 100-300 mV, while SOEC tests are operated with much higher overvoltage. This may contribute to the generally higher degradation of cells and stacks operated in SOEC mode.

2.6 Discussion

The discussion of an ideal degradation indicator has been ongoing in the community for a number of years, see for instance Gemmen et al. [59]. The following should be seen as a continuation of that discussion.

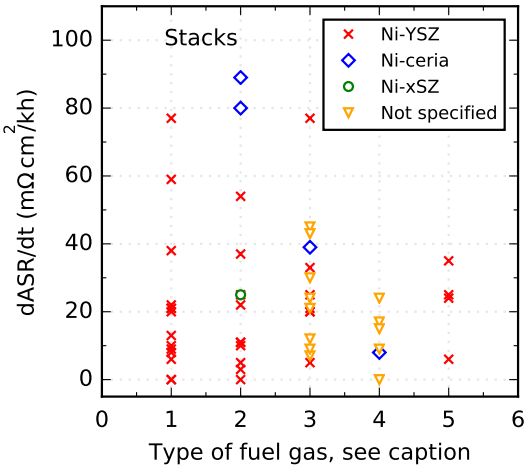

Figure 2.7: Degradation rate in mΩ cm^2/kh against different types of fuel gas for the most common fuel electrode materials. Type 1: 90-100% H_2 balanced by H_2O for SOFC or 90-100% H_2O balanced by H_2 for SOEC; type 2: 0-90% H_2 balanced by H_2O for SOFC or 0-90% H_2O balanced by H_2 for SOEC; type 3: H_2/H_2O with various hydrocarbons; type 4: Natural gas, CH_4 or propane; type 5: CO/CO_2.

2.6.1 The degradation indicator

The by far most commonly used parameter in the community to describe degradation is the loss of voltage in percent relative to the starting voltage per 1000 h (V%/kh). It is so widely accepted as a degradation indicator that some authors even neglect to specify voltage, but instead simply note "%/kh". This is an easily obtainable and quickly calculable parameter that is useful as it holds information on the conversion of energy. However, the parameter also has flaws. As it only takes the voltage and length of the test into account, one cannot compare cells with different initial performance or different operating conditions. If the test is operated mildly with poor performance, i.e. a low production of electricity or gas, V%/kh would be low, but the purpose of the system has not been optimized (depending on the intended application). Furthermore, if for instance the voltage decreases (or increases for SOEC) rapidly in the first couple of hundred hours and then regains performance in the last couple of hundred hours, then simply stating the V%/kh from the initial voltage measurement to the last, would be misleading.

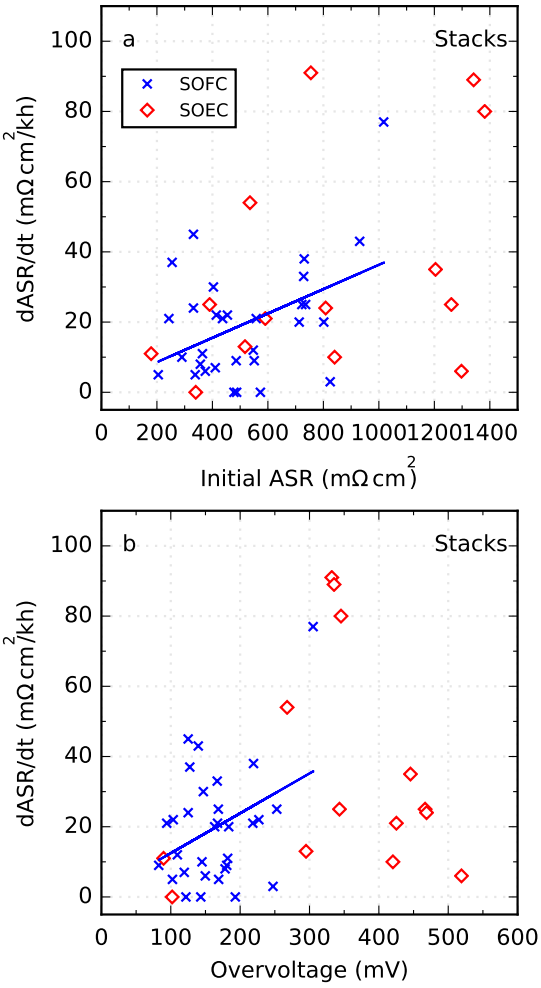

Figure 2.8: Degradation rate in mΩ cm^2/kh against (a) the initial ASR in mΩ cm^2, and (b) the overvoltage in mV. The legend indicates the operation mode.

Moreover, the reporting of the value is also quite subjective. Some authors choose to use the last e.g. 500 h of the test, while others disregard the first e.g. 300 h. The history of the cell or stack before initiating the constant-conditions-test will also have an effect, but this fact is rarely mentioned. As noted earlier, due to

the large dataset, in this study the entire (constant-conditions) test is generally included in the calculation of the number, but any nonlinearity of performance over time is not considered.

Unfortunately many projects and published articles also refer to targets using this unit. For instance, one of the SOFC degradation targets most commonly referred to in the past 5 years was 0.25 V%/kh, i.e. 10% loss in voltage over 40 000 h [20, 60, 61].

2.6.2 Alternative degradation indicators

A better parameter would be the increase in ASR per time-unit (dASR/dt), i.e. mΩ cm^2/kh. With this value, the change in performance, the lifetime and the current are taken into account, but the initial performance is not. This would allow for better comparison of degradation rates at different operating conditions. Using current density-potential (i-V) plots, the ASR can be determined from the secant or the tangent (using EIS) at the desired operating current density. The two methods often yield different values due to non-linearity in i-V curves, but it can also be determined quickly through Ohm's law, which will yield the same value as the secant-method. dASR/dt is rarely mentioned, but has in this study in many cases been calculated using Ohm's law and an estimated value for the OCV. As pointed out by others [59], one should carefully consider whether the experimental voltage or the ideal Nernst potential is used, as the former will include certain experimental effects (e.g. leaks) while the latter will not. Knibbe et al. mentioned this parameter as a target, i.e. 4 mΩ cm^2/kh [3].

Alternatively, one could use the loss in ASR normalized to the starting ASR per 1000 h (ASR%/kh). However, if the initial ASR is high, ASR%/kh would be small. So, this number does also not yield a fair comparison for different systems. The instantaneous ASR rate is attractive to use to visualize whether the degradation is accelerating or decelerating, but it does not constitute a viable alternative as a descriptive single-value indicator of degradation for an entire test. The average ASR throughout the test is technically not an indicator of degradation, but rather of performance (e.g. energy efficiency) throughout the entire test. To describe a whole test, it would be necessary to mention the deviation from the average as well. It is also quite sensitive to the test length, so standardizing this parameter would be needed.

Considering the energy aspect would reveal even more information than just using voltage or ASR. Different producers on the market have different customer segments, so in a fair comparison one would include the intended power output for the system in terms of electricity or fuel product and intended lifetime, e.g. a

specific μ-CHP technical target could be 5 kW operational for 5 years (788.4 GJ or 219 MWh) with 10 thermal cycles, 10 load cycles and an average energy efficiency of 50%. The energy efficiency is more difficult to calculate or estimate, but the information within this parameter is more directly relevant for the customer, i.e. how much energy is wasted? If the target is simply an amount of energy produced, e.g. 788.4 GJ in the example above, one could calculate the number of "re-buys" (replacing the stack) to reach the target, i.e. total power produced divided by the target, but it would be necessary to include the capital cost of the system as well.

While the simple reporting of V%/kh is a useful value to compare identical systems, using slightly more inputs in the degradation indicator (e.g. ASR/kh) would paint a clearer picture when comparing different systems. However, as discussed, it is difficult, if not impossible to identify one single parameter that includes all the necessary information for every situation. The ideal parameter for the customer would be the amount of energy produced (gas or electricity) per monetary unit spent (e.g. J/€). In the case of SOEC, a unit of L/€ might be more practical. Such a value is what the market or the customer is interested in, but it does require inputs such as system price, gas/electricity input price and measurements or estimations of the output product. Due to the lack of a developed market with listed system prices from producers this value could not be obtained in the present study. In certain cases it is possible to estimate the electrical energy produced or consumed (SOFC or SOEC, respectively) and the amount of gas consumed or produced (SOFC or SOEC). For SOEC operation below the thermoneutral voltage, the amount of heat supplied to the system should ideally be included as well. All in all, this can yield an expression of efficiency measured as kWh/m^3, which can be interesting to compare for different systems. The notion can be further investigated by estimating the total lifetime of the test if the EoL is assumed for instance to be 90% of initial voltage for a SOFC-unit. This can give an estimated lifetime had the test continued running. The total amount of electricity produced (SOFC mode) at the predicted EoL relative to the total amount of gas consumed can then be calculated. Estimations for electricity prices and gas prices can be used to calculate an estimated profit at the EoL for the test. Unfortunately such calculations are only possible if many of the parameters listed in Tab. 2.1 are available and as already discussed, it is rarely so. Nonetheless, in a few cases this was possible and is available for viewing in the open-access database. For H_2, kWh/m^3 is typically 1-2 for SOFC and 2-3 for SOEC.

2.6.3 Standardized reporting of long-term tests

As mentioned, the subject of a fair degradation indicator has been discussed before by others [6, 59, 73], many of whom have also pointed out the inherent drawbacks of using V%/kh. However, the degradation rate normalized by the initial voltage is still the preferred value in the community. To overcome the issues of comparing different tests, the testing itself would have to be standardized. This has been attempted in the FCTESTNET [74] and the FCTESqa [75] programs, where a set of particular conditions were specified for SOFC operation with a few chosen fuel gas types. The subject is also currently being investigated by the on-going SOCTESqa program [76], which also considers SOEC and reversible operation. Many companies and research institutes naturally operate with various internal quality assurance (QA) standards, like described by Haanappel et al. from FZJ [77, 78]. Such internationally recognized QA standards, like the ISO9000 series, are important first steps in the comparison between different systems. Still, one standard has not yet been adopted by the community. Unfortunately, with the high degree of variety from system to system, it seems near impossible at the present moment to standardize testing in a manner that would be fair to all systems. In the meantime, one alternative would be to standardize the reporting of tests, so that it is clearly visible when comparisons can be made. Furthermore, this would quickly convey information on the test in general as well. In Tab. 2.2 a suggestion for a simple standardization (assuming galvanostatic operation) is shown and the table has been uploaded for easy copy and paste [79].

Table 2.2: Suggested standardized reporting protocol for long-term tests.

Cell producer:		Cell design:	
Stack producer:		Fuel electrode:	
Testing organization:		Electrolyte:	
Date of test start:		Oxygen electrode:	
Operation mode:		Interconnect:	
Length of test:	kh	Average power:	kW
Temperature:	°C	OCV and initial voltage:	V
Current density:	A/cm^2	Initial ASR:	mΩ cm^2
Fuel gas composition:		Total degradation:	$V_{\%}$/kh mΩ cm^2/kh
Fuel gas flow:	L/h/cm^2		
Fuel gas utilization:	%	Average efficiency (+ std. deviation)	%
Oxidant gas:		Total production:	kWh L (of e.g. H_2)
Oxidant gas flow:	L/h/cm^2		
Oxidant gas utilization:	%	Degradation mechanisms:	
No. of thermal cycles:		Notes:	
No. of load cycles:			

2.6.4 Keeping the database up-to-date

The plots shown in this paper are merely examples of a few interesting comparisons and we invite the reader to compare and plot other parameters perhaps more relevant. The open-access degradation and lifetime database has been uploaded [2]. Anyone interested in using the data are welcome, but we ask that you cite this paper or the above-mentioned DOI in doing so. We also encourage companies and research institutes to contact the authors at enrgk-soctests@dtu.dk and supply data from your single-cell- or stack-test with either the proposed standardized reporting format or in similar format as the data in the database. This will keep the database up-to-date for the benefit of the solid oxide cell community.

2.7 Conclusions

A quantitative review of the current international status of lifetime and degradation for SOC devices has been presented. The study was based on a large dataset collected from more than 150 publications, and with the help of the community the database will continue to grow as more data is published. While the majority of cell- and stack-tests are limited to 10 kh, it was found that degradation rates in recent years have been steadily decreasing and an estimation of the predicted lifetime of the average stack is expected based on a linear trendline to reach the target of 40 kh before 2020, and 60 kh by 2026. However, targets will most likely be met even sooner for individual cases, which will facilitate market penetration. Several other observations based on the data are discussed.

Moreover, it was discussed how to report tests most efficiently so as to enable easy comparison between different systems. Due to the large array of differing parameters between systems and tests, a standardized reporting protocol in the form of a simple table is suggested. The SOC community is encouraged to adopt this standardized form of reporting tests.

2.8 References

1. Singhal, S. C. & Kendall, K. *High Temperature Solid Oxide Fuel Cells: Fundamentals, Design and Applications* (Elsevier, 2003).
2. Skafte, T. L., Hjelm, J., Blennow, P. & Graves, C. *SOC tests database v1.0 (open-access DOI: 10.6084/m9.figshare.1607410)* 2016.
3. Knibbe, R., Hauch, A., Hjelm, J., Ebbesen, S. D. & Mogensen, M. Durability of Solid Oxide Cells. *Green* **1,** 141–169 (Jan. 2011).
4. Yokokawa, H., Horita, T., Yamaji, K., Kishimoto, H. & Brito, M. Degradation of SOFC Cell/Stack Performance in Relation to Materials Deterioration. *Journal of the Korean Ceramic Society* **49,** 11–18 (Jan. 2012).
5. Yokokawa, H., Tu, H., Iwanschitz, B. & Mai, A. Fundamental mechanisms limiting solid oxide fuel cell durability. *Journal of Power Sources* **182,** 400–412 (Aug. 2008).
6. Steinberger-Wilckens, R. *et al.* Real-SOFC - A Joint European Effort in Understanding SOFC Degradation. *ECS Transactions* **7,** 67–76 (2007).
7. Tu, H. & Stimming, U. Advances, aging mechanisms and lifetime in solid-oxide fuel cells. *Journal of Power Sources* **127,** 284–293 (Mar. 2004).
8. Mogensen, M., Jensen, K., Jørgensen, M. & Primdahl, S. Progress in understanding SOFC electrodes. *Solid State Ionics* **150,** 123–129 (2002).
9. Ebbesen, S. D., Jensen, S. H., Hauch, A. & Mogensen, M. B. High Temperature Electrolysis in Alkaline Cells, Solid Proton Conducting Cells, and Solid Oxide Cells. *Chemical Reviews* **114,** 10697–10734 (Nov. 2014).
10. Moçoteguy, P. & Brisse, A. A review and comprehensive analysis of degradation mechanisms of solid oxide electrolysis cells. *International Journal of Hydrogen Energy* **38,** 15887–15902 (Dec. 2013).
11. Laguna-Bercero, M. Recent advances in high temperature electrolysis using solid oxide fuel cells: A review. *Journal of Power Sources* **203,** 4–16 (Apr. 2012).
12. Hansen, J. B. Solid oxide electrolysis - a key enabling technology for sustainable energy scenarios. *Faraday Discuss.* **182,** 9–48 (2015).
13. Menzler, N., Batfalsky, P. & Groß, S. Post-Test Characterization of an SOFC Short-Stack after 17,000 Hours of Steady Operation. *ECS Transactions* **35,** 195–206 (2011).
14. Shaigan, N., Qu, W., Ivey, D. G. & Chen, W. A review of recent progress in coatings, surface modifications and alloy developments for solid oxide fuel cell ferritic stainless steel interconnects. *Journal of Power Sources* **195,** 1529–1542 (Mar. 2010).

15. Jiang, S. P. & Chen, X. Chromium deposition and poisoning of cathodes of solid oxide fuel cells - A review. *International Journal of Hydrogen Energy* **39,** 505–531 (Jan. 2014).

16. Hilpert, K., Das, D. & Miller, M. Chromium vapor species over solid oxide fuel cell interconnect materials and their potential for degradation processes. *Journal of The Electrochemical Society* **143,** 3642–3647 (1996).

17. Matsuzaki, Y. & Yasuda, I. Dependence of SOFC Cathode Degradation by Chromium-Containing Alloy on Compositions of Electrodes and Electrolytes. *Journal of The Electrochemical Society* **148,** A126 (2001).

18. Paulson, S. C. & Birss, V. I. Chromium Poisoning of LSM-YSZ SOFC Cathodes. *Journal of The Electrochemical Society* **151,** A1961 (2004).

19. Yokokawa, H. *et al.* Thermodynamic considerations on Cr poisoning in SOFC cathodes. *Solid State Ionics* **177,** 3193–3198 (Nov. 2006).

20. Blum, L., Packbier, U., Vinke, I. C. & de Haart, L. G. J. Long-Term Testing of SOFC Stacks at Forschungszentrum Jülich. *Fuel Cells* **13,** 646–653 (Aug. 2013).

21. Mai, A., Schuler, J. A., Fleischhauer, F., Nerlich, V. & Schuler, A. Hexis and the SOFC System Galileo 1000 N: Experiences from Lab and Field Testing. *ECS Transactions* **68,** 109–116 (July 2015).

22. Yamamoto, T. *et al. Development of SOFC Performance and Durability Evaluations Technology* in *ECS Transactions* **25** (ECS, 2009), 499–508.

23. Yamamoto, T., Yasumoto, K. & Yoshikawa, M. Performance Evaluations for Long Term Durability and Reliability of Segment-In-Series Tubular Type SOFCs. *ECS Transactions* **57,** 763–770 (2013).

24. Yokokawa, H., Horita, T., Yamaji, K., Kishimoto, H. & Brito, M. M. Materials Chemical Point of View for Durability Issues in Solid Oxide Fuel Cells. *Journal of the Korean Ceramic Society* **47,** 26–38 (Jan. 2010).

25. Horita, T. *et al.* Effects of impurities on the degradation and long-term stability for solid oxide fuel cells. *Journal of Power Sources* **193,** 194–198 (Aug. 2009).

26. Mitterdorfer, A. $La_2Zr_2O_7$ formation and oxygen reduction kinetics of the $La_{0.85}Sr_{0.15}Mn_yO_3$, O_2(g)|YSZ system. *Solid State Ionics* **111,** 185–218 (Sept. 1998).

27. Simner, S. P., Anderson, M. D., Engelhard, M. H. & Stevenson, J. W. Degradation Mechanisms of La-Sr-Co-Fe-O_3 SOFC Cathodes. *Electrochemical and Solid-State Letters* **9,** A478 (2006).

28. Knibbe, R. *et al.* Cathode-Electrolyte Interfaces with CGO Barrier Layers in SOFC. *Journal of the American Ceramic Society* **93,** 2877–2883 (Apr. 2010).

29. Uhlenbruck, S., Moskalewicz, T., Jordan, N., Penkalla, H.-J. & Buchkremer, H. Element interdiffusion at electrolyte - cathode interfaces in ceramic high-temperature fuel cells. *Solid State Ionics* **180,** 418–423 (Apr. 2009).

30. Izuki, M. *et al.* Interfacial stability and cation diffusion across the LSCF/GDC interface. *Journal of Power Sources* **196,** 7232–7236 (2011).

31. Graves, C., Ebbesen, S. D., Jensen, S. H., Simonsen, S. B. & Mogensen, M. B. Eliminating degradation in solid oxide electrochemical cells by reversible operation. *Nature Materials* **14,** 239–244 (Dec. 2015).

32. Malzbender, J., Batfalsky, P., Vaßen, R., Shemet, V. & Tietz, F. Component interactions after long-term operation of an SOFC stack with LSM cathode. *Journal of Power Sources* **201,** 196–203 (Mar. 2012).

33. Pihlatie, M., Kaiser, A. & Mogensen, M. Redox stability of SOFC: Thermal analysis of Ni-YSZ composites. *Solid State Ionics* **180,** 1100–1112 (July 2009).

34. Klemensø, T., Chung, C., Larsen, P. H. & Mogensen, M. The Mechanism Behind Redox Instability of Anodes in High Temperature SOFCs. *Journal of The Electrochemical Society* **152,** A2186 (2005).

35. Jeangros, Q. *et al.* Oxidation mechanism of nickel particles studied in an environmental transmission electron microscope. *Acta Materialia* **67,** 362–372 (Apr. 2014).

36. Tao, Y., Ebbesen, S. D. & Mogensen, M. B. Carbon Deposition in Solid Oxide Cells during Co-Electrolysis of H_2O and CO_2. *Journal of the Electrochemical Society* **161,** F337–F343 (Jan. 2014).

37. Skafte, T. L., Graves, C., Blennow, P. & Hjelm, J. Carbon Deposition during CO_2 Electrolysis in Ni-Based Solid-Oxide-Cell Electrodes. *ECS Transactions* **68,** 3429–3437 (2015).

38. Maher, R. C. *et al.* Raman Spectroscopy of Solid Oxide Fuel Cells: Technique Overview and Application to Carbon Deposition Analysis. *Fuel Cells* **13,** 455–469 (Aug. 2013).

39. Pihlatie, M., Kaiser, A., Mogensen, M. & Chen, M. Electrical conductivity of Ni-YSZ composites: Degradation due to Ni particle growth. *Solid State Ionics* **189,** 82–90 (May 2011).

40. Simwonis, D., Tietz, F. & Stöver, D. Nickel coarsening in annealed Ni/8YSZ anode substrates for solid oxide fuel cells. *Solid State Ionics* **132,** 241–251 (2000).

41. Tanasini, P. *et al.* Experimental and Theoretical Investigation of Degradation Mechanisms by Particle Coarsening in SOFC Electrodes. *Fuel Cells* **9,** 740–752 (Oct. 2009).

42. Ebbesen, S. D., Graves, C., Hauch, A., Jensen, S. H. & Mogensen, M. Poisoning of Solid Oxide Electrolysis Cells by Impurities. *Journal of The Electrochemical Society* **157,** B1419 (2010).

43. Ebbesen, S. D. & Mogensen, M. Exceptional Durability of Solid Oxide Cells. *Electrochemical and Solid-State Letters* **13,** B106 (2010).

44. Sasaki, K., Haga, K. & Yoshizumi, T. Impurity poisoning of SOFCs. *ECS Transactions* **35,** 2805–2814 (2011).

45. Sasaki, K. *et al.* H_2S Poisoning of Solid Oxide Fuel Cells. *Journal of The Electrochemical Society* **153,** A2023 (2006).

46. Hauch, A., Hagen, A., Hjelm, J. & Ramos, T. Sulfur Poisoning of SOFC Anodes: Effect of Overpotential on Long-Term Degradation. *Journal of the Electrochemical Society* **161,** F734–F743 (May 2014).

47. Hagen, A., Rasmussen, J. F. & Thydén, K. Durability of solid oxide fuel cells using sulfur containing fuels. *Journal of Power Sources* **196,** 7271–7276 (Sept. 2011).

48. Hauch, A., Jensen, S. H., Bilde-Sørensen, J. B. & Mogensen, M. Silica Segregation in the Ni/YSZ Electrode. *Journal of The Electrochemical Society* **154,** A619 (2007).

49. Xu, C. *et al.* The effect of phosphine in syngas on Ni-YSZ anode-supported solid oxide fuel cells. *Journal of Power Sources* **193,** 739–746 (Sept. 2009).

50. Zhi, M., Chen, X., Finklea, H., Celik, I. & Wu, N. Q. Electrochemical and microstructural analysis of nickel-yttria-stabilized zirconia electrode operated in phosphorus-containing syngas. *Journal of Power Sources* **183,** 485–490 (Sept. 2008).

51. Haga, K., Shiratori, Y., Ito, K. & Sasaki, K. Chlorine Poisoning of SOFC Ni-Cermet Anodes. *Journal of The Electrochemical Society* **155,** B1233 (2008).

52. Marina, O., Pederson, L., Thomsen, E., Coyle, C. & Yoon, K. Reversible poisoning of nickel/zirconia solid oxide fuel cell anodes by hydrogen chloride in coal gas. *Journal of Power Sources* **195,** 7033–7037 (Oct. 2010).

53. Xu, C., Gong, M., Zondlo, J. W., Liu, X. & Finklea, H. O. The effect of HCl in syngas on Ni-YSZ anode-supported solid oxide fuel cells. *Journal of Power Sources* **195,** 2149–2158 (Apr. 2010).

54. Sarda, V., Auvinen, S. & Shemet, V. Long Term Resistivity Behavior of SOFC Interconnect/Ni-Mesh/Anode Interfaces. *ECS Transactions* **57,** 2279–2288 (2013).

55. Ziomek-Moroz, M., Covino, B., Holcomb, G., Bullard, S. & Penner, L. *Studies of Scale Formation and Kinetics of Crofer22APU and Haynes 230 in Carbon Oxide-containing Environment for SOFC Applications*

56. Hammer, J. E. *et al.* The Oxidation of Ferritic Stainless Steels in Simulated Solid-Oxide Fuel-Cell Atmospheres. *Oxidation of Metals* **67,** 1–38 (Jan. 2007).

57. Sachitanand, R., Sattari, M., Svensson, J.-E. & Froitzheim, J. Coatings for SOFC Interconnects in Fuel Side Environments. *ECS Transactions* **68,** 1575–1580 (July 2015).

58. Goodwin, D. G. *Cantera*

59. Gemmen, R. S., Williams, M. C. & Gerdes, K. Degradation measurement and analysis for cells and stacks. *Journal of Power Sources* **184,** 251–259 (2008).

60. Mugikura, Y., Yasumoto, K. & Morita, H. Performance Evaluation Technology for Long Term Durability and Reliability of SOFCs. *ECS Transactions* **57,** 649–656 (2013).

61. Horita, T., Kishimoto, H. & Yamaji, K. Degradation and Durability of SOFC Materials by the Impurities. *ECS Transactions* **30,** 115–122 (2011).

62. Tomoshige, Y., Mori, N., Iha, M., Takada, T. & Konoike, T. Development of a New Concept SOFC at Murata. *ECS Transactions* **57,** 115–122 (2013).

63. Spendelow, J., Marcinkoski, J. & Papageorgopoulos, D. *Micro CHP Fuel Cell System Targets* tech. rep. (2011).

64. Guthrie, G. & Gerdes, K. *Advanced Fuel Cell Research at NETL.* 2012.

65. Mai, A. *et al.* Progress in the Development of the Hexis' SOFC Stack and the Galileo 1000 N Micro-CHP System. *ECFC Proceedings,* A0403 (2012).

66. Kobayashi, Y. *et al.* Recent Progress of SOFC Combined Cycle System with Segmented-In-Series Tubular Type Cell Stack at MHI. *ECS Transactions* **57,** 53–60 (Oct. 2013).

67. Bertoldi, M., Bucheli, O. & Ravagni, A. Development, Manufacturing and Deployment of SOFC-Based Products at SOLIDpower. *ECS Transactions* **68,** 117–123 (2015).

68. Noponen, M. *et al.* Status of Solid Oxide Fuel Cell Development at Elcogen. *ECS Transactions* **68,** 151–156 (2015).

69. Corre, G. & Brisse, A. 9000 Hours Operation of a 25 Solid Oxide Cells Stack in Steam Electrolysis Mode. *ECS Transactions* **68,** 3481–3490 (2015).

70. Fang, Q., Blum, L. & Menzler, N. H. Performance and Degradation of Solid Oxide Electrolysis Cells in Stack. *Journal of The Electrochemical Society* **162,** F907–F912 (2015).

71. Graves, C., Ebbesen, S. D. & Mogensen, M. Co-electrolysis of CO_2 and H_2O in solid oxide cells: Performance and durability. *Solid State Ionics* **192,** 398–403 (June 2011).

72. Chen, M. *et al.* Microstructural Degradation of Ni/YSZ Electrodes in Solid Oxide Electrolysis Cells under High Current. *Journal of the Electrochemical Society* **160,** F883–F891 (May 2013).

73. Williams, M., Gemmen, R. & Richards, G. Evaluation of Fuel Cell Performance and Degradation. *ECS Transactions* **35,** 621–636 (2011).

74. Friberg, R. *et al.* A proposal of a harmonized testing format for fuel cell technology - FCTESTNET. *Proceedings of the 3rd International Conference on Fuel Cell Science, Engineering, and Technology,* 753–761 (2005).

75. Joint Research Centre. *FCTESqa* 2010.

76. Fuel Cells and Hydrogen Joint Undertaking. *SOCTESqa* 2016.

77. Haanappel, V. a. C. & Smith, M. J. Quality Assurance and Solid Oxide Fuel Cell Testing at Forschungszentrum Juelich. *Journal of Fuel Cell Science and Technology* **4,** 194 (2007).

78. Haanappel, V. A. C. & Smith, M. J. A review of standardising SOFC measurement and quality assurance at FZJ. *Journal of Power Sources* **171,** 169–178 (2007).

79. Skafte, T. L., Hjelm, J., Blennow, P. & Graves, C. *Standardized reporting of SOC tests (DOI: 10.6084/m9.figshare.3198715)* 2016.

3 Carbon formation in the electrode

By focusing on a specific SOC system and use-case we can decrease the complexity and number of relevant degradation and failure mechanisms. Thus it will be possible to identify one or two key issues, which can then be addressed and hopefully mitigated. In this manner we can improve the technology sufficiently for it to meet the high expectations set by the market. Focusing on a niche market will further increase the probability of market penetration.

Haldor Topsoe A/S has developed a commercially available SOC system based on the well-known Ni-YSZ|YSZ|LSCF-CGO cell structure. The company has furthermore identified the conversion of CO_2 into CO as a potential niche market, as described in chapter 1. Here we investigate this type of cell and operation mode and have identified the main issues related to it, namely carbon formation and sulfur poisoning in the Ni-containing electrode. We will examine the effect of operating parameters on the mechanisms and also carry out preliminary attempts at mitigating the problem.

The following pages are based on the 2^{nd} publication: Carbon deposition and sulfur poisoning during CO_2 electrolysis in Ni-based solid-oxide-cell electrodes.

3.1 Abstract

The effect of operating parameters on carbon formation during CO_2-electrolysis is investigated systematically using simple current potential experiments. Due to variations of local conditions it is shown that higher current density and lower fuel electrode porosity will cause local carbon formation at the electrochemical reaction sites despite operating with a CO outlet concentration outside the carbon formation region. Attempts at mitigating the issue with nanoparticle infiltration and sulfur passivation proved unsuccessful. Increasing the fuel electrode porosity can alleviate the problem, but only to a certain extent. This work shows that the outlet CO concentration of a specific CO_2-electrolysis system is limited to up to 50% lower than expected based on the thermodynamic carbon deposition threshold at the inlet temperature, due to temperature and gas composition gradients. Furthermore, cells operated in CO_2-electrolysis mode are poisoned by

reactant gases containing ppb-levels of sulfur, in contrast to ppm-levels for SOFC operation.

3.2 Introduction

The generation and utilization of cheap, renewable electricity is becoming increasingly widespread. Most of the sustainable energy sources are directly linked to the weather and are thus intermittent in nature. As weather changes in the short term and the medium-to-long term due to seasons, production of sustainably sourced energy will vary. Such variation in the energy production and the resulting consequences can be mitigated by storing the energy for later use. A single solution strategy for energy storage is unlikely to succeed, but high-temperature electrolysis with SOC devices offers some distinct advantages. Such devices have high electrical efficiency [1, 2] and combined with conventional catalysis they are capable of converting electrical energy into synthetic hydrocarbon fuels [3–5].

With vast excess of electrical energy during some parts of the day and year in the not-too-distant future, the hydrogen economy seems the ideal solution [6]. However, the transition is likely to be excessively costly to implement. An attractive alternative which can take advantage of the already existent infrastructure is a society with a closed CO_2 loop [7]. Such a strategy has the added advantage of focusing on extracting already emitted CO_2 [8].

Production of synthetic hydrocarbon fuels with SOCs and the subsequent Fischer-Tropsch reaction cannot presently compete with cheap oil prices. However, there are niche-markets where the SOC technology can be cost-effectively employed and developed for the more idealized, long-term scenarios mentioned above. Reduction of CO_2 to CO and O_2 in SOCs is an interesting and seemingly simple process [9]. The products can potentially find use in the chemical industry, military operations where silent production of high purity O_2 is required, or in more extravagant applications such as utilization of the CO_2-rich atmosphere found on Mars [10]. In fact, an SOC is planned to be brought on the coming 2020-NASA rover-mission for preliminary investigations [11, 12]. The initial purpose may be rocket fuel production at location to minimize the required cargo that is brought from Earth. However, large scale fuel production using more traditional homogenous catalysis reactions such as the Sabatier process, eq. 3.1, may be more cost-efficient in the long-term, possibly in combination with the reverse water gas shift (RWGS) reaction [13], eq. 3.2.

$$CO_2 + 4H_2 \rightleftharpoons CH_4 + 2H_2O \qquad \text{(eq. 3.1)}$$

$$CO_2 + H_2 \rightleftharpoons CO + H_2O \qquad \text{(eq. 3.2)}$$

However, the same electrolysis cells would then just be used for conversion and recycling of the H_2O to H_2, which is needed for such processes. To increase the oxygen-to-methane ratio, it would also be possible to use the electrolysis cells for production of oxygen from CO_2 to supplement the RWGS reaction. Furthermore, before a sustainable micro-ecosystem is established, the oxygen produced by the devices can also be used to prepare a breathable atmosphere before human arrival.

CO_2 reduction in SOCs is less studied than H_2O electrolysis and operation in fuel cell mode. Much of the know-how established from decades of SOFC research can be applied directly, but there are also more specific issues, e.g. carbon formation in Ni containing electrodes. This has been extensively studied for steam reforming [14, 15], but in the SOC community the issue has mainly received attention during co-electrolysis of CO_2 and H_2O [16, 17], and during C_xH_y fuel cell operation [18–20]. Tao et al. suggested that gradients through the electrode causes carbon formation primarily due to gas diffusion limitations [16, 17]. Few studies specifically addressing carbon deposition during CO_2-electrolysis exists [21–24]. Some have reported a more severe effect during electrolysis mode compared to fuel cell mode, and Li et al. suspected the direct electrochemical decomposition of CO to C and O^{2-} [24]. The latter will be examined in detail in chapter 4, but in the present study we focus on the technical implications. We have previously reported a straight-forward *operando* detection method utilizing the voltage-response to a changing current density [25], but we will briefly summarize the arguments for its validity below.

3.3 Experimental

Single-cell measurements were performed on Ni-YSZ supported cells with 16 cm^2 active area produced by Haldor Topsoe A/S. The cells had the well-known Ni-YSZ|YSZ|CGO|LSCF-structure. All cells were tested at the Technical University of Denmark (DTU). Further details about the cells and testing setup can be found in Skafte et al. [25]. Two cells of the same general structure, but with different oxygen electrode materials and different fuel electrode porosity were also produced at DTU. The difference in porosity were obtained by sintering the fuel electrode and electrolyte at different temperatures. More information about these cells can be found in Ebbesen et al. [26]. Small variations in thickness of the different components and absolute performance of the different cells is not believed to

affect the observations reported here. By focusing on the Boudouard reaction, eq. 3.3, and solely carrying out coking experiments in a CO/CO_2-atmosphere, it is possible to exclude complications from the RWGS reaction, CH_4 decomposition or the Bosch reaction, eq. 3.4.

$$2CO \rightleftharpoons CO_2 + C \quad \text{(eq. 3.3)}$$

$$CO_2 + 2H_2 \rightleftharpoons 2H_2O + C \quad \text{(eq. 3.4)}$$

3.3.1 Method

This study will investigate the phenomenon of carbon deposition occurring before the thermodynamically expected threshold. As an illustration of this issue, a cell was operated in CO/CO_2 with a CO outlet gas concentration just below the Boudouard limit. As seen in Fig. 3.1a, the cell voltage increased dramatically within just 5 hours of operation, thereby indicating coking conditions in the cell despite being outside the thermodynamically favored region. To investigate this further, a method was developed which is described in more detail in Skafte et al. [25]. Electrolysis current was gradually increased in steps over the course of several hours until the voltage became unstable and started increasing (Fig. S.3.1). When this happened, the current was decreased to OCV again, and hysteresis in the iV-plot is observed (Fig. 3.1b). When stopping the current scan well before the Boudouard threshold, the voltage remains stable and no hysteresis is observed. The outlet gas concentration can be calculated using Faraday's law of electrolysis and the ideal gas law, as shown in the Supporting Information.

The operating conditions are only barely crossing into the carbon deposition regime and the cell thus only suffers minor damage (the cell shown in Fig. 3.1b is intentionally coked more than regularly for illustrative purposes). Therefore, the experiment can be repeated multiple times on the same cell and statistical confidence in the results are increased significantly.

Further evidence supporting the validity of the method can be found in the Supporting Information and in Skafte et al. [25], i.e. measurements of pO_2 (Fig. S.3.2), SEM (Fig. S.3.3), and EIS (Fig. S.3.4). This method is employed to study the effects of various operational parameters on a commercial cell. The technique was confirmed to reproduce the general trend on three different cell test rigs by different test personnel.

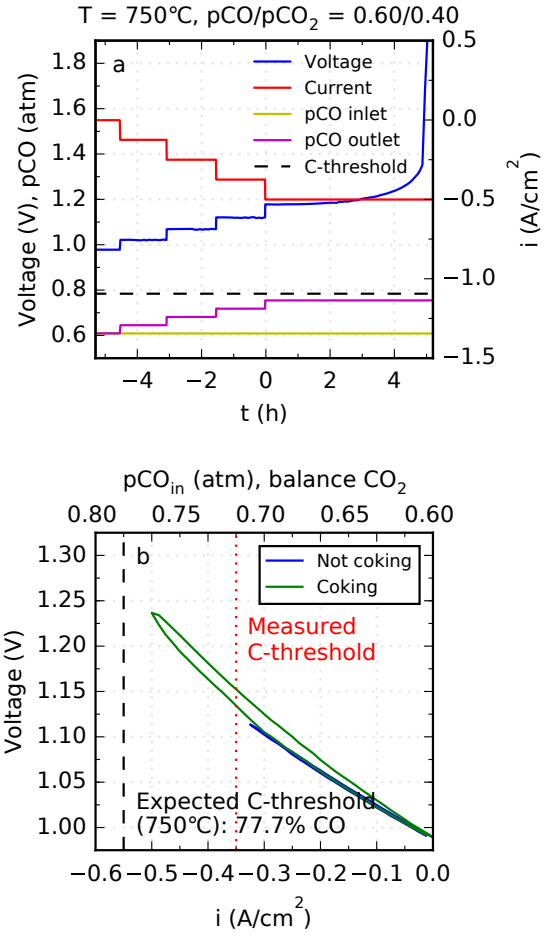

Figure 3.1: (a) Current density, cell voltage, theoretically calculated pCO gas concentration for the inlet and outlet, and the Boudouard threshold for a cell tested in a CO/CO_2-atmosphere. (b) Current-voltage curves in a CO/CO_2-atmosphere. The vertical black line indicates where one would expect the Boudouard threshold to be based on the outlet gas composition. The vertical red line indicates approximately the position of the measured Boudouard threshold.

3.4 Results and discussion

When varying the fuel inlet composition, the onset of coking occurs well before the expected Boudouard threshold as calculated from the fuel outlet gas composition (Fig. 3.2). Those calculations are based on average parameters (temperature, current density, gas concentration) for the entire cell, and not for the local conditions at the reaction sites. The observed deviation of the onset of coking from the expected threshold thus indicates that variations, or gradients, in conditions throughout the cell are the cause of this effect, as was also hypothesized by Tao et al. [16, 17]. They showed that with a sufficiently high porosity, the carbon deposition was not observed. Both the gas composition and temperature will vary across the cell as the reactants are converted along the flow direction. Furthermore, the gas composition and temperature will vary within the electrode. When approaching the reaction sites the product concentration will increase and the temperature will drop (endothermic reaction), which are exactly the conditions that will increase the likelihood of carbon deposition. The gas composition may be further affected by gas diffusion limitations in the electrode. Again, this will increase the concentration of the reducing agent, CO, at the electrode/electrolyte interface. The fact that carbon is more likely to deposit at the electrode/electrolyte interface under electrolysis current has previously been shown experimentally during co-electrolysis by Tao et al. [16, 17] and using in-operando Raman spectroscopy during CO_2 electrolysis by Duboviks et al. [23].

3.4.1 Effect of operating parameters

The effect of different operating parameters was studied systematically. The effect of fuel electrode porosity was also investigated. This parameter had a large impact on when carbon would form, as the decreased porosity is expected to lead to more severe concentration gradients in the electrode during operation. Current density also showed a high correlation with the onset of carbon formation. The results can be seen in Fig. 3.3, where each data point for the corresponding cell represents the onset of carbon formation as found using the described method. It is seen from Fig. 3.3a, that a cell with 30% porosity, operating at -1 A/cm^2 can be limited to converting only 55% of a 100% CO_2 inlet reactant gas, or 23%-units below the theoretical Boudouard threshold. From Fig. 3.3b, it is seen that the effect is even more severe for cells with low porosity electrodes. However, there may be a porosity threshold, above which the effect is negligible. Surprisingly, during these tests, both fuel utilization (Fig. S.3.6) and total fuel gas flow (Fig. S.3.7) had little to no impact on the deviation from the expected Boudouard threshold.

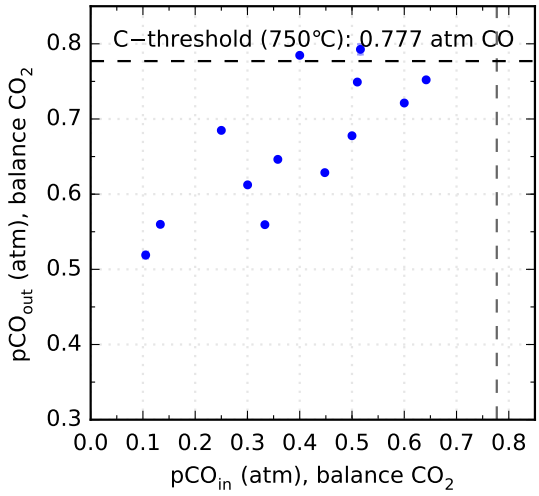

Figure 3.2: Performing the described iV-experiments with different fuel inlet compositions revealed carbon formation for fuel outlet compositions before the expected thermodynamic threshold.

3.4.2 Modeling verification

The results obtained in this study has been verified by two separate COMSOL finite-elements multiphysics models. Using a 2D model, Duhn et al. found a high effect of changing the porosity and/or the tortuosity [27]. Likewise, current density was also found to be of high influence on the onset of carbon deposition, in good agreement with this study. Likewise, Navasa et al. similarly found good agreement between these experimental results and the modeling results of a 3D cell model incorporating kinetic and thermal effects [28, 29]. She found that the carbon activity was highest at the electrode/electrolyte interface, due to a higher CO concentration and lower temperature on account of the endothermic reaction [29, 30].

The correlation between carbon deposition and current density is of vital importance for a commercial system. One would typically want to increase the current, so as to increase the efficiency and production rate of the system. Unfortunately, as shown in this study, one will have to balance these parameters with the risk of forming carbon. Increasing the operating temperature to decrease the risk of crossing the Boudouard threshold is often not an option if relatively inexpensive metallic interconnects are used in the system and long lifetimes are desired. To

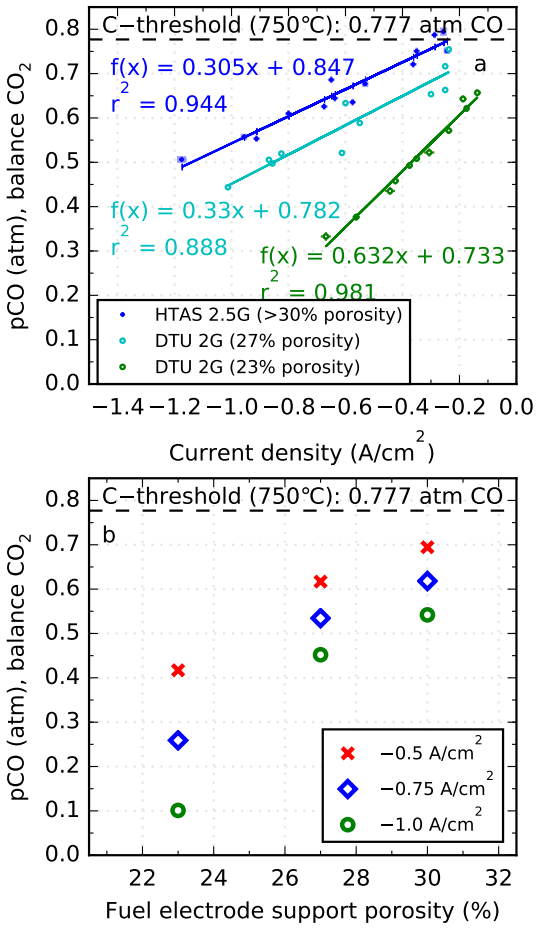

Figure 3.3: Three different cells with varying fuel electrode porosity were operated at 750 °C with air to the oxygen electrode. The outlet gas concentration where carbon deposition was found to take place as found by means of iV-experiments is plotted against (a) current density and (b) porosity of the fuel electrode.

optimize the operation of the system, one can use experiments such as these to obtain an expression for the CO gas concentration gradient through the electrode. Similarly, the experiments can be used to confirm full stack multiphysics modeling,

where the gradients are more pronounced than for a single cell. Thus, a full size 3D stack model developed at Haldor Topsoe A/S [31] was used to investigate gradients throughout a stack. Including the electrode microstructural effects in a full stack model would be very computational intensive, but the results of the two modeling approaches can be combined to optimize the operating strategy. All in all, as illustrated qualitatively in Fig. 3.4, one is left with restrictions on the possible operating window coming from gradients in the cell, gradients through the stack and temperature limitations of the IC material.

3.4.3 Mitigation

As will be shown in the following, it is extremely difficult to hinder carbon formation while employing the common Ni-YSZ electrode. A lot of work has been done on this issue in the catalysis community [32, 33], and there are many methods to test. One natural way of dealing with the problem would be to avoid the use of Ni, and DTU is well on its way towards this goal [34, 35]. However, presently, due to the many attributes of this well-known catalyst and electrode structure, nearly all established SOC manufactures employ Ni [36]. Solving this issue without replacing the Ni catalyst would thus be extremely cost-efficient.

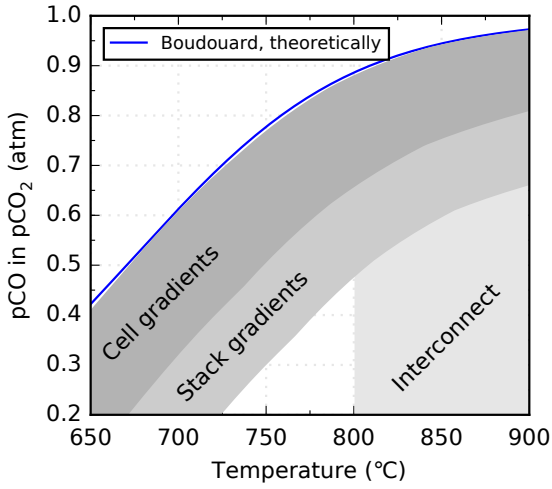

Figure 3.4: A qualitative representation of the various restrictions on the possible operating window of a CO_2-electrolysis system.

If the nickel particles could be completely covered, and stay covered, by for instance CGO or Cu, the coking tolerance may be improved [37]. Both Cu and ceria are known to have low catalytic activity towards carbon deposition [23, 38, 39]. However, complete and especially lasting coverage will be difficult to achieve. Moreover, infiltrating a material will also decrease the porosity, which, as shown, is not desirable. Lastly, infiltration as a means of improving coking tolerance has only been successfully demonstrated in CH_4 gas atmospheres in fuel cell mode [40], but not in CO_2-electrolysis mode.

Infiltration of the fuel electrode with Cu and CGO was attempted as a carbon deposition mitigation strategy. However, as seen in Fig. 3.5, the coking tolerance was not improved and the infiltrated cells actually showed lower tolerance. The lower porosity (here estimated to 2%-3%units lower) affected the carbon deposition negatively as expected. As seen in Fig. 3.3a, a 3% lower porosity will approximately give the same results as found for the infiltrated cells. The negative effect can thus be ascribed to the lower porosity.

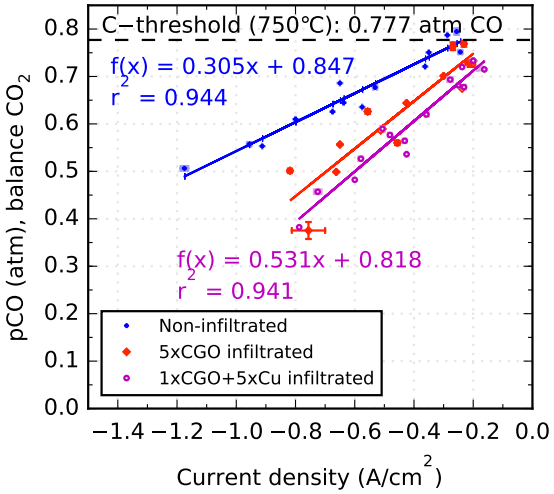

Figure 3.5: Three different cells with 30% porosity were infiltrated and operated at 750 °C with air to the oxygen electrode. The outlet gas concentration where carbon deposition was found to take place, as found by means of iV-experiments, is plotted against current density.

Another way to cover the Ni particles is by use of sulfur. This is a technique known from heterogeneous catalysis used for steam reforming of methane by means of a Ni catalyst, so-called sulfur passivation [41]. While it is well-known that sulfur is a

detrimental impurity in SOFC-mode [33, 42–45], little is known about the impact during electrolysis operation, especially with CO and CO_2. However, Ebbesen et al. found remarkable improvements in durability by cleaning the inlet gas during CO_2 electrolysis [9]. The effect was ascribed to sulfur in the inlet gases, estimated to 5-8 ppb on account of the specifications from the gas supplier.

During preliminary investigations on the effect of S on CO_2-electrolysis, it was indeed found that as little as 5 ppb, as opposed to ppm-levels for SOFC operation [42–45], had a negative effect on the degradation rate. H_2S was flowed on and off for 24 h at a time, increasing the amount each time it was turned on. The degradation rate was estimated for each step and is shown in Fig. 3.6. Nearly every time H_2S was flowing, the degradation rate increased. Curiously, the exception was while crossing the thermoneutral voltage at approximately 1.5 V. At 20 ppb, the voltage increased dramatically to 1.85 V. Interestingly, the poisoning appeared to be semi-reversible, as the degradation rate returned to the rate observed before adding H_2S, but the absolute voltage did not. Other cell test experiments with 0.5-2 ppm of H_2S, both with and without current running through the cell, confirmed the very strong effect of sulfur poisoning during CO_2-electrolysis. With such concentrations, the cell was completely deactivated within hours.

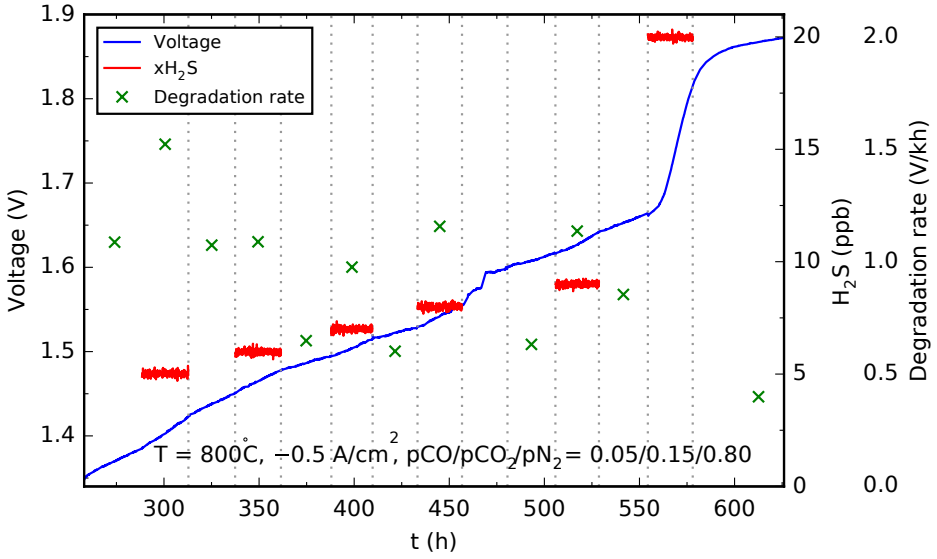

Figure 3.6: Voltage while flowing H_2S stepwise from 5 ppb to 20 ppb, and the corresponding degradation rate at each step.

Two things are important to note in relation to this experiment. Firstly, achieving such low H_2S concentrations required operation of mass-flow-controllers close to the lower recommended threshold for gas flows. Absolute trust should not be put on the exact values and they should rather be regarded as approximations. Secondly, visual inspection after this test revealed carbon dust on the fuel electrode and similar electrode/electrolyte delamination as shown earlier was found with SEM. While the initial effect of H_2S on the degradation rate is not questioned, the sudden jump in voltage after 8 ppb or the large voltage increase after 20 ppb, could be related to carbon formation. Two possible hypotheses explaining these observations are; [a)] this could have occurred due to current only flowing through a certain part of the cell, as the rest could have been left electrochemically inactive due to S coverage of the Ni-catalyst. This would increase the local current density and as shown this increases the likelihood of carbon formation. However, this explanation is questionable since the carbon was primarily found to deposit at the fuel inlet part of the cell, the part where the majority of the sulfur is likely to deposit first. [b)] Thermodynamically it is expected that when the overpotential on the fuel electrode is high enough, carbon formation will occur. This phenomenon will be further investigated in chapter 4. Thus, once the poisoning has increased the overpotential sufficiently, carbon starts forming. This could potentially also have implications on long-term operation in constant current mode, as the overpotential of the fuel electrode will be increasing with time. The local conditions in the electrode could eventually cross the thermodynamic threshold and suddenly coke. This could potentially be avoided by operating with constant voltage. However, at the time of writing, this has not yet been observed experimentally.

The sulfur passivation experiment was performed by conducting similar iV measurements as described earlier, after having flowed a certain amount of H_2S. Initial measurements before flowing H_2S, showed that carbon formed at ~70% CO in the outlet, ~8%-units lower than expected from global thermodynamic calculations under these conditions. This is in full agreement with the previously reported results. With the dramatic effect of sulfur shown during CO_2-electrolysis, the test was started with flowing a small amount of H_2S into the cell, 6 ppb for 1 min. The amount was gradually increased up to what corresponded to having flown 100 ppb H_2S for more than 50 h. As seen in Fig. 3.7, at no point did the sulfur have a positive effect on the carbon tolerance.

3.5 Conclusions

A simple technique for detecting carbon deposition during CO_2 electrolysis in operating solid oxide cells has been developed. The method was used to estimate

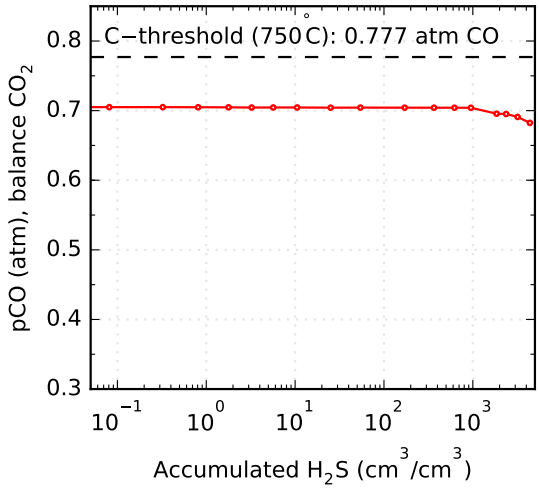

Figure 3.7: The outlet gas concentration where carbon deposition was found to take place as found by means of iV-experiments is plotted against the accumulated H_2S flown into the cell.

the deviation of the measured onset of carbon deposition from that expected from thermodynamic calculations based on averaged cell measurements. The deviation is caused by gradients of temperature, current density and gas concentrations within the cell. It was found that both current and fuel electrode porosity had high impacts on the onset of carbon formation.

It is concluded that these gradients throughout the electrode as well as in the entire stack will severely reduce the possible operating window of a commercial SOEC system during CO_2-electrolysis operation. Depending on the specific cells, stack and operating conditions, the possible product output of the system can be up to 50% lower than expected based on the thermodynamic carbon deposition threshold at the inlet temperature. Under realistic stack operating conditions, the CO outlet concentration is thus in practice limited to around 50%.

The effect can be mitigated by increasing the fuel electrode porosity, or by adjusting the operational conditions, e.g. operating with lower current density or higher temperature. However, these approaches will not resolve the issue entirely. Three other mitigation strategies were tested, none of which were successful, but there are still many possibilities that remain to be tested in a SOC context. However, replacing the Ni-catalyst is likely to be the only lasting solution, although a complete cell redesign is required as these cells, similar to most other industrial cells,

are fuel electrode supported. Finally, sulfur has been shown to be a significant source of degradation during CO_2-electrolysis, necessitating the use of thorough gas cleaning to reduce sulfur concentrations to below 5-10 ppb.

3.6 Supporting Information

3.6.1 Gas composition calculations

The gas composition at the outlet during the maximum current step is estimated using Faraday's law of electrolysis, eq. S.3.1, and the ideal gas law, eq. S.3.2.

$$\dot{n}_I = \frac{I}{nF} \tag{eq. S.3.1}$$

$$\dot{n}_{gas} = \frac{P\dot{V}_{reac.}}{RT} \tag{eq. S.3.2}$$

Where $\dot{n}_I$ is the molar flow of reactants converted by the current, I is the current, n is number of electrons (2 in this case), F is Faraday's constant, $\dot{n}_{gas}$ is the molar flow of reactants supplied in the inlet gas, P is pressure (1 atm in this case), $\dot{V}_{reac.}$ is the volumetric flow of reactants in the inlet gas, R is the gas constant and T is the temperature. FU can be estimated by eq. S.3.3, and the concentration of the product, CO, at the fuel outlet can thus be found using eq. S.3.4.

$$F_U = \frac{\dot{n}_I}{\dot{n}_{gas}} \tag{eq. S.3.3}$$

$$x_{prod.} = F_U \frac{\dot{V}_{reac.}}{\dot{V}_{reac.} + \dot{V}_{prod.}} + \frac{\dot{V}_{prod.}}{\dot{V}_{reac.} + \dot{V}_{prod.}} \tag{eq. S.3.4}$$

3.6.2 Partial oxygen pressure at time of coking

The expected partial oxygen pressure, $p\mathrm{O}_2$, can be calculated according to the amount of CO produced during the slow iV experiment. Although not entirely consistent in all cases, sudden fluctuations in the measured $p\mathrm{O}_2$ were observed, as seen in Fig. S.3.2b. Such $p\mathrm{O}_2$ fluctuations were never observed when drawing

current far from the Boudouard threshold and where no voltage fluctuations or hysteresis was observed. The higher pO_2 may be related to intermediate reactions such as direct decomposition of CO, eq. S.3.5, or CO_2, eq. S.3.6. Whether these reactions are occurring will be discussed in chapter 4.

$$CO \rightleftharpoons C + \frac{1}{2}O_2 \qquad \text{(eq. S.3.5)}$$

$$CO_2 \rightleftharpoons C + O_2 \qquad \text{(eq. S.3.6)}$$

3.6.3 Electrochemical impedance spectroscopy

Impedance measurements were carried out using a Solartron 1252A and a measurement resistor [46]. The impedance data was corrected using the short-circuit response of the test set-up. Furthermore, remaining stray inductance was calculated using a Kramers-Kronig procedure and subtracted from the data. The frequency range was 0.08–96850 Hz with 12 points per decade and an AC perturbation amplitude of 60 mA RMS. Analysis of the impedance data was performed using impedance transforms in the software Ravdav [47].

EIS spectra were recorded before and after each iV-curve in the same CO/CO_2 atmosphere during OCV. The increase after each iV curve of the arc related to the fuel electrode at 1000 - 4000 Hz (as shown previously, e.g. [48, 49]) can be seen in Fig. S.3.4 for the CO/CO_2 atmosphere. Performing similar iV curves in a H_2/H_2O atmosphere before the cell was coked did not cause such an increase in the fuel electrode arc. It is thus confirmed that the voltage increase is caused by changes in the fuel electrode. It is also noted that the iV curves and the formation of minor amounts of carbon does in fact cause permanent damage to the cell. The formed carbon has already changed the microstructure by initiating minor, local areas of delamination between the fuel electrode and the electrolyte as shown in Fig. S.3.3. Another explanation could be a decreased contact area between the individual Ni and YSZ particles in the electrode. Although this was not observed directly during microscopy analysis, it cannot be ruled out.

3.6.4 Raman spectroscopy

No significant signal from ex-situ Raman spectroscopy of cross-sections of the fuel electrode of a tested cell was detected at the relevant Raman shifts, i.e. D-peak at 1359 cm^{-1} and G-peak at 1580 cm^{-1} [22, 50], as seen in Fig. S.3.5. This

suggests that [a)] very small amounts of surface carbon was formed, below the detection limit for ordinary Raman spectroscopy and surface-enhanced Raman spectroscopy (SERS), would be needed [18], or [b)] the carbon has been oxidized before ending the cell test, perhaps even immediately after it was deposited as the electrolysis current was decreased, and *operando* Raman spectroscopy would be needed.

3.6.5 Figures for supporting information

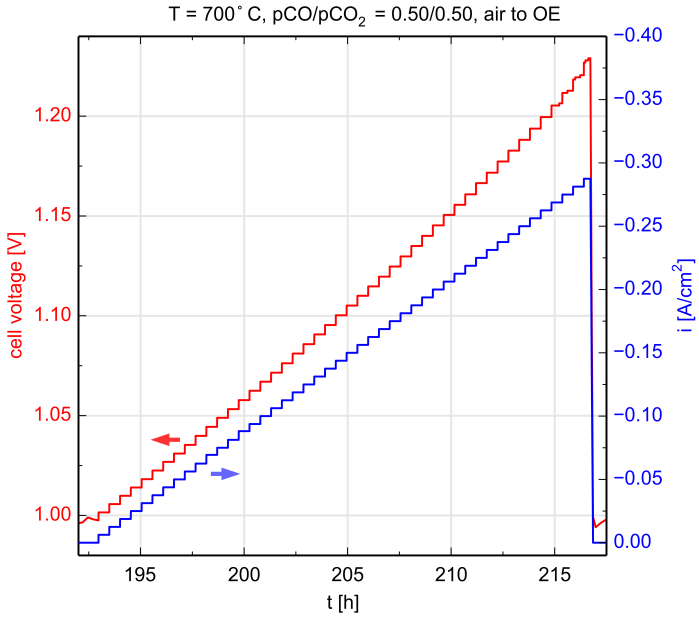

Figure S.3.1: Voltage and current density against time for an iV curve with step-size of 0.1 A and step-time of 0.5 h. As can be seen, the voltage becomes unstable within the last 3 h.

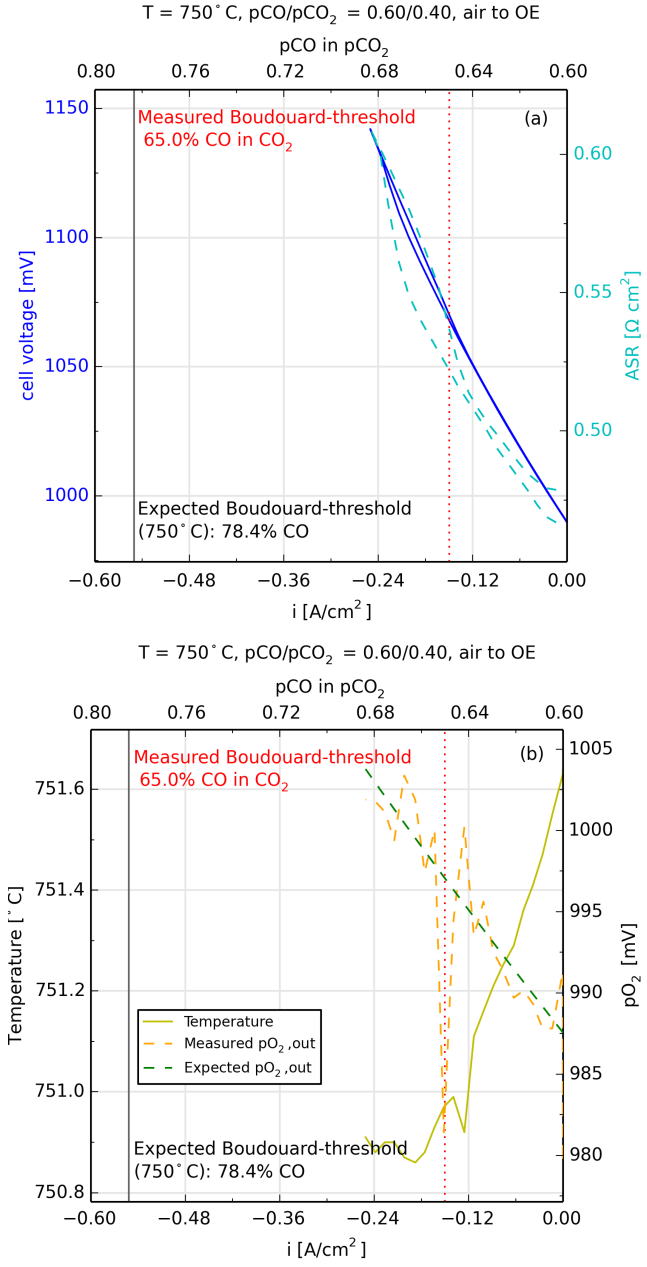

Figure S.3.2: (a) Cell voltage and area-specific resistance, and (b) fuel electrode surface temperature, and expected and measured pO_2 at the gas outlet.

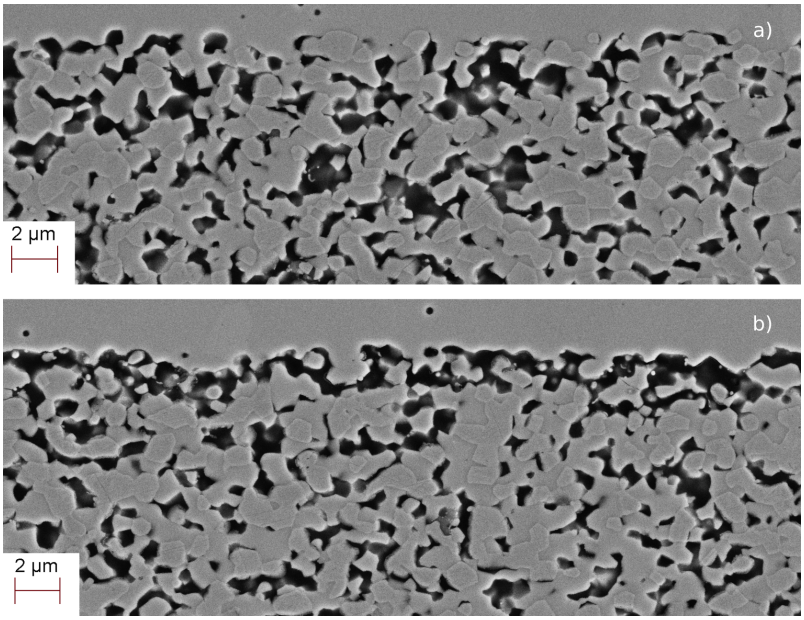

Figure S.3.3: Scanning electron micrographs of the same cell after conducting iV-experiments. Delamination was observed in minor parts of the cell, at the electrode-electrolyte interface.

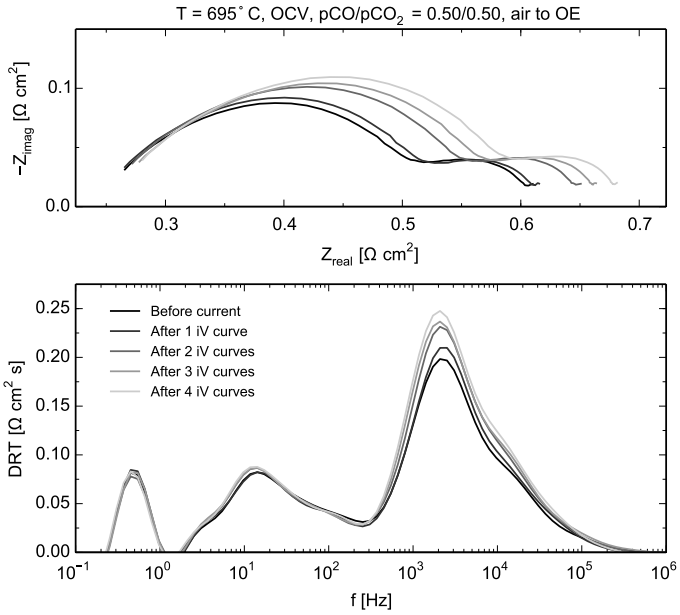

Figure S.3.4: Nyquist and DRT [51] spectra of impedance measurements depicting the increase in resistance for the fuel electrode in a CO/CO_2 atmosphere after measuring 4 iV curves.

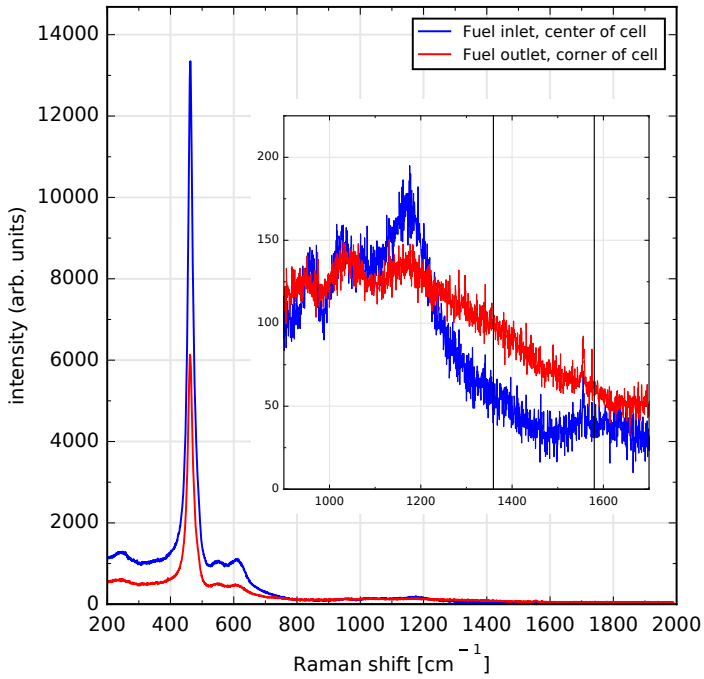

Figure S.3.5: Raman spectroscopy of the cross-section near the electrolyte of a tested cell. The insert is zooming on the D- and G-shifts related to carbon.

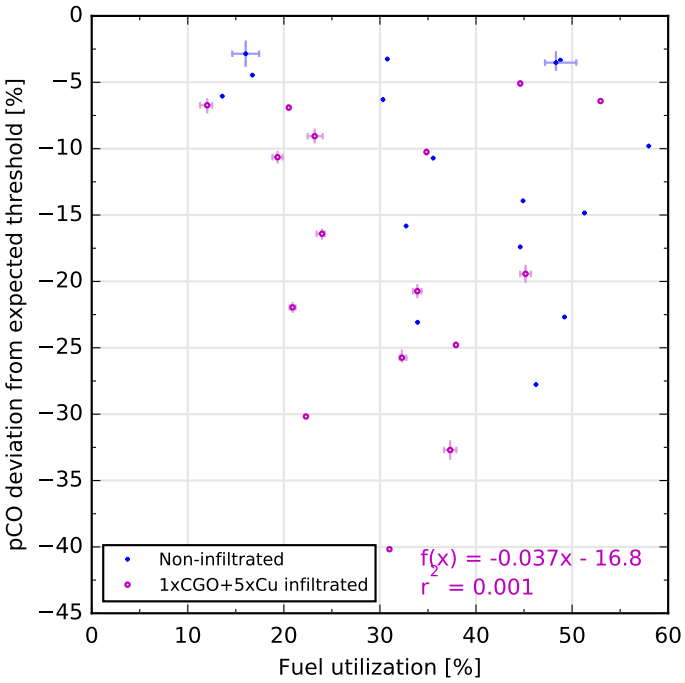

Figure S.3.6: Two different cells were operated at 750 °C with air to the oxygen electrode. The deviation in CO gas concentration from the expected Boudouard threshold as found by means of iV-experiments is plotted against fuel utilization.

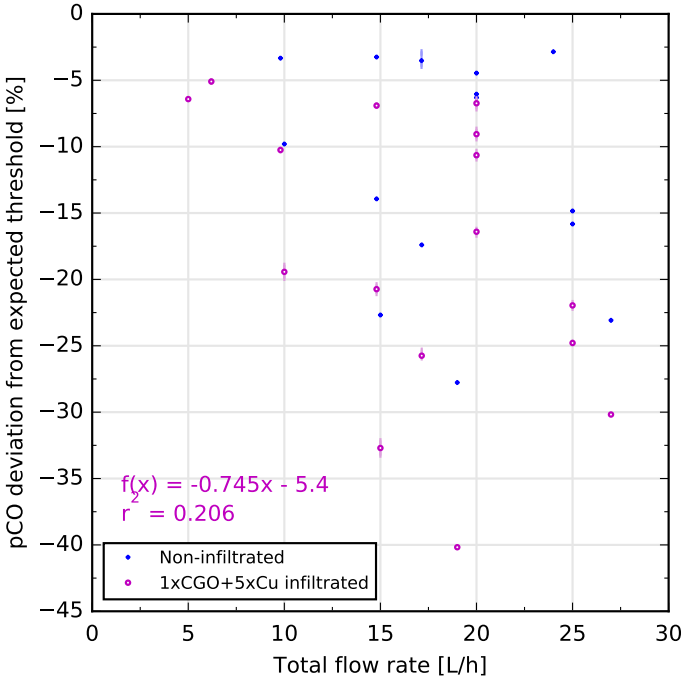

Figure S.3.7: Two different cells were operated at 750 °C with air to the oxygen electrode. The deviation in CO gas concentration from the expected Boudouard threshold as found by means of iV-experiments is plotted against total fuel gas flow.

3.7 References

1. Ebbesen, S. D., Jensen, S. H., Hauch, A. & Mogensen, M. B. High Temperature Electrolysis in Alkaline Cells, Solid Proton Conducting Cells, and Solid Oxide Cells. *Chemical Reviews* **114,** 10697–10734 (Nov. 2014).
2. Hauch, A., Ebbesen, S. D., Jensen, S. H. & Mogensen, M. Highly efficient high temperature electrolysis. *Journal of Materials Chemistry* **18,** 2331 (2008).
3. Ebbesen, S. D., Graves, C. & Mogensen, M. Production of Synthetic Fuels by Co-Electrolysis of Steam and Carbon Dioxide. *International Journal of Green Energy* **6,** 646–660 (Dec. 2009).
4. Jensen, S. H., Larsen, P. H. & Mogensen, M. Hydrogen and synthetic fuel production from renewable energy sources. *International Journal of Hydrogen Energy* **32,** 3253–3257 (Oct. 2007).
5. Skov, I. R. *et al. The role of electrolysers in energy system - Energy markets, grid stabilisation and transport fuels* tech. rep. (Aalborg University, 2016).
6. Crabtree, G. W., Dresselhaus, M. S. & Buchanan, M. V. The Hydrogen Economy. *Physics Today* **57,** 39–44 (2004).
7. Graves, C., Ebbesen, S. D., Mogensen, M. & Lackner, K. S. Sustainable hydrocarbon fuels by recycling CO_2 and H_2O with renewable or nuclear energy. *Renewable and Sustainable Energy Reviews* **15,** 1–23 (Jan. 2011).
8. Lackner, K. S. Capture of carbon dioxide from ambient air. *European Physical Journal: Special Topics* **176,** 93–106 (2009).
9. Ebbesen, S. D. & Mogensen, M. Electrolysis of carbon dioxide in Solid Oxide Electrolysis Cells. *Journal of Power Sources* **193,** 349–358 (Aug. 2009).
10. Sridhar, K. & Vaniman, B. Oxygen production on Mars using solid oxide electrolysis. *Solid State Ionics* **93,** 321–328 (1997).
11. Hartvigsen, J. J. *et al.* Challenges of Solid Oxide Electrolysis for Production of Fuel and Oxygen from Mars Atmospheric CO_2. *ECS Transactions* **68,** 3563–3583 (July 2015).
12. Meyen, F. E., Hecht, M. H. & Hoffman, J. A. Thermodynamic model of Mars Oxygen ISRU Experiment (MOXIE). *Acta Astronautica* **129,** 82–87 (Dec. 2016).
13. Zubrin, R. M., Muscatello, A. C. & Berggren, M. Integrated Mars In Situ Propellant Production System. *Journal of Aerospace Engineering* **26,** 43–56 (Jan. 2013).

14. Tavares, M. T., Alstrup, I., Bernardo, C. A. & Rostrup-Nielsen, J. R. CO Disproportionation on Silica-Supported Nickel and Nickel-Copper Catalysts. *Journal of Catalysis* **147,** 525–534 (1994).

15. Rostrup-Nielsen, J. R. & Alstrup, I. Innovation and science in the process industry: steam reforming and hydrogenolysis. *Catalysis today* **53,** 311–316 (1999).

16. Tao, Y., Ebbesen, S. D., Zhang, W. & Mogensen, M. B. Carbon Nanotube Growth on Nanozirconia under Strong Cathodic Polarization in Steam and Carbon Dioxide. *ChemCatChem* **4000** (Feb. 2014).

17. Tao, Y., Ebbesen, S. D. & Mogensen, M. B. Carbon Deposition in Solid Oxide Cells during Co-Electrolysis of H_2O and CO_2. *Journal of the Electrochemical Society* **161,** F337–F343 (Jan. 2014).

18. Li, X. *et al.* An operando surface enhanced Raman spectroscopy (SERS) study of carbon deposition on SOFC anodes. *Phys. Chem. Chem. Phys.* **17,** 21112–21119 (2015).

19. Subotić, V. *et al.* Anode regeneration following carbon depositions in an industrial-sized anode supported solid oxide fuel cell operating on synthetic diesel reformate. *Journal of Power Sources* **295,** 55–66 (2015).

20. Subotić, V., Schluckner, C., Schroettner, H. & Hochenauer, C. Analysis of possibilities for carbon removal from porous anode of solid oxide fuel cells after different failure modes. *Journal of Power Sources* **302,** 378–386 (2016).

21. Maher, R. C. *et al.* Raman Spectroscopy of Solid Oxide Fuel Cells: Technique Overview and Application to Carbon Deposition Analysis. *Fuel Cells* **13,** 455–469 (Aug. 2013).

22. Duboviks, V. *et al.* A Raman spectroscopic study of the carbon deposition mechanism on Ni/CGO electrodes during CO/CO_2 electrolysis. *Physical Chemistry Chemical Physics* **16,** 13063 (2014).

23. Duboviks, V. *et al.* Carbon deposition behaviour in metal-infiltrated gadolinia doped ceria electrodes for simulated biogas upgrading in solid oxide electrolysis cells. *Journal of Power Sources* **293,** 912–921 (2015).

24. Li, W., Shi, Y., Luo, Y., Wang, Y. & Cai, N. Carbon deposition on patterned nickel / yttria stabilized zirconia electrodes for solid oxide fuel cell / solid oxide electrolysis cell modes. *Journal of Power Sources* **276,** 26–31 (2015).

25. Skafte, T. L., Graves, C., Blennow, P. & Hjelm, J. Carbon Deposition during CO_2 Electrolysis in Ni-Based Solid-Oxide-Cell Electrodes. *ECS Transactions* **68,** 3429–3437 (2015).

26. Ebbesen, S. D., Sun, X. & Mogensen, M. B. Understanding the processes governing performance and durability of solid oxide electrolysis cells. *Faraday discussions* **182,** 393–422 (2015).

27. Duhn, J. D., Jensen, A. D., Wedel, S. & Wix, C. Modelling of gas diffusion limitations in Ni/YSZ electrode material in CO_2 and co-electrolysis. *EFCF 2016 proceedings,* B0810 (2016).

28. Navasa, M., Graves, C., Chatzichristodoulou, C., Skafte, T. L. & Sund, B. A Three Dimensional Multiphysics Model of a Solid Oxide Electrochemical Cell for Degradation Studies. *In manuscript* (2017).

29. Navasa, M. *Three Dimensional Multiphysics Modeling of Reversible Solid Oxide Electrochemical Cells for Degradation Studies Three Dimensional Multiphysics Modeling of Reversible Solid Oxide Electrochemical Cells for Degradation Studies* PhD thesis (Lund University, 2016).

30. Navasa, M., Frandsen, H. L., Skafte, T. L., Sundén, B. & Graves, C. Localized Carbon Deposition in Solid Oxide Electrolysis Cells Studied by Multiphysics Modeling. *In manuscript* (2017).

31. Blennow, P. *et al.* Understanding lifetime limitations in the Topsoe Stack Platform using modeling and post mortem analysis. *EFCF 2016 proceedings,* A1102 (2016).

32. Liu, C.-j., Ye, J., Jiang, J. & Pan, Y. Progresses in the Preparation of Coke Resistant Ni-based Catalyst for Steam and CO_2 Reforming of Methane. *ChemCatChem* **3,** 529–541 (Mar. 2011).

33. Boldrin, P. *et al.* Strategies for Carbon and Sulfur Tolerant Solid Oxide Fuel Cell Materials, Incorporating Lessons from Heterogeneous Catalysis. *Chemical Reviews* **116,** 13633–13684 (Nov. 2016).

34. Skafte, T. L., Sudireddy, B. R., Blennow, P. & Graves, C. Carbon and Redox Tolerant Infiltrated Oxide Fuel-Electrodes for Solid Oxide Cells. *ECS Transactions* **72,** 201–214 (May 2016).

35. Graves, C., Martinez, L. & Sudireddy, B. R. High Performance Nano-Ceria Electrodes for Solid Oxide Cells. *ECS Transactions* **72,** 183–192 (May 2016).

36. Skafte, T. L., Hjelm, J., Blennow, P. & Graves, C. Quantitative review of degradation and lifetime of solid oxide cells and stacks. *EFCF 2016 proceedings,* B0501 (2016).

37. Lee, J. G. *et al.* Durable and High-Performance Direct-Methane Fuel Cells with Coke-Tolerant Ceria-Coated Ni Catalysts at Reduced Temperatures. *Electrochimica Acta* **191,** 677–686 (2016).

38. Wang, S., Lu, G. Q. & Millar, G. J. Carbon Dioxide Reforming of Methane To Produce Synthesis Gas over Metal-Supported Catalysts: State of the Art. *Energy & Fuels* **10,** 896–904 (Jan. 1996).

39. Brett, D. J. *et al.* Methanol as a direct fuel in intermediate temperature. *Chemical Engineering Science* **60,** 5649–5662 (Nov. 2005).

40. Rostrup-Nielsen, J. R. Equilibria of decomposition reactions of carbon monoxide and methane over nickel catalysts. *Journal of Catalysis* **27,** 343–356 (1972).

41. Rostrup-Nielsen, J. R. Sulfur-passivated nickel catalysts for carbon-free steam reforming of methane. *Journal of Catalysis* **85,** 31–43 (1984).

42. Hagen, A., Rasmussen, J. F. & Thydén, K. Durability of solid oxide fuel cells using sulfur containing fuels. *Journal of Power Sources* **196,** 7271–7276 (Sept. 2011).

43. Hansen, J. B. Correlating Sulfur Poisoning of SOFC Nickel Anodes by a Temkin Isotherm. *Electrochemical and Solid-State Letters* **11,** B178 (2008).

44. Hauch, A., Hagen, A., Hjelm, J. & Ramos, T. Sulfur Poisoning of SOFC Anodes: Effect of Overpotential on Long-Term Degradation. *Journal of the Electrochemical Society* **161,** F734–F743 (May 2014).

45. Rostrup-Nielsen, J., Hansen, J., Helveg, S., Christiansen, N. & Jannasch, A. Sites for catalysis and electrochemistry in solid oxide fuel cell (SOFC) anode. *Applied Physics A* **85,** 427–430 (Sept. 2006).

46. Barsoukov, E. & Macdonald, J. *Impedance Spectroscopy: Theory, Experiment, and Applications* (Wiley, 2005).

47. Graves, C. *RAVDAV data analysis software, version 0.9.8.* 2015.

48. Barfod, R. *et al.* Detailed Characterization of Anode-Supported SOFCs by Impedance Spectroscopy. *Journal of The Electrochemical Society* **154,** B371 (2007).

49. Graves, C. & Hjelm, J. Advanced impedance modeling of solid oxide electrochemical cells. *EFCF 2014 proceedings,* B1203 (2014).

50. Duboviks, V., Maher, R. C., Offer, G., Cohen, L. F. & Brandon, N. P. In-Operando Raman Spectroscopy Study of Passivation Effects on Ni-CGO Electrodes in CO_2 Electrolysis Conditions. *ECS Transactions* **57,** 3111–3117 (Oct. 2013).

51. Schichlein, H. & Ivers-tiffe, E. Deconvolution of electrochemical impedance spectra for the identification of electrode reaction mechanisms in solid oxide fuel cells. *Journal of Applied Electrochemistry* **32,** 875–882 (2002).

4 Inhibiting carbon formation

As discussed in the previous chapter, decreasing the likelihood of carbon formation and increasing the tolerance towards already formed carbon would drastically increase the possible operating window of the operation mode in question. As shown, attempts at modifying the already well-established Ni-based electrode has proven to be unsuccessful. However, the case is influenced by other factors, such as gas diffusion limitations in the porous structure, thermal gradients caused by the occurring reactions and agglomeration of the Ni particles. To study the phenomenon of carbon formation in detail we now turn to the surface sensitive technique NAPXPS. Focusing on the carbon formation mechanism excluding the mentioned unwanted factors can be achieved by utilizing model electrodes and a slightly lower temperature. We will investigate the reactions occurring at the Ni/YSZ interface during operation, as well as on doped ceria with and without Ni present. As will be discussed, ceria has been reported to inhibit the formation of carbon and is thus an attractive material to examine for mitigation purposes. However, little is known about the exact reasons for the higher tolerance and here we will attempt to shed light on this subject.

The following pages are based on the 3^{rd} publication: Electrochemically driven carbon deposition from CO_2 on nickel and ceria electrodes: Reaction and inhibition mechanisms.

4.1 Abstract

The solid oxide electrochemical cell is a promising technology for efficient energy storage, but state-of-the-art nickel-based electrodes are susceptible to destructive carbon formation during operation. Certain oxide electrode materials, such as samarium-doped ceria (SDC), have been reported as less susceptible. Here we investigated the mechanisms by which carbon deposition occurs during CO_2 reduction using dense thin-film electrodes as model systems to understand the role of Ni, YSZ, and SDC. The presence of carbon and surface adsorbates was measured with NAPXPS at 550 °C in 0.5 Torr CO:CO_2 (1:1). We found that carbon formation initiated at different applied electrical potentials – it was inhibited for

ceria-containing electrodes – and varying the potential reversibly increased and decreased the surface converage, with hysteresis. Carbon-nanotubes (CNT) grew on Ni-YSZ, while ceria formed an amorphous carbon layer less likely to cause mechanical damage to the electrode. The potential dependent spectroscopy data elucidates the role of carbonates and other oxidized carbon species on the ceria surface in inhibiting carbon deposition.

4.2 Introduction

The ability of SOCs to oxidize H_2/CO and reduce H_2O/CO_2 makes them potentially important players in sustainable energy scenarios such as the hydrogen economy [1] or the closed loop CO_2 economy [2]. Electrochemical splitting of CO_2 into CO and O_2 can provide storage of intermittent solar and wind power and conversion of otherwise-emitted CO_2 into more valuable products, i.e. hydrocarbons, synthetic fuels and CO [2]. Such CO_2-recycling may increase the value of CO_2 and incentivize further investments in carbon capture and storage. Having recently crossed the limit of 400 ppm CO_2 in the atmosphere [3], extracting greenhouse gases from emitters or directly from the air [4] is likely required to avoid catastrophic and costly effects of climate change. Another application showcasing the technical possibilities is as a rocket fuel production unit or as part of a life support system on Mars utilizing the CO_2-rich atmosphere [5, 6].

Most commercial SOC systems currently utilize the well-known Ni electrocatalyst in the fuel electrode [7]. Unfortunately, Ni is also an excellent catalyst for carbon formation [8, 9], which destroys the porous electrode [10–13]. Carbon formation is a well-known issue in heterogeneous catalysis during steam reforming [14–17] and during fuel cell operation with hydrocarbons in SOCs [18–20], but has been far less studied for CO_2 electrolysis. During electrolysis, gradients of gas concentration, temperature and overpotential caused by high current density have been shown to cause carbon formation at the electrode/electrolyte interface [21–23] even when operating the system far from the thermodynamic threshold [12, 13, 21].

The gradients known to exist in the electrode could increase the CO concentration and lower the temperature such that the responsible carbon forming reaction would be the traditional CO disproportionation, also known as the Boudouard reaction:

$$2CO_{(g)} \rightarrow C_s + CO_{2(g)} \qquad \text{(eq. 4.1)}$$

With the subscript "(g)" denoting a gas phase specie and "s" a surface specie. However, it has also been speculated and to a certain extent demonstrated that

electrochemical carbon deposition reactions can occur, such as the reactions in eq. 4.2 and eq. 4.3 [22–27].

$$CO_{2(g)} + 4e^- \rightarrow C_s + 2O^{2-} \quad \text{(eq. 4.2)}$$

$$CO_{(g)} + 2e^- \rightarrow C_s + O^{2-} \quad \text{(eq. 4.3)}$$

Designing carbon tolerant electrodes has so far mostly been empirical in nature. Doped ceria has been observed to inhibit carbon formation [28–32], but the reason is poorly understood and often simply proposed to be related to the high oxygen-storage capacity. *Operando* surface sensitive techniques are needed to further our fundamental understanding of the governing reactions and thus our capabilities of mitigating the issue [33].

Here, we employ synchrotron-based XPS at near-ambient pressure and elevated temperature while simultaneously applying an electrical potential to different model electrodes. These are schematically shown in Fig. 4.1; [a)] a SDC surface, [b)] a SDC surface with randomly dispersed Ni nanoparticles (Ni-SDC), and [c)] a YSZ surface with dispersed Ni nanoparticles and a Ni pattern for electronic percolation (Ni-YSZ). These samples constitute three different types of reaction zones; 2PB, 3PB and a mixed 2PB/3PB for SDC, Ni-YSZ and Ni-SDC, respectively. Comparing the Ni-SDC and Ni-YSZ samples elucidated the effect of different oxide substrates. Analyzing the surface for intermediates provided novel insights into the mechanism of the carbon suppressing ability of doped ceria. The experiments were designed to decrease the probability of thermochemical carbon deposition, eq. 4.1, so as to facilitate investigation of electrochemical carbon deposition, eq. 4.2 and eq. 4.3.

The experiments were carried out at 550 °C in a 1:1 CO:CO_2 atmosphere with a total pressure of 150 mTorr (0.2 mbar) for the SDC sample, and 480-500 mTorr (0.66 mbar) for the Ni-SDC and Ni-YSZ samples. The thermodynamic carbon deposition threshold changes with pressure, but only minutely in the pressure range employed here (~2% CO). Under these conditions the threshold is ~98% CO balanced by CO_2 and thermochemical carbon formation was thus not expected. However, by increasing the cathodic overpotential on the working electrode the threshold can be crossed. In this case, the threshold is approximately −125 mV ±25 mV (cathodic), assuming a 20 °C temperature accuracy (see Supporting Information for calculations). By changing the bias from anodic to gradually more cathodic and monitoring the XPS spectra, we were able to determine with high sensitivity the onset potential of electrochemically driven carbon deposition for each electrode and examine the surface species before and during deposition.

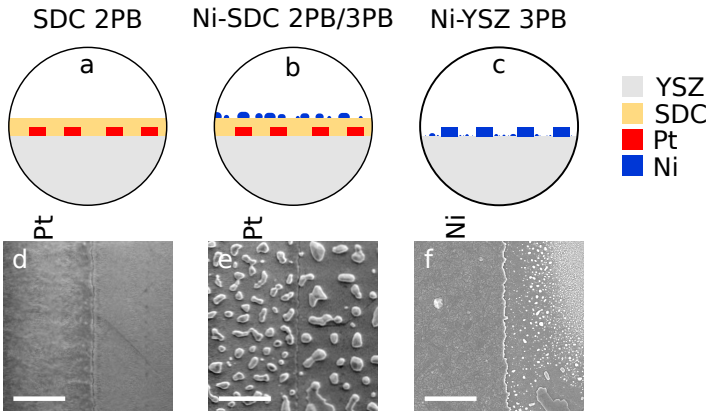

Figure 4.1: Model electrodes employed to study carbon deposition on different surfaces. a-c, illustrations of the SDC, Ni-SDC and Ni-YSZ electrodes, with a buried Pt pattern for the SDC samples. d-f, planar SEM images of the surfaces and interfaces. The Ni-YSZ electrode had <40 nm Ni particles next to the pattern. Scalebar is 2 μm.

4.3 Results

4.3.1 Carbon formation

Controlling the deposition of carbon is possible for all samples, as seen from the peak growing at ~285 eV in Fig. 4.2. As will be discussed later, other peaks at higher BE are also visible, i.e. CO_3^{2-} (carbonate, from now on referred to as CO_3) at ~290.5 eV and various oxidation groups between the carbonate and carbon peaks. For a comprehensive analysis of peak assignment and fitting, please see the Supporting Information. Even on the SDC sample, which lacks a conventional metal catalyst, carbon formation occurred. This is known to be possible with a sufficiently high driving force [24, 34]. By applying an anodic potential the carbon was oxidized again. Lastly, upon return to cathodic conditions, the carbon re-deposited.

The Ni-YSZ sample had adventitious carbon on the surface from the beginning of the experiment, as seen in Fig. 4.2c. As this sample was prepared with a metallic Ni pattern susceptible to Ni-oxidation, it was not possible to flow oxygen to burn off any adventitious carbon which is commonly present on all samples exposed to atmospheric air. For Ni-YSZ, neither the carbon peak nor the lattice oxygen peak from O 1s (529.9 eV at 0 mV) changed significantly during the first

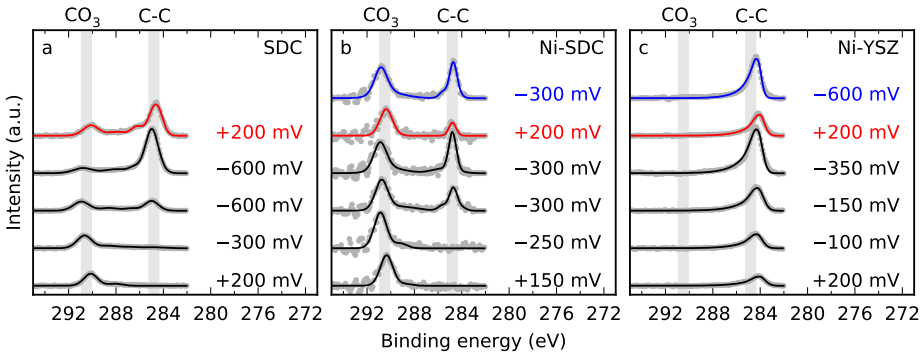

Figure 4.2: Carbon formation and oxidation as the overpotential is varied. XPS spectrum of C 1s from a signal depth of 0.6 nm showing the dependence of the carbon peak at ~285 eV on the applied overpotential for a, the SDC, b, the Ni-SDC and c, the Ni-YSZ electrode. The arrows indicate the chronological order of measurements. A change in color highlights a change in sweeping direction, black (—) and blue (—) indicating cathodic direction and red (—) anodic direction. The gas phase peaks for CO and CO_2 have here been fitted and removed.

10 measurements from +200 mV (anodic) to −100 mV (cathodic). However, when reaching −150 mV, the intensity of the carbon peak grew considerably and continued to do so when higher cathodic potentials were applied. A decrease in the lattice oxygen peak from O 1s at −150 mV further supports the suggested onset point of −150 mV (Fig. S.4.1). Moreover, it shows that the carbon is covering the YSZ surface.

In the current-potential curves, hysteresis was observed due to decreasing performance as carbon deposited and covered the reaction sites (see Fig. S.4.2, Fig. S.4.3 and discussion in Supporting Information). This agrees with observations of hysteresis for full-sized commercial SOECs during constant-current experiments with carbon formation [12].

4.3.2 Onset and reversibility

The onset potential at which carbon formation occurs for the different samples is illustrated in Fig. 4.3. Here, the inhibiting effect of ceria on carbon formation is clearly shown. For SDC, carbon formation occurs between −300 mV and −600 mV. For Ni-SDC, it occurs between −250 mV and −300 mV. Both of these

samples require a far more cathodic potential than the thermodynamic threshold of approximately −125 mV under the specific experimental conditions. The Ni-YSZ sample, however, deposits carbon between −100 mV and −150 mV, showing excellent correlation with the expected threshold.

Additional measurements shown for the Ni-SDC sample illustrate the reversibility of the carbon formation (Fig. 4.3). Once initiated, the carbon keeps growing at −300 mV until returning to more oxidizing conditions than the threshold (step 2.). Upon returning to −300 mV (step 3.), carbon starts growing again. Similar trends were observed for both SDC and Ni-YSZ (not shown). The same type of reversibility has been observed on porous Ni-YSZ electrodes in full-sized commercial cells [12, 13], although the amount of carbon formed must be carefully controlled as it will otherwise destroy the microstructure and delaminate the electrode from the electrolyte. Such delamination cannot occur on these model electrodes.

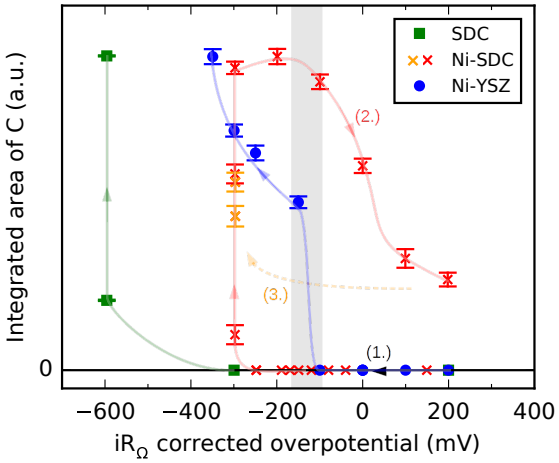

Figure 4.3: Onset of carbon formation for the different electrode surfaces and the observed reversibility shown for the Ni-SDC electrode. The integrated areas of the XPS carbon peaks are normalized to the maximum peak area. Lines are only meant to guide the eye. The chronological order of measurements is indicated by arrows. For Ni-SDC, step (1.) is sweeping in cathodic direction, step (2.) in anodic direction, and step (3.) is returning to a cathodic potential. Fitting error is indicated by error bars. The thermodynamic threshold for carbon formation is shown by the gray box, accounting for experimental uncertainties and differences.

4.3.3 Binding energy shifts

The XPS core level binding energy of different elements was investigated under applied overpotential. Changing the external electrostatic potential will change the energy difference between the Fermi level and core level if the material can be oxidized or reduced. Such a change will shift the binding energy in the XPS spectra accordingly [35, 36]. The BE of the YSZ surface should change with the applied bias in a one-to-one ratio (slope 1.0) [35, 37], as should chemically bonded adsorbates. This was confirmed for the Zr 3d, Si 2p and lattice O 1s core-level peaks (Fig. S.4.4). Ni and C have metallic band structure, and these materials will not change the distance between the Fermi- and the core-level upon biasing. Thus, we observed no shifting of the Ni 2p, 3p and C 1s peaks, except for the adventitious carbon layer on the YSZ surface, which was strongly bonded to the YSZ lattice (Fig. 4.4a-b). The valence band of Ni-SDC and Ni-YSZ was dominated by the metallic Ni feature, so no shifting of the valence band maximum was observed (Fig. S.4.4). The intermediate case is SDC, for which the Fermi level under oxidation/reduction partially moved, and the binding energy shift-slope was between 0 and 1. This was validated for both Ce 4d, Si 2p and lattice O 1s spectra, as also observed by Feng et al. [38]. The binding energy of the carbonate present on Ni-SDC and SDC changed rigidly with the SDC surface (Fig. 4.4c), which indicates strong bonding.

4.3.4 Type of carbon

As was seen in Fig. 4.2a-c, the shape of the carbon peak as well as the BE for the different samples is not identical. A more in-depth analysis of the type of carbon on the different samples follows. Carbon can exist in three different hybridizations, sp_3, sp_2 and sp_1 [39]. Sp_2 type carbon is commonly a sign of graphitic carbon, CNTs or nanofibers, while amorphous and diamond-like carbon, for instance nanodiamonds and some types of carbon nanodots [40], are made up of primarily sp_3-hybridized carbon [41]. Sp_2 carbon has slightly shorter bond length than the tetrahedral sp_3. The BE is slightly smaller for sp_2, but since carbon is homopolar, the difference is small, i.e. 0.6 eV - 0.9 eV [42–47]. Here, sp_2 was generally found at ~284.3 eV and sp_3 at ~284.7 eV. Carbon sp_2 was fitted to a blend of a Doniach-Sunjic function and a Gaussian-Lorentzian function which results in an asymmetric line shape [45, 48]. This is due to the screening of electron-hole pair excitations at the Fermi level [43]. Sp_3 carbon was fitted to a symmetric Gaussian-Lorentzian function.

As seen in Fig. 4.5a, the SDC and Ni-SDC samples have mostly sp_3 carbon. Furthermore, it is seen that especially the SDC sample has a considerable amount

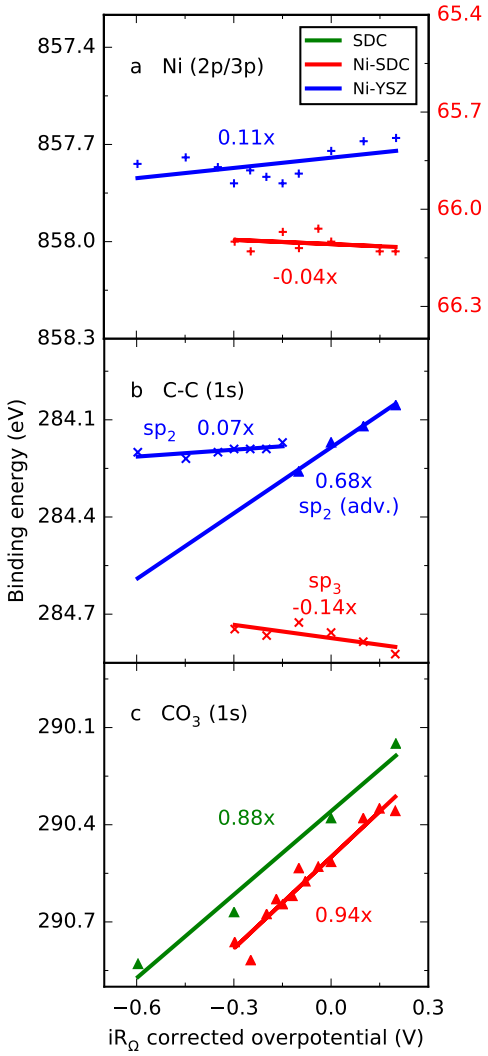

Figure 4.4: Shifts of photoemission core-level peaks for different surface species. a, Ni 2p for Ni-YSZ and Ni 3p for Ni-SDC. b, Carbon peak at ~285 eV, with a sp_2-hybridization carbon peak from adventitious carbon on YSZ and a peak for electrochemically deposited sp_2 carbon on or near nickel on Ni-YSZ, and a deposited carbon peak for Ni-SDC ascribed to sp_3-hybridization. There were insufficient data points to plot the shifting of the carbon peak for the SDC electrode. c, Carbonate shifting rigidly with the SDC surfaces. No carbonate peak was identified for the Ni-YSZ electrode.

of oxidation groups (C-O, C=O, and/or carboxylate, i.e. Ce-CO_2) at 285.8-290 eV [40, 47, 49–51]. These two observations indicate growth of amorphous or diamond-like carbon on the SDC surface. No carbon was found with SEM after testing, which could be because the carbon is deposited in a thin layer not visible with SEM, or it could be due to the shutdown procedure which is difficult to control without affecting the surface carbon.

Compared to the SDC sample, the carbon peak from the Ni-YSZ sample has a more asymmetric shape and a lower BE, indicative of sp_2 type carbon. The fitting procedure is complicated by the already present adventitious carbon on the YSZ surface, but it is clear that not all of the deposited carbon can be assigned to an sp_3 peak. The small C-O peak observed may in fact not be C-O species, but rather sp_2 plasmon [47]. The presence of sp_2 carbon suggests growth of graphitic carbon or CNTs. The latter is commonly observed for Ni catalysts [19, 52, 53] and was also confirmed here with SEM, as seen in Fig. 4.5b.

4.3.5 Adsorbates

The presence of carbonate adsorbate is known to be present on doped ceria in a CO/CO_2 atmosphere [38, 54, 55] and this is confirmed by the peak observed at ~290.5 eV [38, 50, 51, 56] in both Fig. 4.2a-b and Fig. 4.5a. As seen, no carbonate adsorbates are present on Ni-YSZ in a CO/CO_2 atmosphere (Fig. 4.2c and Fig. 4.5a). The presence of Ni carbide species was also investigated. Ni carbide BE overlaps with the main peak of C 1s (281.2 eV for NiC_x and 283.5-283.9 eV for Ni_3C) and with NiO-peaks for Ni $2p_{3/2}$ (852.9 eV for Ni_3C and 854.7-855.0 eV for $NiCO_3$ and $Ni(CO)_4$) [49, 57, 58]. The analysis is further complicated by the possible shifting of the BE of some species with overpotential. NiC_x at 281.2 eV and $NiCO_3$ and $Ni(CO)_4$ at 288.2-288.4 eV are not present in the C 1s spectrum, and the Ni $2p_{3/2}$ spectrum (Fig. S.4.5) resembles that of 100% metallic Ni in a study with no CO/CO_2 gas-species [59]. Thus, no carbides were discernable on Ni-YSZ, but it is noted that carbon atoms dissolving into Ni particles by more than a few nm will not be visible by the XPS analysis.

4.4 Discussion

In this study it has been assumed that the amount of CO produced during biasing is negligible, and unlikely to be enough to cross the thermodynamic threshold for thermochemical (gaseous or Boudouard) carbon deposition. This threshold is ~98% CO balanced by CO_2, based on the experimental conditions, far above the inlet gas composition of 50% CO balanced by CO_2. The production rate of CO

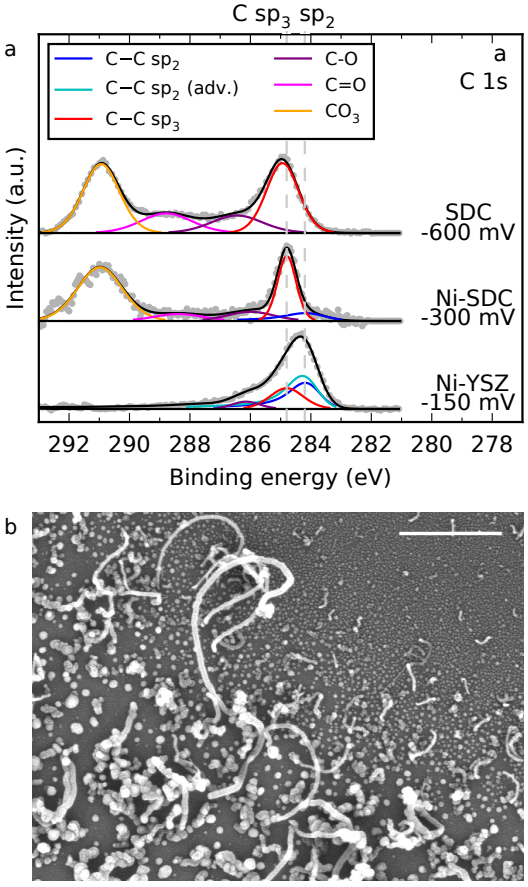

Figure 4.5: Different types of adsorbates and carbon detected on the different electrode surfaces. a, Fitting of XPS peaks for all three electrodes at the potential where carbon was first deposited. The gas phase peaks for CO and CO_2 have been fitted and removed, the background has been subtracted and carbon peak intensity has been normalized. b, Planar SEM of CNT growth on dispersed Ni nanoparticles next to the Ni pattern. Scale bar is 500 nm.

is estimated to be negligible since no significant change in the CO:CO_2-ratio was observed during polarization according to a locally probing mass-spectrometer and the gas phase XPS peak intensities (Fig. S.4.6 for Ni-SDC) – although in the case of Ni-YSZ, the XPS probing volume is much larger than the electrochemically active zone.

It has previously been suggested that carbonate participates in the reduction of CO_2 to CO on ceria [38, 54, 55]. This was based on a correlation between increased surface coverage of carbonate, the oxidation state of ceria and the applied potential. During our experiments we observed the same increase of carbonate coverage up until the most reducing condition, whereafter the carbonate coverage drops (Fig. 4.2a and Fig. S.4.7). This occurs simultaneously with carbon formation, suggesting a link between the two. The participation of carbonates in the carbon reactions has previously been suggested based on Raman spectroscopy experiments on BaO-modified Ni powder [60], but the decreasing carbonate coverage observed here may simply be explained by a carbon layer on top of the carbonate. While carbonate coverage drops, the coverage of carbon oxidation groups increases. This suggests that carbonate is reduced to the C-O, C=O and/or Ce-CO_2 species, which may be further reduced to solid carbon.

It is commonly believed that surface oxygen vacancies on doped ceria are the reason for the experimentally observed higher carbon tolerance. However, Feng et al. found that the oxygen vacancies are saturated with carbonates at reducing conditions [38]. Li et al. suggested that carbonate oxidizes the carbon into C-O groups [60], meaning carbonate is responsible for the increased carbon tolerance. However, the C-O groups have been shown with DFT models [61, 62] to provide an inhibiting effect on the deposition of carbon, and it has recently been suggested that increasing the formation rate of C-O species will increase the carbon tolerance [63]. So, these species may act as oxidizing agents on the doped ceria surface, or they may constitute additional intermediates with high formation energy barriers. Thus, the total overpotential required before the C-C species are formed is higher than for surfaces that are incapable of forming these intermediates, e.g. Ni-YSZ. Based on the observations made in this study and the mentioned reports in literature, we therefore suggest that oxygen vacancies on doped ceria assist in the formation of carbonate species that acts as intermediates for carbon formation. We have experimentally confirmed that various oxidation groups (C-O, C=O and/or Ce-CO_2) are indeed present on the surface and that the coverage of these increase at highly reducing conditions. Thus, we further suggest that the oxidation groups either inhibit the formation of carbon or oxidize the already deposited carbon. More computational modeling and experiments are required to understand exactly how the pathway from carbonate to carbon proceeds, but a suggested reaction scheme on the SDC surface is conceptually visualized in Fig. 4.6a and described in the following. CO_2 is physisorbed on the surface and reduced by a localized electron from the ceria electrode to form a unidentate carbonate specie [38, 54]. Upon cathodic polarization, an oxygen ion is transported via oxygen vacancies to the bulk SDC leaving an O-C-O specie (adsorbed CO). The adsorbed CO can desorb as gas, or when a large enough overpotential is applied, it can be further reduced to a C-O, C=O or Ce-CO_2 specie.

Several of these will likely have to be in close proximity to form C-C species after the C-O, C=O or Ce-CO_2 bonds have been broken.

On Ni-YSZ the redox reactions can only occur at the 3PB. Carbides are likely to form by dissolution of carbon atoms into the Ni crystal as suggested in literature [19, 61–64], but no carbides were identified during the analysis. In any case, the carbon must first form at the 3PB or on the Ni, before dissolution can take place. We suggest the following simple reactions (eq. 4.4 and eq. 4.5), which, contrary to what occurs on doped ceria, are strictly electrochemical.

$$CO_{(g)} + 2e'_{Ni} + V_O^{\bullet\bullet} \rightleftharpoons C_s + O_O^x \qquad \text{(eq. 4.4)}$$

$$CO_{2(g)} + 4e'_{Ni} + 2V_O^{\bullet\bullet} \rightleftharpoons C_s + 2O_O^x \qquad \text{(eq. 4.5)}$$

Using the Kröger-Vink notation, where O_O^x, $V_O^{\bullet\bullet}$ and e'_{Ni} denotes a lattice oxygen, an oxygen vacancy, and an electron from Ni, respectively. In Fig. 4.5b the Ni particles from which the CNTs are growing appear to be electrically isolated, i.e. electrochemically inaccessible, but it is possible that the YSZ surface has sufficient electronic conductivity to supply electrons to the reactions. A thin carbon layer growing on YSZ from the 3PB or from Ni, or the aforementioned adventitious carbon layer, could also cause an electronic connection. Carbon formation on oxides such as YSZ has also been shown to be possible even without a Ni catalyst [65]. The suggested reaction scheme for carbon formation on Ni-YSZ is illustrated in Fig. 4.6b. Once the carbon has deposited at the interface, it is likely that dissolution into the Ni crystal follows. When sufficient carbon has diffused into Ni and carbides are formed, carbon precipitates as a CNT growing outwards with a Ni nanoparticle at its tip.

4.5 Conclusions

Electrochemically driven carbon formation has previously been observed to occur during CO_2 electrolysis, but the comprehensive investigation presented here constitutes the first of its kind. By analyzing adsorbates on carefully selected surfaces we are one step closer to understanding the full set of fundamental reaction mechanisms. The results have elucidated the source of the inhibiting effect of ceria, which was previously loosely linked to the high concentration of oxygen vacancies. We have found that carbonates covering the acceptor-doped ceria surface likely

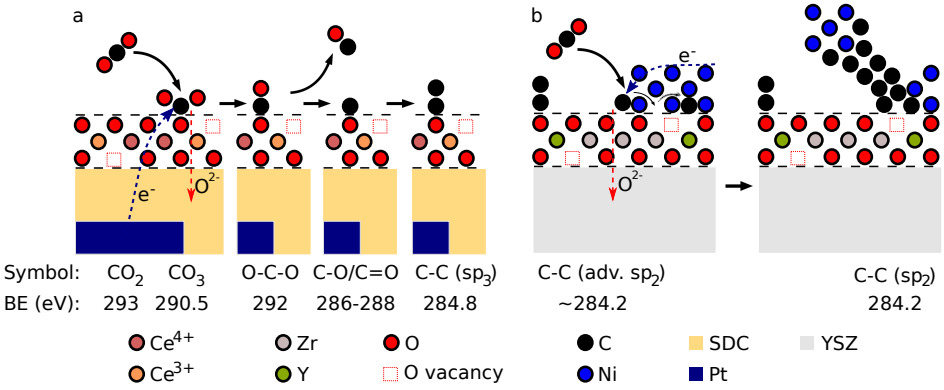

Figure 4.6: Illustrations of proposed reaction mechanisms for carbon formation and coverage on a doped ceria surface and at a Ni-YSZ interface. a, on SDC, CO_2 is adsorbed and forms unidentate carbonate, which under a cathodic potential is reduced to an adsorbed CO specie. The adsorbed CO specie can desorb as gas or be further reduced to a C-O, C=O or Ce-CO_2 specie, which in turn can form C-C species. b, on Ni-YSZ, CO_2 is directly reduced to a surface carbon atom at the 3PB, which then dissolves into the Ni particle. Eventually a CNT grows and pushes the Ni particle off of the YSZ.

are intermediates in the carbon formation and that other oxidized carbon species inhibit the formation of carbon. Lacking similar adsorbates, Ni-YSZ catalyzed carbon growth more readily, i.e. precisely when thermodynamically expected to. Another noteworthy observation was the formation of CNTs on Ni-YSZ, which explains the significantly more severe effect of carbon formation in porous electrodes lacking doped ceria.

The realization that the applied overpotential can cause carbon formation during operation is key for the choice of operation strategy for a hydrocarbon- or CO_2-fueled SOC system. An increase of electrode overpotential caused by other unrelated degradation mechanisms could trigger a sudden formation of carbon [13]. The discoveries presented here advance the fundamental understanding of carbon formation, which is required in the design of more robust SOC electrodes that can operate with hydrocarbons or CO_2 with higher efficiency and longer lifetime. Electrochemical control over CNT growth is another novel finding, which may find application within the field of nanotechnology [66, 67].

4.6 Methods

4.6.1 Sample preparation

The single-chamber model electrochemical cells were fabricated on single-crystal (100) $Y_{0.16}Zr_{0.84}O_{1.92}$ (YSZ) substrates acting as the oxygen-ion-conducting electrolyte with dimensions 10 x 10 x 0.5 mm^3, with one side polished. The fabrication procedure follows in chronological order. The counter-electrode (CE) was applied on the rough side of the substrate by hand-painting Pt paste (Ferro GmbH 6402101-5), which was dried on a hot-plate at 200 °C and sintered at 800 °C for 1 h in stagnant air, forming a porous Pt backbone. Next, an aqueous precursor salt solution for CGO [68] was wet infiltrated, dried at 250 °C on a hot-plate and decomposed at 350 °C for 0.5 h in stagnant air. The CGO was introduced to enhance the oxygen-ion-conducting and electrocatalytic capabilities. The large area and relatively high performance of the CE ensured that the prevalent part of the potential-drop was across the working-electrode (WE), with a minor (<1 %) drop over the electrolyte. The exact overpotential of the CE was not determined, but assumed to be insignificant. The overpotential of the WE was thus estimated as $\eta_{WE} = V_{cell}$ - $I_{cell}R_{\Omega}$, with R_{Ω} found by EIS. On the polished side, the Pt or Ni current conducting pattern was fabricated by metal lift-off photolithography. An undercut resist layer (Dow Microposit LOL 2000) was spin-coated on the polished side of the YSZ substrate at 2000 r.p.m. for 60 s (~300 nm thick) and annealed in air at 180 °C for 5 minutes. To the annealed undercut layer, a positive photoresist (Shipley S-1813) was spin-coated at 4000 r.p.m. for 45 s and baked at 100 °C for 2.5 min underneath a glass cover. The photomask was aligned with a Karl Suss MJB 3 mask aligner and the spin-coated films were exposed to UV light with a dosage of 105 mJ. The photoresist was developed in a Shipley Microposit MF CD-26 Developer solution until the undercut was ~1 μm. After the pattern was rinsed with deionized water, dried, oxygen plasma cleaned for 30 sec at 200 W, the metal was deposited in 3 mbar Ar in a DC magnetron Lesker sputter system. Liftoff was accomplished dissolving the resist in Baker PRS-1000 Positive Photoresist stripper heated to 50 °C. A final oxygen plasma treat at 300 W for 60 s ensured removal of any photolithographic residue. The Pt pattern current collector consisted of 27 x 2000 μm stripes of 180 nm height and 5 μm width separated by 10 μm. A closed loop design improved interconnectivity to prevent disconnected metal stripes due to defects in the photolithography process; 500 x 750 μm^2 Pt contact pads were placed on the side of the patterns for contact with the current collector probe. The Ni pattern consisted of 13 x 2000 μm stripes of 200 nm height and 5 μm width separated by 50 μm. A closed loop design was used again to ensure metal connectivity. A 500 x 750 μm^2 Ni contact pad was placed at one end of the pattern for probe contact. Each YSZ patterned

sample had two WEs so that the biased electrode could be compared to a reference sample exposed to identical experimental conditions but left unbiased. The Pt was annealed at 650 °C for 1 h in 100 mTorr. On the Pt pattern samples, a 650 μm thick $Sm_{0.2}Ce_{0.8}O_{1.9-\delta}$ film was deposited by pulsed-laser deposition (PLD) at 650 °C in 5 mTorr O_2 with a laser fluency of 1.5 J cm^{2-} at 10 Hz with a substrate to target distance of 70 cm. For the Ni-SDC sample, an additional 35 nm thick NiO layer was deposited by PLD on top of the SDC. The NiO layer was reduced to randomly dispersed, approximately 200-400 nm, Ni particles in-situ during the XPS experiment with a 500 mTorr CO:CO_2 (1:1) atmosphere. The Ni-YSZ sample had Ni particles next to the Ni pattern, which varied in size from 40 nm to less than 1 nm.

4.6.2 Electrochemical XPS

Ambient-pressure XPS experiments were conducted at beamline 9.3.2 [69] (Ni-SDC and SDC samples) and beamline 11.0.2 [70] (Ni-YSZ sample) at the Advanced Light Source synchrotron, Lawrence Berkeley National Laboratory. Scienta R4000 HiPP and Specs Phoibos 150 differentially pumped electron analyzers are employed for beamline 9.3.2 and 11.0.2, respectively, which together with a homebuilt sample holder allows for experimental conditions of up to 700 °C [71] and 1 Torr [69], or several Torr for 11.0.2. Ohmic heating was supplied by a ceramic heater. Electrical contact was established by mechanically pressing a Pt coil onto the CE, while the electrical contact to the WE was made by Pt/Ir probes. More details on the design of the sample holder can be found elsewhere [70, 71].

The soft x-ray penetration depth is estimated to ~1 nm for all spectra by applying a similar kinetic energy, 160 – 320 eV. Incident angle was 75 ° for the SDC and Ni-SDC samples at beamline 9.3.2, while it was 65 ° for Ni-YSZ at beamline 11.0.2. The difference causes significantly different gas phase peak intensity between the samples and a slightly different BE, but this did not affect the data analysis significantly. The WE and an Au foil were Fermi coupled with the electron analyzer. The BE of each spectrum was calibrated with the Au $4f_{7/2}$ peak (84.0 eV). A Biologic SP-300 potentiostat was used for chrono-amperometry and EIS. The latter was used to estimate the temperature by comparing the Ohmic resistance, R_Ω, to a calibration done in a tube furnace equipped with a thermocouple.

During the experiments, adventitious carbon was first burned off for the SDC and NiO-SDC samples by flowing O_2. This was not possible for the Ni-YSZ sample, as the metallic Ni pattern would undergo a redox cycle to NiO potentially causing an electrical disconnection of part of the electrode. Therefore, adventitious carbon

was found on the Ni-YSZ sample. In the fitting of the carbon peaks, the assumption was made that the adventitious carbon peak would not change significantly in intensity and that the slope of the BE shifting would remain constant. CO and CO_2 of research grade purity was then carefully dosed and equilibrated to a ~1:1 ratio, which was confirmed by means of the XPS gas phase peaks intensities calibrated for the difference in electron-molecule scattering cross-sections of CO and CO_2 [72], as well as with a mass-spectrometer.

4.7 Supporting Information

4.7.1 Calculations of electrochemical threshold

The carbon formation threshold on account of the Boudouard reaction (eq. 4.1) can be found from thermodynamics:

$$\Delta G_r = \Delta H_r \cdot T\Delta S_r = -RT\ln\left(K_r\right) = -RT\ln\left(\frac{pCO^2}{pCO_2}\right) \qquad \text{(eq. S.4.1)}$$

Where ΔG_r, ΔH_r and ΔS_r are the changes in Gibbs free energy, the enthalpy and the entropy of the reaction, respectively. T is the absolute temperature, R is the gas constant, K_r is the equilibrium constant of the reaction, pCO and pCO_2 is the partial CO and CO_2 pressure. Since we only have CO and CO_2 in the atmosphere; $x_{CO} = 1 - x_{CO_2}$. If we account for pressure, $p = pCO + pCO_2$, we then have:

$$K_x = K_{eq.} \cdot p = \frac{\left(1 - x_{CO_2}\right)^2}{x_{CO_2}} \qquad \text{(eq. S.4.2)}$$

Where x represent a mole fraction. The binomial solution to two equations with two unknowns can now be found:

$$x_{CO_2} = \left(\frac{1/2}{p \cdot K_{eq.}} + 1\right) - \sqrt{\left(\frac{1/2}{p \cdot K_{eq.}} + 1\right)^2 - 1} \qquad \text{(eq. S.4.3)}$$

$K_{eq.}$ is dependent on temperature, T, and can be found using the FactSage thermochemical software and database [73].

The reactant gas atmosphere for the threshold can then be converted to a partial oxygen pressure, $p\mathrm{O}_2(Boud.)$, with the unit atm:

$$pO_2(Boud.) = 10^{2\cdot\log_{10}(K_{eq.})} \cdot \left(\frac{x_{CO_2}}{x_{CO}}\right)^2 \qquad \text{(eq. S.4.4)}$$

In the same manner, the pO_2 of the actual inlet reactant gas atmosphere, $pO_2(reac.)$, can be calculated. Here, the equilibrium constant for the CO_2-electrolysis reaction; $CO_2 \rightleftharpoons CO + \frac{1}{2}O_2$, must be used. Since we now know the pO_2 of the inlet gas, we can use the Nernst equation to calculate the OCV:

$$OCV = \frac{RT}{nF} \ln\left(\frac{pO_2(air)}{pO_2(reac.)}\right) \quad \text{(eq. S.4.5)}$$

Where n is the number of electrons participating in the reaction, F is Faraday's constant, and $pO_2(air)$ is the partial oxygen pressure of air (0.21 atm). The unit will be V.

In a similar manner, the potential of the threshold can be calculated, and by subtraction we find the electrochemical overpotential of the cell required for carbon formation:

$$\eta(Boud.) = OCV - \frac{RT}{nF} \ln\left(\frac{pO_2(air)}{pO_2(Boud.)}\right) \quad \text{(eq. S.4.6)}$$

Which will be negative (cathodic) given the experimental conditions chosen in this study. The relative contribution of the WE, the CE and the electrolyte was further elaborated on in sec. 4.6.1.

4.7.2 Photoemission spectra fitting and peak assignment

For all three samples the fitting routine was consistent, albeit with minor differences. The fitting software was CasaXPS v2.3.17PR1.1. All peaks were fitted with a Gaussian-Lorentzian shape, "GL(30)", except for sp_2 type carbon, which was fitted with an asymmetric peak consisting of a blend of a Doniach-Sunjic function and a Gaussian-Lorentzian function, "DS(0.03,125)GL(30)". A singularity index of 0.03 was found to fit the data well, a value smaller than what others have reported using, i.e. 0.1-0.2 [45, 74]. For SDC and Ni-SDC a Shirley background was fitted and subtracted, while for Ni-YSZ a linear background was deemed more suitable for the data. Changing the background type did not alter the results of the analysis, only the fitting error bars. Before and after each experimental condition, a spectrum for each relevant photon energy was collected on an Au foil a few mm from the sample, which was Fermi coupled (grounded) to the working electrode. Thus, all spectra were calibrated to Au $4f_{7/2}$ (84.0 eV). The photon

energy was chosen such that the kinetic energy yielded an information depth of ~0.6 nm for all spectra (kinetic energy ~250 eV ±100 eV). The BE mentioned in the following refer to OCV, since the BE will shift with applied potential for some species.

C 1s. Despite the reduction in possible species due to the lack of H-, N- and F-atoms, there are still a significant amount of possible surface species to identify within a narrow BE window. In order of descending BE, the assigned peaks can be seen in Tab. 4.1. In addition to these, an unidentified peak was often visible 1 eV higher than CO_2 (gas). The CO_3 and C=O peaks were not present on the Ni-YSZ electrode, and C-O only to a small degree. At the beginning of the test at OCV, adventitious C-C sp_2 was only present on Ni-YSZ. After carbon deposition, C-C sp_2 appeared to a minor degree on SDC and Ni-SDC, but the primary C-C type on these samples was sp_3.

O 1s. The assigned peaks can be seen in Tab. 4.2. The C adsorbate peak could be either CO_3, C=O, O-C=O, C-O-C or C-O-C=O, but this peak was only present for the SDC and Ni-SDC samples, not the Ni-YSZ. This is consistent with the lack of CO_3, C=O and to a certain extent, C-O, on Ni-YSZ in the C 1s spectra. Other surface species, e.g. S 2p, Zr 3d, Ce 4d, Ni 2p and 3p are of lower importance in the present study. These are simply fitted with sufficient peaks to accurately determine the BE shifting of the main peak while varying the potential (Fig. 4.4 and Fig. S.4.4).

4.7.3 Current-potential curves

The current response during the chrono-amperometry experiments for the three samples is shown in Fig. S.4.2. The SDC sample in Fig. S.4.2a has a relatively low performance before applying a large cathodic potential of -600 mV. The activation is clearly visible by comparing the current at +200 mV anodic potential before and after the large cathodic bias. This sort of activation was expected to occur when the ceria surface was reduced sufficiently to cause crack-formation along the Pt-patterns. The formation of such cracks are confirmed by SEM after the experiment. This phenomenon is expected to significantly increase the surface area, which is not accounted for in the geometric area-normalized current density shown here. More interestingly, a large increase in resistance of the cell is observed at the most reducing conditions. This is most likely due to coverage of the SDC surface by carbon, effectively blocking the 2PB, supported by an observed decrease in the lattice oxygen peak from O 1s.

For the Ni-SDC sample, Fig. S.4.2b, more current-potential points were collected. Like SDC, the resistance increased at the most reducing condition. This was

followed by activation upon returning to the most oxidizing condition. The increased resistance at the reducing condition clearly shows hysteresis in the iV-curve. Such hysteresis is also observed for full-sized commercial SOECs during chrono-potentiometry experiments with carbon formation [12]. After oxidizing most of the carbon and returning to the reducing condition, the electrochemical performance is regained. We also applied negative bias to this electrode again and the same resistance increase was observed as the carbon grew back again.

Curiously, the formation of carbon did not cause an increase in resistance for the Ni-YSZ sample. The coverage of reaction sites by carbon might be compensated by electronically connecting more Ni particles as carbon is growing. This would increase the 3PB length and the performance.

The shape of the iV curves of the SDC samples (Fig. S.4.2a-b) are as expected based on comparison to other model electrode tests [38, 75]. However, a reversed cathodic shape of the iV-curve for the Ni-YSZ sample was expected [75]. This might be due to the effect suggested above where carbon deposition extended the 3PB length, improving the electrode performance.

4.7.4 Figures for supporting information

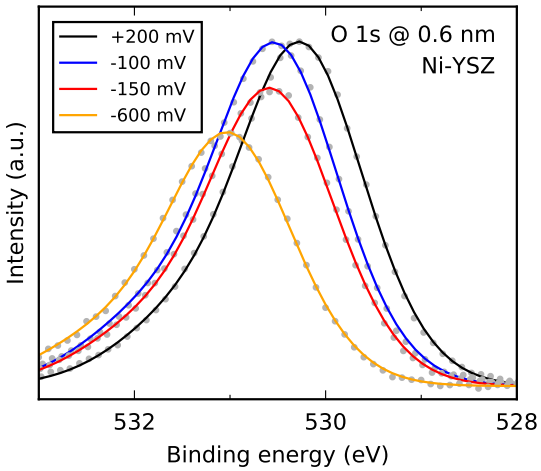

Figure S.4.1: Lattice oxygen (1s) XPS peak decreasing in intensity as carbon is deposited on the Ni-YSZ model electrode. The decrease in intensity indicates coverage of the YSZ surface. The shift in BE is due to the applied potential.

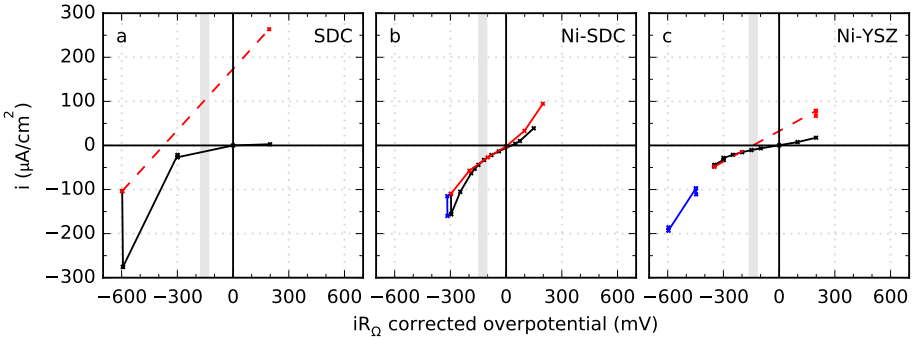

Figure S.4.2: iV plots with hysteresis for the three samples. a, SDC, b, Ni-SDC and c, Ni-YSZ. The fixed potential was corrected for the Ohmic resistance of the YSZ electrolyte. The arrows indicate the chronological order in which measurements were recorded, with black first, red second and blue third. The thermodynamic threshold for carbon formation is shown by the gray box, accounting for experimental uncertainties and differences.

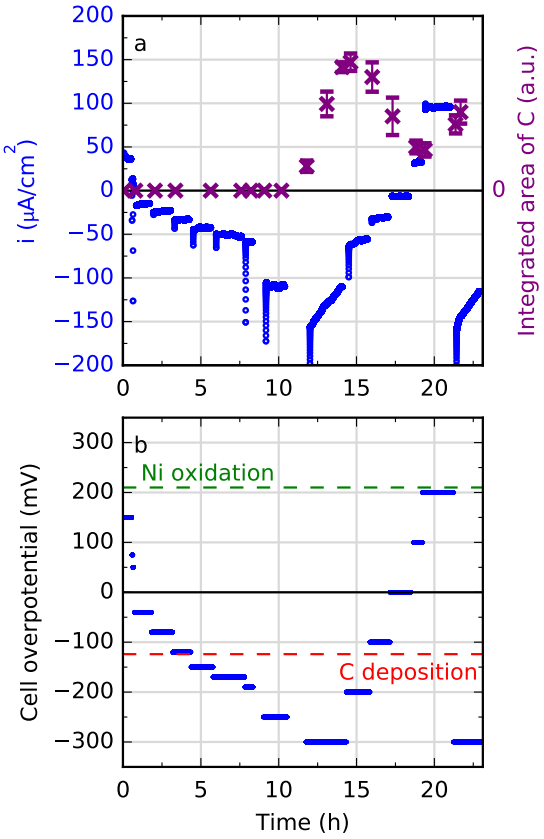

Figure S.4.3: The response of the current and carbon coverage to the changing potential throughout the Ni-SDC experiment. The SDC and Ni-YSZ electrodes have similar, but not identical behavior. a, current density and the integrated area of the C peak changing with time. b, the applied voltage changing with time. The upper limit of Ni oxidation is also plotted (–), and the carbon deposition threshold (–) which was intentionally crossed. After 12 h, when -300 mV is applied, the current drops considerably and carbon coverage increases. When decreasing the potential below the thermodynamic threshold for carbon formation, the carbon coverage decreases and the current stabilizes. The results were reproduced at the end of the experiment by applying -300 mV again.

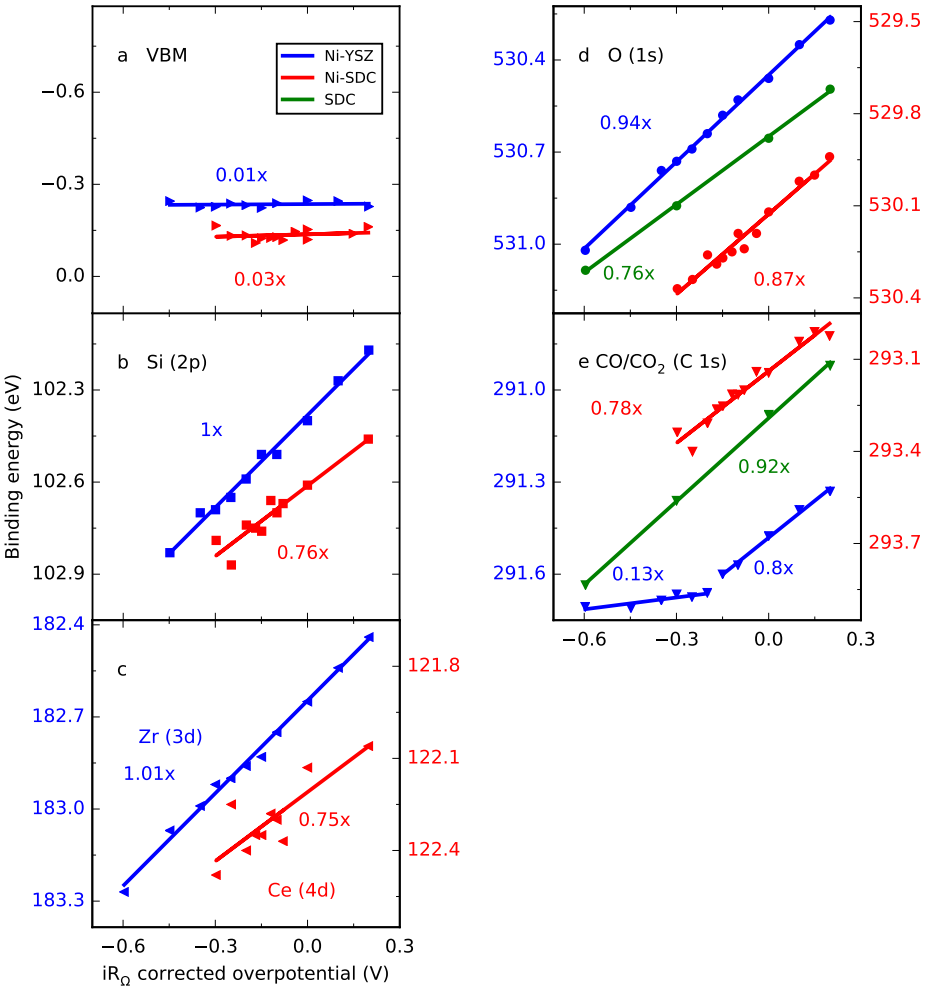

Figure S.4.4: Shifts of XPS core-level peaks for different surface species. a, Valence band maximum (VBM) dominated by Ni. b, Si 2p. c, Zr 3d for Ni-YSZ and Ce 4d for Ni-SDC. d, lattice oxygen. e, CO_2 gas phase for SDC and Ni-SDC, and CO gas phase for Ni-YSZ. In e, the changing slope observed for Ni-YSZ was confirmed by the shifts of gas phase core-level peaks from the O 1s spectrum.

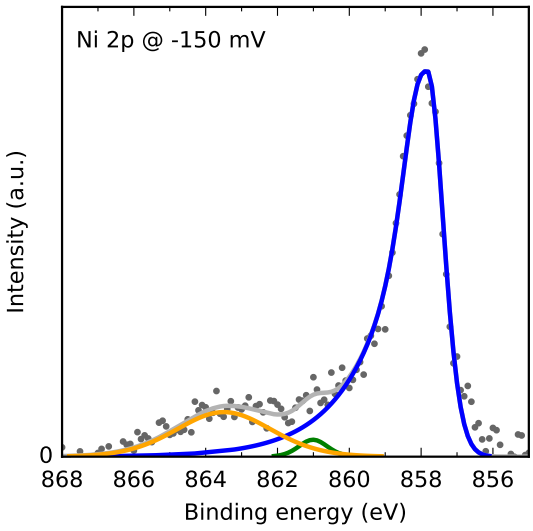

Figure S.4.5: Ni 2p NAPXPS spectrum measured at -150 mV on the Ni-YSZ electrode. Note: For this spectrum, calibration to Au has not been done, so the BE is not correct.

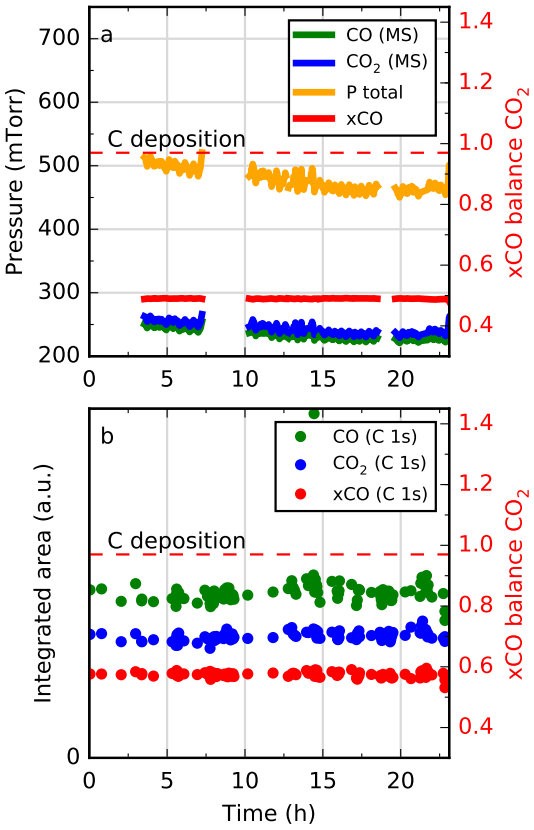

Figure S.4.6: Pressure and gas composition throughout the Ni-SDC experiment measured using mass-spectroscopy and the XPS C 1s spectra. a, total pressure (—), CO pressure (—) and CO_2 pressure (—) on the first y-axis in mTorr, and the CO:CO_2-ratio (—) and the carbon deposition threshold (–) on the second y-axis. The data has been smoothed slightly to remove excessive noise in pressure measurements while moving the sample stage. b, integrated area of the CO (—) and CO_2 peaks (—) from C 1s after calibrating for the difference in electron-molecule scattering cross-sections ($1.449 \cdot 10^{-20}$ m^2 and $2.177 \cdot 10^{-20}$ m^2 at 490 eV, respectively) on the first y-axis, and the CO:CO_2-ratio (—) and the carbon deposition threshold (–) on the second y-axis. The CO:CO_2-ratio agrees fairly well, although the result from XPS is about 7-8% xCO higher.

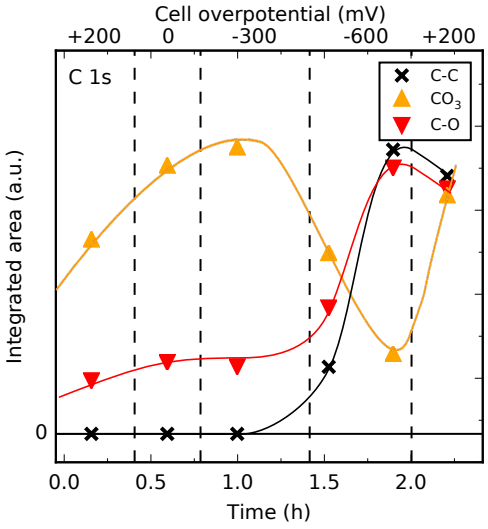

Figure S.4.7: Integrated area of carbon, carbonate and C-O from NAPXPS peaks measured on the SDC electrode throughout the experiment. As carbon starts depositing at -600 mV, the carbonate coverage drops. Likewise, when carbon starts oxidizing at +200 mV at the end of the experiment, the carbonate coverage increases again. The C-O coverage follows the C-C coverage.

4.7.5 Tables for supporting information

Table 4.1: Peak assignment for C 1s at OCV.

Specie	Approx. BE (eV)	BE constraints (eV)	FWHM (eV)	FWHM constraints (eV)	Ref.
CO_2 (gas)	293.0-293.3	293.0-294.5	0.6	<1.1	[38, 54, 76]
CO (gas)	291.5-291.9	290.0-293.0	0.6	= FWHM(CO_2)	[77]
CO_3	290.4-290.6		1.4-1.55	<1.55	[38, 50, 51, 54, 56, 76]
C=O	288.0-288.4	287.0-289.0	1.4-1.55	= FWHM (CO_3)	[40, 47, 49–51]
C-O	286.4-286.6	=BE (CO) – 5.3	1.4-1.55	= FWHM (CO_3)	[40, 47, 49–51]
C-C sp_3	284.7-285.0	284.7-285.1	0.7	<2.0	[42–47, 78]
C-C sp_2 (adv.)	284.3*	284.0-286.0*	1.5	<2.0	[42–47]
C-C sp_2	284.3	283.9-284.5	1.0-1.2	<2.0	[42–47, 78]

*Before electrochemical carbon deposition. After deposition, the BE was strictly constrained to continue the linear BE shift with applied potential as observed prior to deposition (see Fig. 4.4b).

Table 4.2: Peak assignment for O 1s at OCV.

Specie	Approx. BE (eV)	BE constraints (eV)	FWHM (eV)	FWHM constraints (eV)	Ref.
CO (gas)	538.1		1.0	= FWHM (CO_2)	[77]
CO_2 (gas)	536.9		1.0		[38, 54, 76]
C adsorbates	532.5-532.7		1.5	= FWHM (Lattice O)	[38, 54, 76, 78]
Si impurities	531.3-531.5		1.5	= FWHM (Lattice O)	[37, 38]
Lattice O	529.9-530.1		1.5		[37, 38, 54, 76]

4.8 References

1. Marbán, G. & Valdés-Solís, T. Towards the hydrogen economy? *International Journal of Hydrogen Energy* **32,** 1625–1637 (Aug. 2007).
2. Graves, C., Ebbesen, S. D., Mogensen, M. & Lackner, K. S. Sustainable hydrocarbon fuels by recycling CO_2 and H_2O with renewable or nuclear energy. *Renewable and Sustainable Energy Reviews* **15,** 1–23 (Jan. 2011).
3. Dlugokencky, E. & Tans, P. *Recent Global CO_2 from NOAA/ESRL.* 2016.
4. Lackner, K. S. Capture of carbon dioxide from ambient air. *European Physical Journal: Special Topics* **176,** 93–106 (2009).
5. Hartvigsen, J., Elangovan, S. E., Elwell, J., Larsen, D. & Clark, L. Development of solid oxide electrolysis for oxygen production from mars atmosphere carbon dioxide. *EFCF 2016 proceedings,* A1403 (2016).
6. Meyen, F. E., Hecht, M. H. & Hoffman, J. A. Thermodynamic model of Mars Oxygen ISRU Experiment (MOXIE). *Acta Astronautica* **129,** 82–87 (Dec. 2016).
7. Skafte, T. L., Hjelm, J., Blennow, P. & Graves, C. Quantitative review of degradation and lifetime of solid oxide cells and stacks. *EFCF 2016 proceedings,* B0501 (2016).
8. Tøttrup, P. B. Kinetics of decomposition of carbon monoxide on a supported nickel catalyst. *Journal of Catalysis* **42,** 29–36 (1976).
9. Tavares, M., Alstrup, I., Bernardo, C. & Rostrup-Nielsen, J. Carbon Formation and CO Methanation on Silica-Supported Nickel and Nickel-Copper Catalysts in CO + H_2 Mixtures. *Journal of Catalysis* **158,** 402–410 (Feb. 1996).
10. Tao, Y., Ebbesen, S. & Mogensen, M. Degradation of solid oxide cells during co-electrolysis of H_2O and CO_2: Carbon deposition under high current densities. *ECS Transactions* **50,** 139–151 (2013).
11. Tao, Y., Ebbesen, S. D., Zhang, W. & Mogensen, M. B. Carbon Nanotube Growth on Nanozirconia under Strong Cathodic Polarization in Steam and Carbon Dioxide. *ChemCatChem* **4000** (Feb. 2014).
12. Skafte, T. L., Graves, C., Blennow, P. & Hjelm, J. Carbon Deposition during CO_2 Electrolysis in Ni-Based Solid-Oxide-Cell Electrodes. *ECS Transactions* **68,** 3429–3437 (2015).
13. Skafte, T. L., Graves, C., Blennow, P. & Hjelm, J. Carbon deposition and sulfur poisoning during CO_2 electrolysis in Ni-based solid-oxide-cell electrodes. *In manuscript* (2017).

14. Rostrup-Nielsen, J. R. & Alstrup, I. Innovation and science in the process industry: steam reforming and hydrogenolysis. *Catalysis today* **53,** 311–316 (1999).

15. Bengaard, H. S. *et al.* Steam Reforming and Graphite Formation on Ni Catalysts. *Journal of Catalysis* **209,** 365–384 (2002).

16. Mortensen, P. M. & Dybkjær, I. Industrial Scale Experience on Steam Reforming of CO_2-Rich Gas. *Applied Catalysis A: General* **495,** 141–151 (2015).

17. Liu, C.-j., Ye, J., Jiang, J. & Pan, Y. Progresses in the Preparation of Coke Resistant Ni-based Catalyst for Steam and CO_2 Reforming of Methane. *ChemCatChem* **3,** 529–541 (Mar. 2011).

18. Kim, T. *et al.* A study of carbon formation and prevention in hydrocarbon-fueled SOFC. *Journal of Power Sources* **155,** 231–238 (Apr. 2006).

19. Lee, W. Y., Hanna, J. & Ghoniem, a. F. On the Predictions of Carbon Deposition on the Nickel Anode of a SOFC and Its Impact on Open-Circuit Conditions. *Journal of the Electrochemical Society* **160,** F94–F105 (Dec. 2012).

20. Subotić, V. *et al.* Anode regeneration following carbon depositions in an industrial-sized anode supported solid oxide fuel cell operating on synthetic diesel reformate. *Journal of Power Sources* **295,** 55–66 (2015).

21. Tao, Y., Ebbesen, S. D. & Mogensen, M. B. Carbon Deposition in Solid Oxide Cells during Co-Electrolysis of H_2O and CO_2. *Journal of the Electrochemical Society* **161,** F337–F343 (Jan. 2014).

22. Duboviks, V. *et al.* A Raman spectroscopic study of the carbon deposition mechanism on Ni/CGO electrodes during CO/CO_2 electrolysis. *Physical Chemistry Chemical Physics* **16,** 13063 (2014).

23. Duboviks, V. *et al.* Carbon deposition behaviour in metal-infiltrated gadolinia doped ceria electrodes for simulated biogas upgrading in solid oxide electrolysis cells. *Journal of Power Sources* **293,** 912–921 (2015).

24. Yu, Y. *et al.* Carbon Deposits and Pt/YSZ Overpotentials in CO/CO_2 Solid Oxide Electrochemical Cells. *ECS Transactions* **57,** 3119–3126 (2013).

25. Kirtley, J. D., Halat, D. M., McIntyre, M. D., Eigenbrodt, B. C. & Walker, R. A. High-Temperature Spectrochronopotentiometry: Correlating Electrochemical Performance with In Situ Raman Spectroscopy in Solid Oxide Fuel Cells. *Analytical Chemistry* **84,** 9745–9753 (Nov. 2012).

26. Li, W., Shi, Y., Luo, Y., Wang, Y. & Cai, N. Carbon deposition on patterned nickel / yttria stabilized zirconia electrodes for solid oxide fuel cell / solid oxide electrolysis cell modes. *Journal of Power Sources* **276,** 26–31 (2015).

27. Maher, R. C. *et al.* Raman Spectroscopy of Solid Oxide Fuel Cells: Technique Overview and Application to Carbon Deposition Analysis. *Fuel Cells* **13,** 455–469 (Aug. 2013).

28. Li, X. *et al.* An operando surface enhanced Raman spectroscopy (SERS) study of carbon deposition on SOFC anodes. *Phys. Chem. Chem. Phys.* **17,** 21112–21119 (2015).

29. Choi, Y., Brown, E. C., Haile, S. M. & Jung, W. Electrochemically modified, robust solid oxide fuel cell anode for direct-hydrocarbon utilization. *Nano Energy* **23,** 161–171 (2016).

30. Duboviks, V. *et al.* A Raman spectroscopic study of the carbon deposition mechanism on Ni/CGO electrodes during CO/CO_2 electrolysis. *Physical Chemistry Chemical Physics* **16,** 13063 (2014).

31. Lee, J. G. *et al.* Durable and High-Performance Direct-Methane Fuel Cells with Coke-Tolerant Ceria-Coated Ni Catalysts at Reduced Temperatures. *Electrochimica Acta* **191,** 677–686 (2016).

32. Skafte, T. L., Sudireddy, B. R., Blennow, P. & Graves, C. Carbon and Redox Tolerant Infiltrated Oxide Fuel-Electrodes for Solid Oxide Cells. *ECS Transactions* **72,** 201–214 (May 2016).

33. Traulsen, M. L. *et al.* Need for In Operando Characterization of Electrochemical Interface Features. *ECS Transactions* **66,** 3–20 (2015).

34. Liu, Y. *et al.* Mechanism of CO Disproportionation on Reduced Ceria. *ChemCatChem* **2,** 336–341 (Mar. 2010).

35. Feng, Z. A. *et al.* Origin of Overpotential-Dependent Surface Dipole at CeO_{2-x}/Gas Interface During Electrochemical Oxygen Insertion Reactions. *Chemistry of Materials* **28,** 6233–6242 (Sept. 2016).

36. Gopal, C. B., Gabaly, F. E., Mcdaniel, A. H. & Chueh, W. C. Origin and Tunability of Unusually Large Surface Capacitance in Doped Cerium Oxide Studied by Ambient-Pressure X-Ray Photoelectron Spectroscopy. *Advanced Materials* **28,** 4692–4697 (2016).

37. Feng, Z. a., El Gabaly, F., Ye, X., Shen, Z.-X. & Chueh, W. C. Fast vacancy-mediated oxygen ion incorporation across the ceria-gas electrochemical interface. *Nature Communications* **5,** 1–9 (2014).

38. Feng, Z. a., Machala, M. L. & Chueh, W. C. Surface electrochemistry of CO_2 reduction and CO oxidation on Sm-doped CeO_{2-x}: coupling between Ce^{3+} and carbonate adsorbates. *Phys. Chem. Chem. Phys.* **17,** 12273–12281 (2015).

39. Robertson, J. Diamond-like amorphous carbon. *Materials Science and Engineering: R: Reports* **37,** 129–281 (May 2002).

40. Ming, H. *et al.* Large scale electrochemical synthesis of high quality carbon nanodots and their photocatalytic property. *Dalton Transactions* **41,** 9526 (2012).

41. Georgakilas, V., Perman, J. A., Tucek, J. & Zboril, R. Broad Family of Carbon Nanoallotropes: Classification, Chemistry, and Applications of Fullerenes, Carbon Dots, Nanotubes, Graphene, Nanodiamonds, and Combined Superstructures. *Chemical Reviews* **115,** 4744–4822 (2015).

42. Morar, J. F. *et al.* C 1s excitation studies of diamond (111). I. Surface core levels. *Physical Review B* **33,** 1346–1349 (Jan. 1986).

43. Chen, C. T. & Sette, F. High Resolution Soft X-Ray Spectroscopies with the Dragon Beamline. *Physica Scripta* **T31,** 119–126 (1990).

44. Mizokawa, Y. The C KLL first-derivative x-ray photoelectron spectroscopy spectra as a fingerprint of the carbon state and the characterization of diamondlike carbon films. *Journal of Vacuum Science & Technology A: Vacuum, Surfaces, and Films* **5,** 2809 (Sept. 1987).

45. Haerle, R., Riedo, E., Pasquarello, A. & Baldereschi, A. sp_2/sp_3 hybridization ratio in amorphous car. *Physical Review B* **65,** 045101 (Dec. 2001).

46. Brühwiler, P. A. *et al.* π^* and σ^* Excitons in C 1s Absorption of Graphite. *Physical Review Letters* **74,** 614–617 (Jan. 1995).

47. Ermolieff, a. *et al.* XPS, Raman spectroscopy, X-ray diffraction, specular X-ray reflectivity, transmission electron microscopy and elastic recoil detection analysis of emissive carbon film characterization. *Surface and Interface Analysis* **31,** 185–190 (2001).

48. Doniach, S. & Sunjic, M. Many-electron singularity in X-ray photoemission and X-ray line spectra from metals. *Journal of Physics C: Solid State Physics* **3,** 285–291 (1970).

49. Czekaj, I. *et al.* Characterization of surface processes at the Ni-based catalyst during the methanation of biomass-derived synthesis gas: X-ray photoelectron spectroscopy (XPS). *Applied Catalysis A: General* **329,** 68–78 (Oct. 2007).

50. Mudiyanselage, K. *et al.* Importance of the metal-oxide interface in catalysis: In situ studies of the water-gas shift reaction by ambient-pressure X-ray photoelectron spectroscopy. *Angewandte Chemie - International Edition* **52,** 5101–5105 (2013).

51. Staudt, T. *et al.* Electronic Structure of Magnesia-Ceria Model Catalysts, CO_2 Adsorption, and CO_2 Activation: A Synchrotron Radiation Photoelectron Spectroscopy Study. *The Journal of Physical Chemistry C* **115,** 8716–8724 (May 2011).

52. Helveg, S. *et al.* Atomic-scale imaging of carbon nanofibre growth. *Nature* **427,** 426–429 (Jan. 2004).

53. Hofmann, S. *et al.* In situ observations of catalyst dynamics during surface-bound carbon nanotube nucleation. *Nano Letters* **7,** 602–608 (2007).

54. Yu, Y. *et al.* CO_2 activation and carbonate intermediates: an operando AP-XPS study of CO_2 electrolysis reactions on solid oxide electrochemical cells. *Phys. Chem. Chem. Phys.* **16,** 11633–11639 (2014).

55. Cheng, Z., Sherman, B. J. & Lo, C. S. Carbon dioxide activation and dissociation on ceria (110): A density functional theory study. *Journal of Chemical Physics* **138,** 1–20 (2013).

56. Senanayake, S. D. *et al.* Probing the reaction intermediates for the water-gas shift over inverse CeO_x/Au(111) catalysts. *Journal of Catalysis* **271,** 392–400 (May 2010).

57. Kwak, J. S. *et al.* Nanoparticle Embedded p-Type Electrodes for GaN-Based Flip-Chip Light Emitting Diodes. *Journal of Nanoscience and Nanotechnology* **6,** 3547–3550 (Nov. 2006).

58. Wiltner, A. & Linsmeier, C. Formation of endothermic carbides on iron and nickel. *physica status solidi (a)* **201,** 881–887 (Apr. 2004).

59. El Gabaly, F., McCarty, K. F., Bluhm, H. & McDaniel, A. H. Oxidation stages of Ni electrodes in solid oxide fuel cell environments. *Physical Chemistry Chemical Physics* **15,** 8334 (2013).

60. Li, X. *et al.* In Situ Probing of the Mechanisms of Coking Resistance on Catalyst-Modified Anodes for Solid Oxide Fuel Cells. *Chemistry of Materials* **27,** 822–828 (2015).

61. Guo, J. *et al.* Improving the Carbon Resistance of Ni-Based Steam Reforming Catalyst by Alloying with Rh: A Computational Study Coupled with Reforming Experiments and EXAFS Characterization. *ACS Catalysis* **1,** 574–582 (June 2011).

62. Nikolla, E., Schwank, J. & Linic, S. Hydrocarbon steam reforming on Ni alloys at solid oxide fuel cell operating conditions. *Catalysis Today* **136,** 243–248 (July 2008).

63. Boldrin, P. *et al.* Strategies for Carbon and Sulfur Tolerant Solid Oxide Fuel Cell Materials, Incorporating Lessons from Heterogeneous Catalysis. *Chemical Reviews* **116,** 13633–13684 (Nov. 2016).

64. Toebes, M. Impact of the structure and reactivity of nickel particles on the catalytic growth of carbon nanofibers. *Catalysis Today* **76,** 33–42 (Nov. 2002).

65. Kogler, M. *et al.* High-Temperature Carbon Deposition on Oxide Surfaces by CO Disproportionation. *The Journal of Physical Chemistry C* **120,** 1795–1807 (Jan. 2016).

66. Jong, K. D. & Geus, J. Carbon nanofibers: catalytic synthesis and applications. *Catal. Rev. Sci. Eng.* **42,** 481–510 (2000).

67. Baughman, R. H. Carbon Nanotubes–the Route Toward Applications. *Science* **297,** 787–792 (Aug. 2002).

68. Graves, C., Martinez, L. & Sudireddy, B. R. High Performance Nano-Ceria Electrodes for Solid Oxide Cells. *ECS Transactions* **72,** 183–192 (May 2016).

69. Grass, M. E. *et al.* New ambient pressure photoemission endstation at advanced light source beamline 9.3.2. *Review of Scientific Instruments* **81** (2010).

70. Frank Ogletree, D., Bluhm, H., Hebenstreit, E. D. & Salmeron, M. Photoelectron spectroscopy under ambient pressure and temperature conditions. *Nuclear Instruments and Methods in Physics Research Section A: Accelerators, Spectrometers, Detectors and Associated Equipment* **601,** 151–160 (Mar. 2009).

71. Whaley, J. a. *et al.* Note: Fixture for characterizing electrochemical devices in-operando in traditional vacuum systems. *Review of Scientific Instruments* **81,** 1–3 (2010).

72. Hwang, W., Kim, Y.-K. & Rudd, M. E. New model for electron-impact ionization cross sections of molecules. *The Journal of Chemical Physics* **104,** 2956 (1996).

73. Bale, C. *et al.* FactSage thermochemical software and databases - recent developments. *CALPHAD* **33,** 295–311 (June 2009).

74. Díaz, J., Paolicelli, G., Ferrer, S. & Comin, F. Separation of the sp_3 and sp_2 in the C1s photoemission spectra of amorphous carbon film. *Physical Review B* **54,** 8064–8069 (Sept. 1996).

75. Graves, C., Chatzichristodoulou, C. & Mogensen, M. Kinetics of CO/CO_2 and H_2/H_2O reactions at Ni-based and ceria-based solid-oxide-cell electrodes. *Faraday Discuss.* 1–21 (2015).

76. Deng, X. *et al.* Surface Chemistry of Cu in the Presence of CO_2 and H_2O. *Langmuir* **24,** 9474–9478 (Sept. 2008).

77. Norton, P. R. & Tapping, R. Photoelectron spectroscopy studies of the adsorption of CO and CO_2 on nickel, platinum and copper. *Chemical Physics Letters* **38,** 207–212 (1976).

78. Blume, R. *et al.* The influence of intercalated oxygen on the properties of graphene on polycrystalline Cu under various environmental conditions. *Physical chemistry chemical physics : PCCP* **16,** 25989–6003 (2014).

5 Mitigating degradation

Despite the unsuccessful attempts at mitigating carbon formation using infiltration of nanoparticles into Ni-YSZ electrodes in chapter 3, there are still some intriguing benefits of the technique. Higher performance is commonly observed and although it appears not to be the case in the specific operation mode of CO_2-electrolysis, higher robustness towards carbon formation and impurities have been reported. However, the agglomeration of the infiltrated nanoparticles and thus the long-term stability is consistently a concern. In this last part of the dissertation we will investigate a novel approach by performing the infiltration after the cell has degraded. We will examine three case-studies of otherwise unintentional incidents which will damage the cell, one of which is carbon formation. Lastly, we will apply this concept to stack level to learn about the potential for scalability and widespread employment to accelerate the technology towards commercialization.

The following pages are based on the 4^{th} publication: Eliminating fuel electrode degradation and reactivating solid oxide cells and stacks.

5.1 Abstract

The SOC could play a vital role in energy storage when the share of intermittent electricity production is high. However, large-scale commercialization of the technology is still hindered by the limited lifetime. Here, we address this issue by examining the potential for repairing various failure and degradation mechanisms occurring in the fuel electrode, thereby extending the potential lifetime of a SOC system. We successfully infiltrated the Ni-YSZ electrode in commercial cells with CGO after operation. By this method we fully reactivated the fuel electrode after simulated reactant starvation, carbon formation and thousands of hours of steady degradation. The potential for entirely eliminating the degradation of the fuel electrode was demonstrated by infiltrating after microstructural stabilization of the electrode had occurred. Moreover, we showed the scalability of the concept by reactivating an 8-cell stack based on a commercial design.

5.2 Introduction

The SOC is a promising device for the conversion of intermittently produced electricity into storable chemical energy [1]. The technology still faces challenges regarding lifetime [2] and capital cost before a large-scale commercialization can take place. Taking advantage of economies of scale requires targeting niche markets initially, such as reduction of CO_2 to CO or biogas upgrading [3]. However, to mitigate degradation and failure mechanisms and thereby increase lifetime, significant efforts in materials and surface science is still required.

The concept of infiltrating nano-sized particles to increase surface area or supply electronic or ionic conductivity to the electrodes was initially considered immensely promising on account of the high performance reported [4]. Infiltration of the oxygen electrode, especially, has been intensely studied [5–7]. Efforts are being made to develop alternative fuel electrode structures also or modifying the classical Ni-YSZ electrode [7–9]. Some success has been obtained, especially in terms of increased robustness (carbon formation tolerance, redox tolerance, poisoning tolerance), but the concept has not been embraced by SOC producers. The Ni-YSZ electrode is still cost-effective compared to alternative lab-scale electrodes and is currently employed by largely every commercial SOC producer [2]. For the Ni-YSZ electrode, the process is somewhat complicated by the requirement of NiO reduction to allow room for the infiltrated material. Even so, it would be beneficial in paving the way for a commercial breakthrough to enhance the performance or robustness of this well-known cermet, ideally without altering the already well-established fabrication process.

Lately, the interest in infiltrating SOCs has declined. According to the Scopus literature database, the year 2016 was the first with an appreciable drop in the number of published articles in this specific field[1]. One concern raised consistently is whether the improved performance has a lasting effect, and only few [10] have studied the performance of infiltrated cells over the course of the required thousands of hours. Another concern is whether the technique is scalable to stack-level. Infiltration on stack level has been achieved before by infiltrating individual non-Ni-YSZ electrodes before assembly [10]. In the collaboration between Topsoe Fuel Cell A/S and DTU Energy, a Ni-YSZ-based stack was recently infiltrated after assembly [11]. The beneficial effect was most noticeable after infiltration of the oxygen electrode, and that of the Ni-YSZ electrode was negligible. However, except for these recent cases, the typical approach is still to apply the solution with a pipette, in many cases onto a mm^2-sized symmetric cell.

Here we have infiltrated commercially sized Ni-YSZ electrodes on both cell and

[1] Search conducted February 6^{th}, 2017; "solid oxide" + infiltration

stack level, after assembly. Furthermore, we have applied the concept of infiltration in an unconventional manner, namely to mitigate various failure and degradation mechanisms after they have occurred. This contrasts to the typical objective of enhancing the beginning-of-life performance. In the following we thus investigate the concept of reactivating the fuel electrode after detrimental damage such as reactant starvation and carbon formation. Furthermore, we examine the same effect on long-term, steady degradation. Lastly, we explore the possibility of reactivating a severely damaged commercial stack after thousands of hours of operation. We perform the majority of the testing in harsh CO/CO_2 gas atmospheres, relevant for the aforementioned niche application.

5.3 Experimental

Nominally identical planar cells from the same production batch manufactured by Haldor Topsoe A/S were tested as reference cells. These had NiO-YSZ as support and fuel electrode, a ~10 μm YSZ electrolyte and an oxygen electrode of LSCF and CGO. They further had a CGO barrier layer between the electrolyte and the oxygen electrode and contact layers on both electrodes. All cells were laser-cut to 5.3x5.3 cm^2 with a 16 cm^2 active area. Cells were mounted in either a FuelCon or DTU Energy in-house designed single-cell test rig at DTU Risø campus. A corrugated Ni and Au mesh were used for electronic current collection and fuel distribution on the fuel and oxygen side, respectively. A Au foil frame was used as a sealing gasket on the fuel side. The test-house design is described in more detail in Njodzefon [12]. The cell was heated to 850 °C while flowing N_2, followed by a reduction process of 2 h of 9% H_2/N_2 and 1.5 h of 5% H_2O/H_2.

Reactivated or infiltrated cells refer to reference cells which have been coated by a CGO solution on the fuel electrode side. Stoichiometric amounts of Ce- and Gd-nitrate salts were mixed with water and a surfactant (Triton X-100) to obtain the desired $Ce_{0.8}Gd_{0.2}O_{2-\delta}$-phase. A Cu infiltration solution was made in the same manner. Since the NiO-YSZ fuel electrode must be reduced prior to infiltration, reference cells were reduced as described above and cooled to room-temperature in 9% H_2/N_2. The cells were then carefully removed from the ceramic test house. After infiltration, the material was decomposed in stagnant air at 350 °C for 0.5 h. Ni oxidation is a risk while heating the already reduced Ni-YSZ electrode in air, but only minor bending of the cells was observed and as will be shown, the performance did not suffer from this treatment. After the heat-treatment, a brittle layer of CGO was left on the surface which was carefully dusted off and the surface was cleaned with ethanol. Such an infiltration and heating process constitutes one infiltration cycle, and is hereon labeled “1xCGO”. By measuring the weight gain

and knowing the exact dimensions, the approximate volume that the infiltrated material occupies can be estimated. 1xCGO typically yielded 2 vol-%, and the Ni-YSZ electrode have previously been shown to have a post-reduction porosity of ~30 vol-%. A few cells underwent more cycles obtaining a higher loading, or with other materials. For instance, a cell infiltrated with one cycle of CGO and 5 cycles of a Cu solution is here labeled as "1xCGO+5xCu". Lastly, the infiltrated cells could be remounted in the test rig and heated to operating temperature in 9% H_2/N_2.

EIS was measured using a Solartron 1252A or 1260 and a measurement resistor. The data was corrected with a short-circuit response of the test setup and stray inductance was subtracted using the Kramers–Kronig procedure. The frequency range was typically 0.1 Hz to 1 MHz. All analysis was performed using the RavDav software package [13].

LV-SEM on a Zeiss Supra 35 FE-SEM was used to analyze the loss of Ni percolation in long-term tested cells, as described in Thydén et al. [14].

An 8-cell stack produced by Haldor Topsoe A/S was operated for ~3kh in electrolysis mode with 95% CO_2 as reactant gas and either 5% CO or H_2 to avoid Ni oxidation. The Topsoe Stack Platform (TSP-1) is a state-of-the-art commercial stack design capable of holding up to 75 cells of approximately 110 cm^2 active area [15]. Here, a TSP-1 was loaded with 8 full-sized cells and wires for voltage measurements were attached to the interconnects between the cells, allowing for iV and EIS measurements on individual repeating units (RU, a cell and an interconnect). Voltage and EIS was measured on individual RUs throughout the test. The RU voltages can be seen in Fig. S.5.1. After testing the stack was then infiltrated with one cycle of CGO by "flushing" the manifold compartments. The solution was then pumped out and air pockets were removed by placing the stack in a vacuum enclosure. The stack was calcined at 350 °C for 1 h with a small flow of air, similar to how the solution was calcined for the single cells. A microstructural analysis of the infiltrated material using this technique can be found in Kiebach et al. [11].

5.4 Results

5.4.1 Initial performance

The improvement in performance of infiltrated cells relative to the reference was investigated by means of EIS in Fig. 5.1a-b and quantified in Fig. 5.1c-d. Two infiltrated cells are considered here; 1xCGO and 1xCGO+5xCu. Cu was infiltrated in separate cycles and was chosen as an alternative to Ni with higher

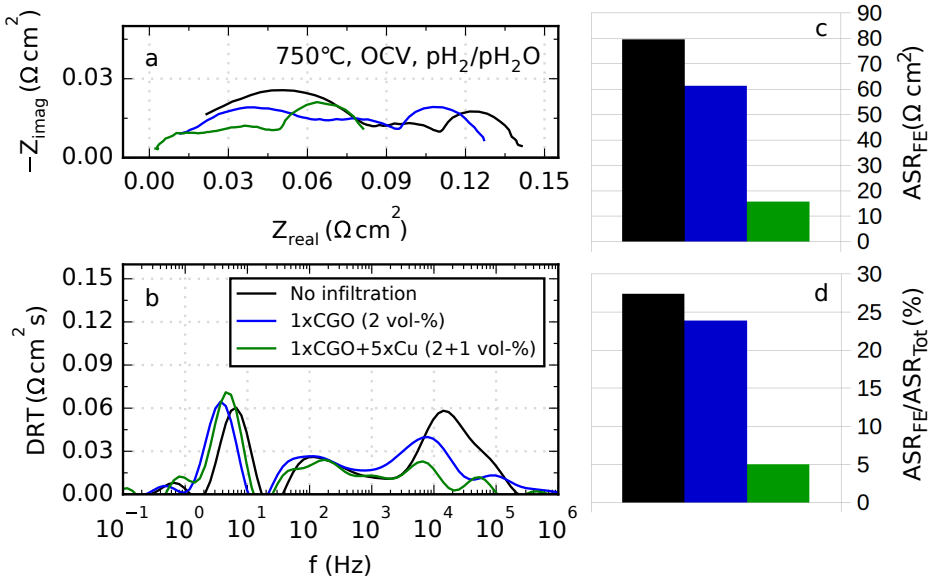

Figure 5.1: Reducing polarization resistance of the fuel electrode by infiltrating CGO or a combination of CGO and Cu. Performance at 750 °C in pH_2/pH_2O 0.5/0.5 and OCV. a, Nyquist spectra with the Ohmic resistance estimated by model fitting and subtracted. b, DRT spectra showing the impedance contribution of the fuel electrode above 1 kHz for the three different cells. c, Quantified contribution of the fuel electrode after model fitting. d, The contribution of the fuel electrodes relative to the total ASR.

carbon formation tolerance reported [16]. The contributions of different components were modelled using 1-D two-channel transmission line models for the two porous electrodes, and 2-D coupled plug-flow models for the combined gas diffusion and conversion for each electrode [17] (Fig. S.5.4). This advanced model will quantify the impedance accurately and physically meaningful parameters can be extracted, but this is beyond the scope of this investigation. It is more time-consuming than the conventional RQ-based fitting models, which will also be used in the remaining part of this study. With the Ohmic resistance fitted and subtracted, the improvement in total polarization resistance is clearly visible in Fig. 5.1a. Higher resolution in the frequency/time-domain can be obtained by converting the impedance data to the DRT format, as seen in Fig. 5.1b. The impedance contribution above 1 kHz is ascribed to the fuel electrode electrochemistry (see Fig. S.5.3b), and it is clearly seen that the improvement of the

total polarization resistance is entirely caused by changes in the fuel electrode. The total ASR contribution of the fuel electrode decreased by a factor of 5 from 80 mΩ cm^2 to 16 mΩ cm^2 for the 1xCGO+5xCu cell (Fig. 5.1c). The relative contribution compared to the total resistance of the cell decreased from 27% to 5% (Fig. 5.1d).

5.4.2 Repairing

Three different examples of repairing damages to the fuel electrode are examined in the following. The first two examples simulate cases where a human or system error causes severely damaging operating conditions, albeit only for a brief amount of time. The third example is a more general case, where constant operating conditions causes mild, constant degradation. Lastly, the concept is demonstrated to work on a larger scale by going from single cell level to an 8-cell stack.

5.4.3 Case 1, reactant starvation

Reactant starvation causes significant, and in some cases fatal, damage to an operating cell. In the case of electrolysis operation, if oxygen ions are not available in the fuel (H_2O or CO_2), the fuel electrode material will be reduced. For Ni-YSZ, the oxygen ions in the zirconia lattice will be forced though the electrolyte to the positive electrode leaving zirconium [18]. This was simulated here by operating the cell with an electrolysis current density of -2 A/cm^2 for 1 h with 100% H_2. The cell voltage quickly reached 1.9 V where it stabilized (Fig. S.5.5), suggesting this to be the potential required for zirconia reduction [18]. The damage to the cell is evident from the voltage by comparing the reference cell to the cell starved of reactants (Fig. 5.2). However, if a cell exposed to the same treatment is infiltrated by one cycle of CGO, the voltage does not increase as much.

From Fig. 5.3a it is seen that the Ohmic resistance does not change, but the total polarization resistance is clearly affected by the reactant starvation simulation. It is clearly seen from the DRT spectrum (Fig. 5.3b) that only the fuel electrode is damaged. The low frequency peak (0.1 – 1 Hz), which also increases, is mainly ascribed to gas conversion in the fuel electrode (see Supporting Information). By fitting the impedance collected throughout the experiments with a simple L-R-RQ-RQ-RQ-RQ-RQ model (Fig. S.5.6), the contribution of the fuel electrode can be quantified and the result is shown in Fig. 5.2 on the 2^{nd} y-axis. R_{FE} agrees well with the observed changes of cell voltage, except for the repaired cell. The resistance of the fuel electrode is almost as low as for the reference cell, and the electrode can thus be largely considered restored to the condition it was in prior

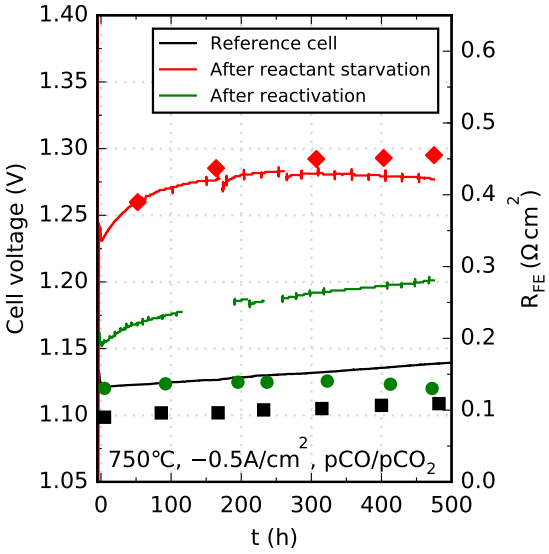

Figure 5.2: Repairing a fuel electrode which has been starved of reactants. One reference cell, one cell starved of reactants and exposed to an operating voltage of 1.9 V for 1 h, and a cell exposed to the same treatment, but repaired with infiltration. The performance and degradation was compared at 750 °C in pCO/pCO_2 0.34/0.66 (inlet) with -0.5 A/cm^2 electrolysis current density. Cell voltage (lines, 1^{st} y-axis) and fuel electrode resistance (symbols, 2^{nd} y-axis). Missing voltage measurements for the repaired cell was due to a temporary loss of data collection.

to the damaging effect occurred. The difference in cell voltage, however, means that some other part of the cell degraded, and the impedance of the oxygen electrode was indeed observed to increase (Fig. 5.3b, frequency range 10-100 Hz). The cause of this was not identified and is not the focus here, but it is noted that the observation could not be reproduced and is therefore deemed coincidental.

5.4.4 Case 2, coking

Another example of a fatal failure mechanism is carbon formation in the Ni-YSZ electrode. Since Ni is an excellent catalyst for carbon formation, this can occur when operating on hydrocarbons or CO/CO_2. Here, the case was simulated by applying a sufficiently high electrolysis current density, which will cause the local

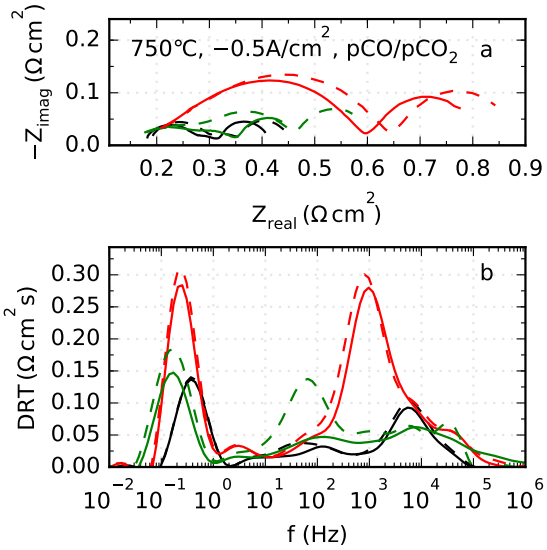

Figure 5.3: Repairing a fuel electrode which has been starved of reactants. a, Nyquist plot of impedance in pCO/pCO_2 0.5/0.5 before (solid lines) and after (dashed lines) the 500 h test. b, DRT plot showing the difference in impedance contribution of the fuel electrode above ~1 kHz and the increased contribution of the oxygen electrode for the repaired cell at a frequency of ~500 Hz. See Fig. 5.2 for legends.

$CO:CO_2$-ratio at the electrode/electrolyte interface to cross the thermodynamic threshold. Run-away carbon formation will quickly delaminate the electrode from the electrolyte during electrolysis operation [19–22] which will rapidly destroy the electrode. However, by carefully monitoring the voltage and current density the amount of carbon, and thus the damage caused, can be controlled [21, 22]. This case thus simulates a system where the gas or current (in the case of SOFC-mode) supply momentarily fails, causing a small amount of carbon to form inside the electrode. The damage caused is illustrated in the EIS spectrum in Fig. 5.4. Once again, it is clearly seen that the damage is confined to the fuel electrode in the frequency range above 1 kHz (Fig. 5.4b). By infiltrating the cell after carbon formation, however, the damage can be fully repaired. In fact, the total polarization resistance is almost exactly identical to that before carbon deposition (Fig. 5.4a).

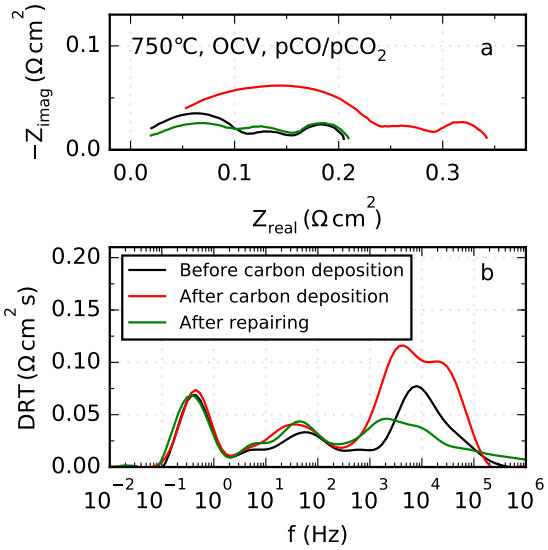

Figure 5.4: Repairing minor deposition of carbon in the fuel electrode. Performance of the same cell at 750 °C in pCO/pCO2 0.5/0.5 and OCV before and after carbon deposition, and after carbon deposition and repairing. a, Nyquist plot with the Ohmic resistance fitted and subtracted. b, DRT plot showing the changing contribution of the fuel electrode above 1 kHz.

5.4.5 Case 3, degradation

In the third example we do not consider any specific degradation or failure mechanisms. Instead, we let the cell run under constant conditions and degrade steadily. This will cause degradation of presumably all components in the cell, so we do not expect a full recovery when repairing only the fuel electrode. A reference cell was operated for ~2.3 kh in CO/CO_2 with a steady degradation rate of ~37 mV/kh or ~91 mΩ cm^2/kh (total ASR). Another cell was operated for approximately 0.9 kh with a similar degradation rate of ~36 mV/kh or ~80 mΩ cm^2/kh (disregarding the jump at t = 700 h caused by 72 h in H_2/H_2O at OCV and operating temperature). The cell was then infiltrated and ran for another ~1.3 kh. The degradation rate dropped by a factor 3 to ~11 mV/kh or ~26 mΩ cm^2/kh (Fig. 5.5). However, what is even more interesting, when fitting and quantifying the contribution from the fuel electrode, it is seen that the degradation of this component has been essentially eliminated. Furthermore, the resistance of the repaired fuel electrode after 2.3 kh is almost identical to the beginning of the test, ~80 mΩ cm^2. This

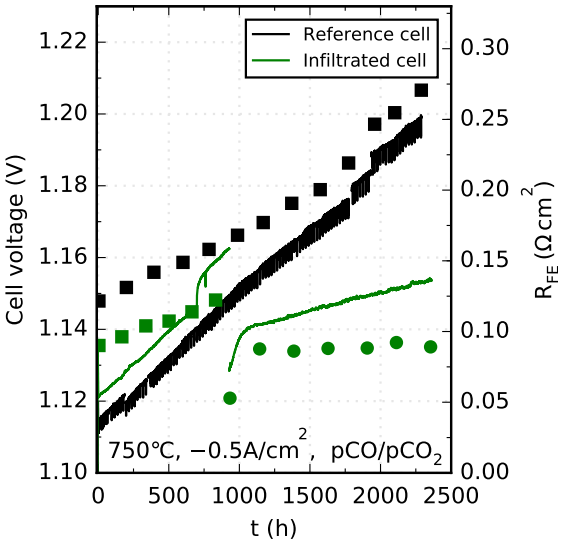

Figure 5.5: Repairing and eliminating fuel electrode degradation over the course of 2.3 kh. The performance and degradation was compared at 750 °C in pCO/pCO_2 0.34/0.66 (inlet) with -0.5 A/cm^2 electrolysis current density. Cell voltage (lines, 1^{st} y-axis) and fuel electrode resistance (symbols, 2^{nd} y-axis).

can also be seen from the Nyquist and DRT spectra in Fig. 5.6. The component responsible for the majority of the degradation rate is now the oxygen electrode (Fig. 5.6b, ~30 Hz). The peak frequency of the infiltrated electrode has shifted to significantly lower frequency (from ~5 kHz to ~250 Hz) and starts overlapping with the oxygen electrode peak (~25 Hz). This makes it difficult to distinguish between the two in the Nyquist plot, but they can still be separated in the DRT plot and thus in the fitting of the data. The Ohmic resistance did not change significantly during the tests. This agreed with the relatively small loss of Ni percolation after testing (Fig. S.5.7), which will otherwise result in an additional porous electrolyte layer. Under these conditions, the degradation is thus not due to loss of Ni percolation as is the case in demanding steam electrolysis operation with poor Ni-YSZ microstructure [23].

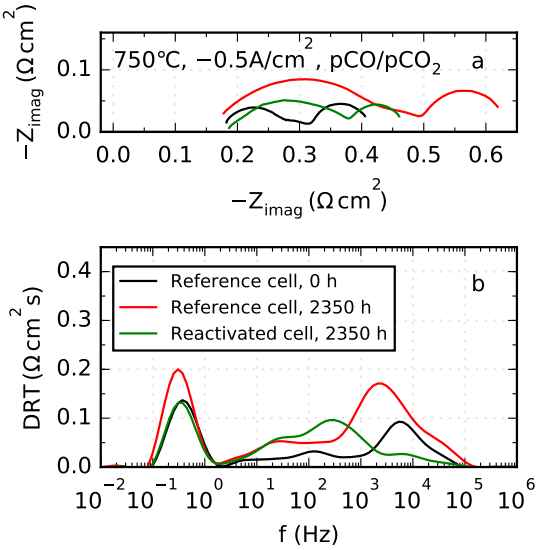

Figure 5.6: Repairing and eliminating fuel electrode degradation over the course of 2.3 kh. a, Nyquist spectra measured at the beginning and end of the test for the reference cell, and at the end of the test of the repaired cell. b, DRT plot showing the difference in impedance contribution of the fuel electrode. The fuel electrode peak frequency is shifted to lower frequency for the repaired cell, ~250 Hz. The degradation of the oxygen electrode is also seen for both cells, at ~100 Hz for the beginning of the reference test and shifted to ~25 Hz for the two spectra at the end of the tests.

5.4.6 Stack level tests

To illustrate the applicability of the concept to the technology in general, the method was scaled up to stack level. The lifetime of the stack is not the focus here and will be published elsewhere, but a brief description follows. The RUs degraded steadily and the average cell voltage had increased with ~100 mV during the test, except for the first three RUs. Some of the suspected main degradation mechanisms were sulfur poisoning by contaminants in the CO gas and minor carbon formation. Furthermore, a number of significant events causing interruptions in the test occurred and these may affect the degradation as well, i.e. pollution of the air to the oxygen electrode with oil, power supply failure, CO_2 gas supply failure and carbon formation in the surrounding tubing.

After the long-term test, the stack was infiltrated with one cycle of CGO. Voltages obtained in SOFC mode (+0.2 A/cm^2) with H_2/N_2 were either fully restored or even higher than when the test was started (Fig. 5.7). The voltages of the most degraded cells improved the most, and the voltage spread decreased significantly (Fig. S.5.8).

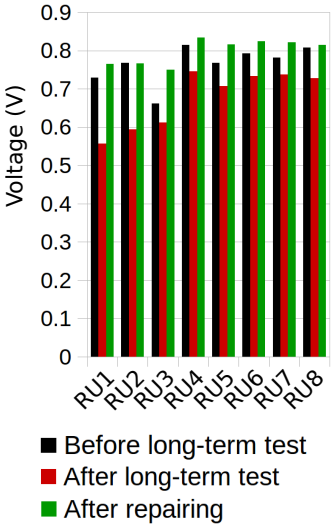

Figure 5.7: Regaining voltage by reactivating a SOC stack. Individual voltage measurements for each RU at 700 °C with pH_2/pN_2 0.6/0.4 and 0.2 A/cm^2 (SOFC-mode) before and after a ~3 kh stack test, and after repairing the stack by means of infiltration.

5.5 Discussion

The initial performance gain of infiltration is commonly reported. We confirmed this observation as we were able to reduce the resistance of the fuel electrode fivefold. Next, we turned our attention to another concept. The ability to repair the cells after near-death incidents, as shown here in the first two examples, could prove to be a useful tool when operating a complex system with many more components than just the SOC stack. The supply of gases or the current supply could be unintentionally interrupted for various reasons, but if the disruption is of short duration on the timescale of minutes or a few hours, we have shown here that the cells are capable of recovering from the damaging effects that can

occur, such as reactant starvation or carbon formation. It is likely that any damage that causes minor delamination between the Ni and YSZ particles can be recovered from by this method (Fig. 5.8). Furthermore, by infiltrating a MIEC with electrocatalytic properties, such as CGO, the reaction zone can be extended. Thus, not only is the delamination repaired, the electrode also gains a larger electrocatalytically active reaction zone. In agreement with others, we have also shown that the performance gain can be further improved by optimizing choice and volume of the infiltrated material.

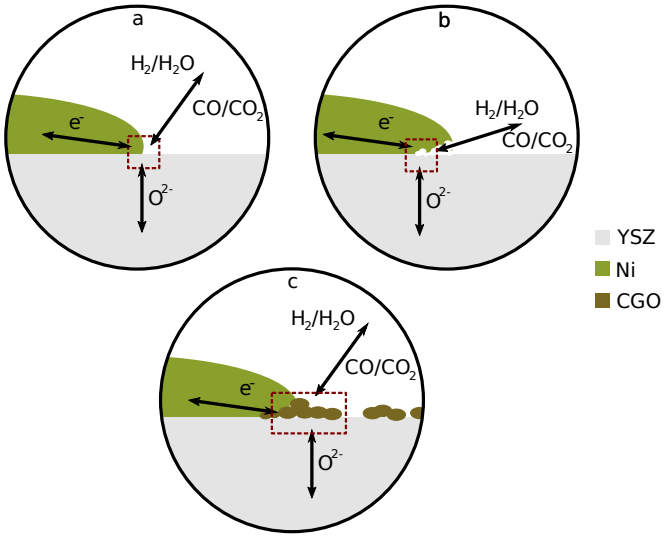

Figure 5.8: Illustration of one suggested degradation mechanism and how infiltration repairs the damage. a, electrons supplied by the Ni particle, oxygen ions supplied by the YSZ particle and gas meets in the reaction zone at the 3PB. b, as local delamination takes place, the reaction zone moves and the 3PB shrinks. For particles with poor connection, complete delamination can occur. c, after infiltration, the delamination is filled by CGO particles and the 3PB (now technically a 2PB since CGO is a MIEC) increases again.

A valid concern often raised regarding SOC electrode infiltration is the longevity of the effect. As have been shown by others (see references in [7]), the infiltrated material tends to agglomerate with time and the performance gain is invalidated. Here we show that, under the conditions used here, the effect may indeed last over the course of several thousand hours, at least when the electrode is infiltrated after stabilization of the microstructure has taken place. Recent results from colleagues at DTU Energy indicate that the effect may even be long-lasting when infiltrating

prior to testing, but we will leave the discussion of this subject for when more related data is available. In the experiment we performed, the performance of the fuel electrode was completely stabilized after infiltration and the contribution of this component was largely unchanged compared to the beginning of the test. Over the course of 2.3kh, the degradation of the fuel electrode was thus eliminated. The preliminary results presented here certainly warrants further investigation.

The second valid concern against infiltration is whether the technique is scalable. Here we take the first step towards proving the scalability by infiltrating an 8-cell stack based on a commercial full-sized stack design. We believe that by combining many decades of experience from infiltration in the field of heterogeneous catalysis and a stack infiltration technique such as that developed by DTU and Haldor Topsoe A/S [11], it is possible to cost-effectively infiltrate full-sized stacks. Here, the concept of repairing the fuel electrode was shown to be transferable from cell to stack level. The individual cell performance based on voltage measurements was regained after ~3 kh of testing with various degradation mechanisms and many unintended systemic failures. Much remains to be investigated, however, and this experiment merely establishes the validity of the method on stack-level. Higher control of the specific degradation mechanisms must be obtained to gain more knowledge of the effect, the repaired stack should be further tested after infiltration, and naturally the method should be scaled up to full-sized commercial stack- or even system-level.

5.6 Conclusions

In the present study we have demonstrated a novel concept of repairing lifetime limiting mechanisms in SOCs. Three case-studies were considered as proof-of-concept on commercial cells. Damages incurred by simulated reactant starvation and carbon formation were fully repaired and the performance of the electrode was entirely restored. The effect was shown to be lasting for 500 h and we have no reason to believe that this would change with additional test time. The third case-study was to examine the effect on generic steady-state degradation. By allowing the microstructure to first stabilize, the degradation of the infiltrated electrode was shown to be completely eliminated over the course of 2.3 kh. Lastly, the method was scaled up to stack level, which similarly revealed positive effects.

Much still remains to be investigated and, as we also demonstrated here, with only minor optimization the performance gain can be even greater. The basic procedure established here demonstrate renewed potential for SOC electrode infiltration and the possibility of optimizing the traditional Ni-YSZ cermet.

5.7 Supporting Information

5.7.1 Electrochemical impedance spectroscopy

An analysis of impedance contributions from different processes occurring in the SOCs was carried out. Changes in gas composition on both the fuel and the oxygen side, and incremental changes in temperature, was used to distinguish between gas concentration and electrochemical processes. Gas concentration processes are only affected by changes of the gas composition and not the temperature [24], while electrochemical processes are affected by both type of changes. A DRT plot can be helpful in increasing the resolution in the time/frequency domain, and thereby more easily differentiate between processes. The difference between two DRT plots (ΔDRT) can be used to identify impedance changes at specific frequency ranges [17].

Gas concentration related processes for the fuel electrode are identified in Fig. S.5.2, where the gas on the fuel side is changed between 50% and 20% H_2O in H_2. As seen, peaks at approximately 1-3 Hz, 20-50 Hz and 100-3000 Hz are identified as being affected by fuel gas concentration changes. Similarly, when changing the gas concentration on the oxygen side between 100% and 21% O_2 in N_2, peaks arise at approximately 1-3 Hz and 20-50 Hz.

With five different characteristic peaks identified, two for the oxygen electrode and three for the fuel electrode, the next step is to investigate whether these are affected by temperature changes. Such an analysis has been carried out and is shown in Fig. S.5.3. The electrochemical processes are thus identified at 100-3000 Hz and 20-50 Hz for the fuel electrode (Fig. S.5.3b) and the oxygen electrode (Fig. S.5.3c), respectively. Combining this analysis with others from literature, we can in Fig. S.5.2b label the 1-3 Hz peak for the fuel electrode as fuel gas conversion (FC), the 20-50 Hz peak for the fuel electrode as fuel gas diffusion (FD), the 100-3000 Hz peak for the fuel electrode as fuel electrode polarization (FP), the 1-3 Hz peak for the oxygen electrode as oxidant gas diffusion (OD), and the 20-50 Hz peak for the oxygen electrode as oxygen electrode polarization (OP).

With the individual processes identified, the impedance response can be quantified using a complex non-linear least squares fitting routine. Either with a more advanced model (Fig. S.5.4) or a simpler one (Fig. S.5.6). The more advanced model is based on a transmission line model for the electrochemical processes occurring at either electrode [17, 25], and a plug-flow gas model for the combined contribution of gas diffusion and conversion [17, 26].

5.7.2 Figures for supporting information

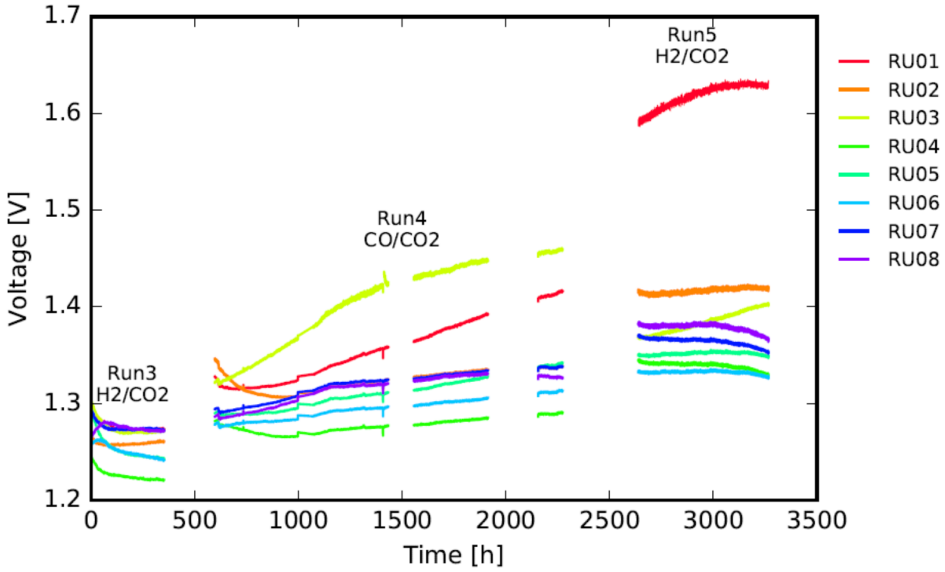

Figure S.5.1: Voltage measurements for each of the eight RUs during CO_2 electrolysis prior to infiltration. The stack was operated at 770 °C with 95% CO_2 and either 5% H_2 or CO. Stack current was -50 A and the fuel utilization was 30 %.

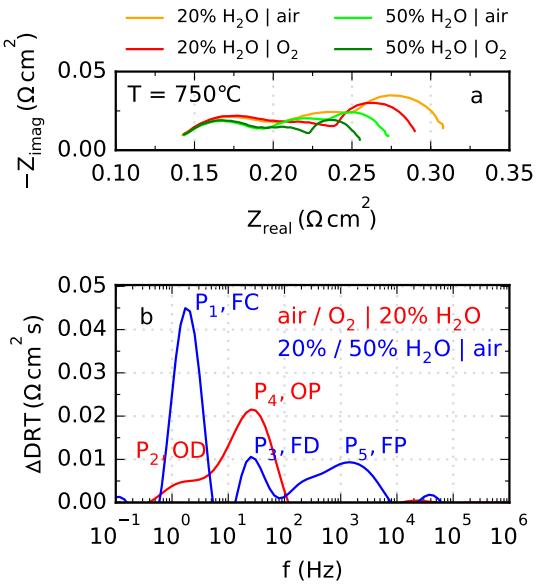

Figure S.5.2: EIS analysis of four different gas compositions at 750 °C , 20% or 50% H_2O in H_2 on the fuel side, and 100% or 21% O_2 in N_2 on the oxygen side, and with a fuel flow rate of 25 mL/min/cm^2, and an oxidant flow rate of 312.5 mL/min/cm^2. a) Nyquist plots, and b) ΔDRT curves illustrating the difference in the DRT upon changing either the gas atmosphere on the fuel side or on the oxygen side, while keeping the gas atmosphere constant on the other side. Peaks identify processes affected by gas composition changes on the two electrode sides.

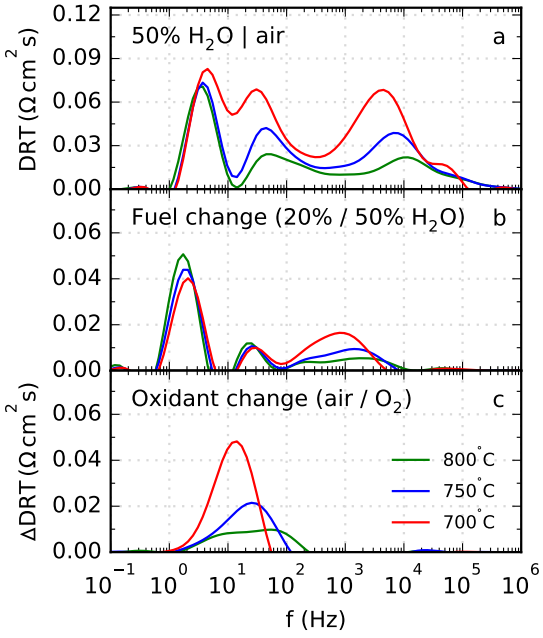

Figure S.5.3: DRT and ΔDRT curves obtained from impedance spectra recorded at 50 °C increments in the temperature interval 700 – 800 °C, and with a fuel flow rate of 25 mL/min/cm^2, and an oxidant flow rate of 312.5 mL/min/cm^2. a) DRT curves calculated from impedance spectra collected with a fuel composition of 50% H_2 + 50% H_2O, with air as the oxidant. b) ΔDRT curves illustrating the difference in the DRT between two different gas compositions, 50% and 20% H_2O in H_2, on the fuel side. c) Delta-DRT curves between two different gas compositions, 100% and 21% O_2 in N_2, on the oxygen side.

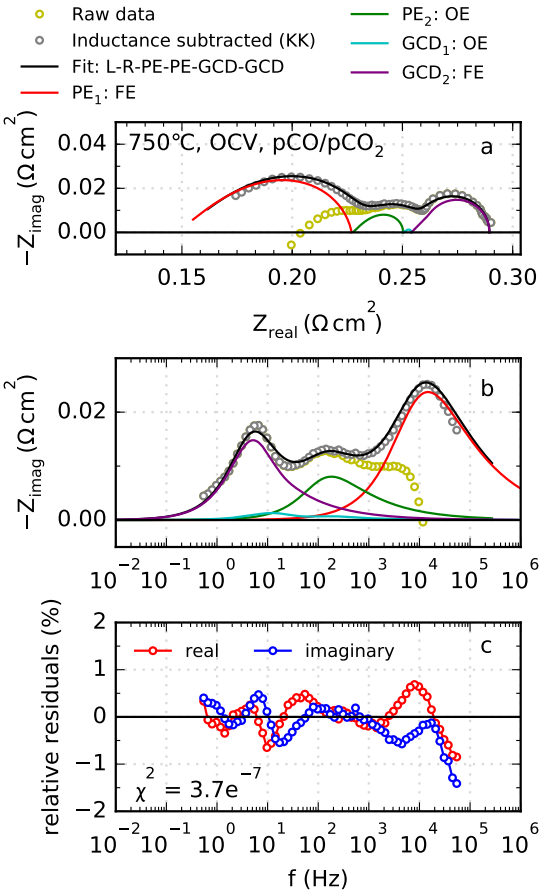

Figure S.5.4: An advanced EIS fitting of data from a test at 750 °C, at OCV with a pCO/pCO_2-atmosphere of 0.5/0.5 and 25 mL/min/cm^2 gas flow to the fuel electrode and 312.5 mL/min/cm^2 air flow to the oxygen electrode. a) Nyquist plot, b) Bode plot, and c) relative residuals between the Kramers-Kronig inductance corrected data and the model fit for the real and imaginary impedance. PE: porous electrode, GCD: gas conversion and diffusion, FE: fuel electrode, and OE: oxygen electrode.

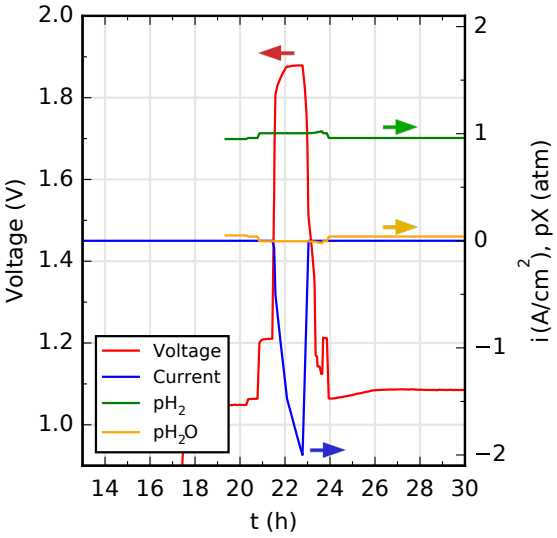

Figure S.5.5: Voltage (red, 1st y-axis), current density (blue, 2nd y-axis), pH2 (green, 2nd y-axis), and pH_2O (orange, 2nd y-axis) for a simulated reactant starvation test at 750 °C.

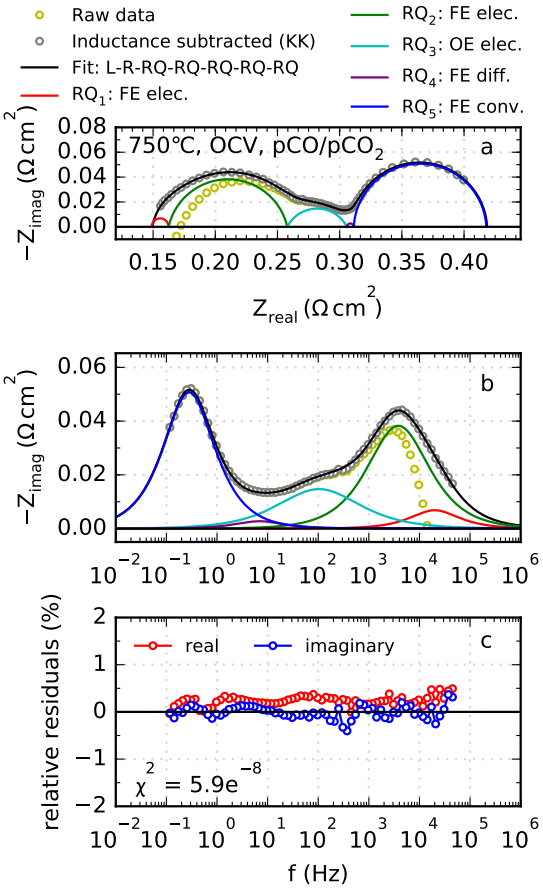

Figure S.5.6: A relatively simple EIS fitting of data from a test at 750 °C, at OCV with a pCO/pCO_2-atmosphere of 0.5/0.5 and 25 mL/min/cm^2 gas flow to the fuel electrode and 312.5 mL/min/cm^2 air flow to the oxygen electrode. a) Nyquist plot, b) Bode plot, and c) relative residuals between the Kramers-Kronig inductance corrected data and the model fit for the real and imaginary impedance. FE: fuel electrode, OE: oxygen electrode, elec.: electrochemistry, diff.: diffusion, and conv.: conversion.

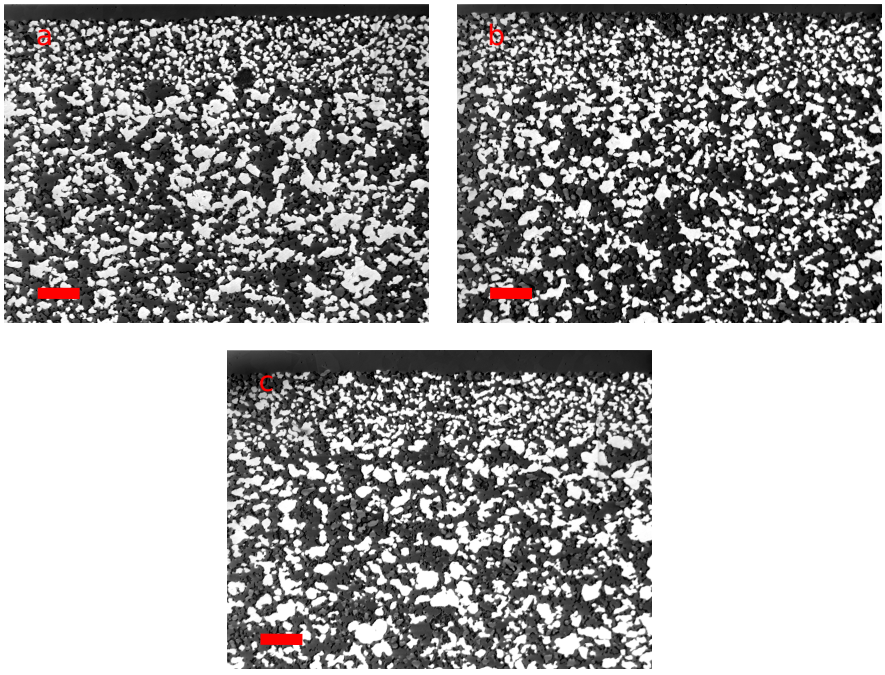

Figure S.5.7: LV SEM of a reference cell after reduction (a), the tested reference cell after 2350 h (b), and the repaired cell after 2350 h (c). The scalebar is 10 μm.

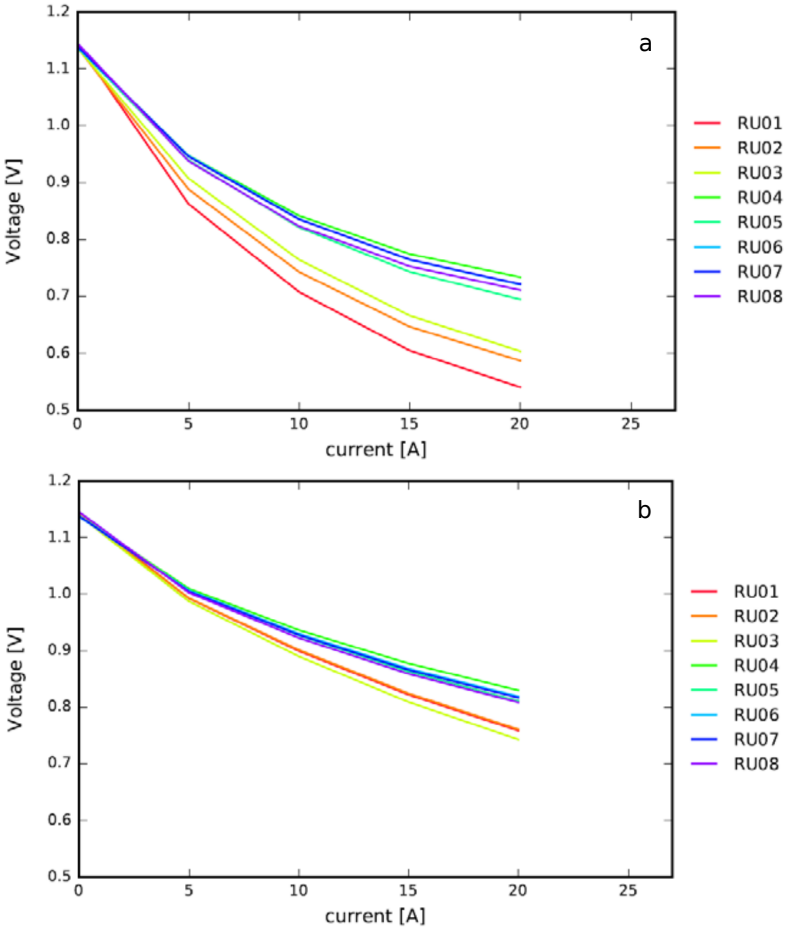

Figure S.5.8: IV curves of each RU of the stack in SOFC mode with 60%/40% H_2/N_2 at 700 °C, before (a) and after (b) infiltration.

5.8 References

1. Graves, C., Ebbesen, S. D., Mogensen, M. & Lackner, K. S. Sustainable hydrocarbon fuels by recycling CO_2 and H_2O with renewable or nuclear energy. *Renewable and Sustainable Energy Reviews* **15,** 1–23 (Jan. 2011).
2. Skafte, T. L., Hjelm, J., Blennow, P. & Graves, C. Quantitative review of degradation and lifetime of solid oxide cells and stacks. *EFCF 2016 proceedings,* B0501 (2016).
3. Hansen, J. B. Solid oxide electrolysis - a key enabling technology for sustainable energy scenarios. *Faraday Discuss.* **182,** 9–48 (2015).
4. Jiang, S. P. A review of wet impregnation - An alternative method for the fabrication of high performance and nano-structured electrodes of solid oxide fuel cells. *Materials Science and Engineering: A* **418,** 199–210 (Feb. 2006).
5. Vohs, J. M. & Gorte, R. J. High-Performance SOFC Cathodes Prepared by Infiltration. *Advanced Materials* **21,** 943–956 (Mar. 2009).
6. Ding, D., Li, X., Lai, S. Y., Gerdes, K. & Liu, M. Enhancing SOFC cathode performance by surface modification through infiltration. *Energy & Environmental Science* **7,** 552 (2014).
7. Jiang, S. P. Nanoscale and nano-structured electrodes of solid oxide fuel cells by infiltration: Advances and challenges. *International Journal of Hydrogen Energy* **37,** 449–470 (Jan. 2012).
8. Gorte, R. & Vohs, J. Nanostructured anodes for solid oxide fuel cells. *Current Opinion in Colloid & Interface Science* **14,** 236–244 (Aug. 2009).
9. Liu, Z. *et al.* Fabrication and modification of solid oxide fuel cell anodes via wet impregnation/infiltration technique. *Journal of Power Sources* **237,** 243–259 (Sept. 2013).
10. Verbraeken, M. C. *et al.* Short Stack and Full System Test Using a Ceramic A-Site Deficient Strontium Titanate Anode. *Fuel Cells* **15,** 682–688 (Oct. 2015).
11. Kiebach, R. *et al.* Infiltration of SOFC Stacks: Evaluation of the Electrochemical Performance Enhancement and the Underlying Changes in the Microstructure. *Fuel Cells* **16,** 80–88 (Feb. 2016).
12. Njodzefon, J. C. *Electrode Kinetics and Gas Conversion in Solid Oxide Cells* PhD thesis (Technical University of Denmark, 2015).
13. Graves, C. *RAVDAV data analysis software, version 0.9.8.* 2015.
14. Thyden, K. *Microstructural degradation of Ni-YSZ anodes for solid oxide fuel cells* Ph.D. thesis (Technical University of Denmark, 2008).

15. Rass-hansen, J. *et al.* Topsoe Stack Platform (TSP) - A robust stack technology for solid oxide cells. *EFCF 2016 proceedings,* A1508 (2016).

16. Duboviks, V. *et al.* Carbon deposition behaviour in metal-infiltrated gadolinia doped ceria electrodes for simulated biogas upgrading in solid oxide electrolysis cells. *Journal of Power Sources* **293,** 912–921 (2015).

17. Graves, C. & Hjelm, J. Advanced impedance modeling of solid oxide electrochemical cells. *EFCF 2014 proceedings,* B1203 (2014).

18. Hansen, K. V. *et al.* Effects of Strong Cathodic Polarization of the Ni-YSZ Interface. *Journal of The Electrochemical Society* **163,** F1217–F1227 (2016).

19. Tao, Y., Ebbesen, S. D. & Mogensen, M. B. Carbon Deposition in Solid Oxide Cells during Co-Electrolysis of H_2O and CO_2. *Journal of the Electrochemical Society* **161,** F337–F343 (Jan. 2014).

20. Tao, Y., Ebbesen, S. D., Zhang, W. & Mogensen, M. B. Carbon Nanotube Growth on Nanozirconia under Strong Cathodic Polarization in Steam and Carbon Dioxide. *ChemCatChem* **4000** (Feb. 2014).

21. Skafte, T. L., Graves, C., Blennow, P. & Hjelm, J. Carbon Deposition during CO_2 Electrolysis in Ni-Based Solid-Oxide-Cell Electrodes. *ECS Transactions* **68,** 3429–3437 (2015).

22. Skafte, T. L., Graves, C., Blennow, P. & Hjelm, J. Carbon deposition and sulfur poisoning during CO_2 electrolysis in Ni-based solid-oxide-cell electrodes. *In manuscript* (2017).

23. Hauch, A., Brodersen, K., Chen, M. & Mogensen, M. Ni/YSZ electrodes structures optimized for increased electrolysis performance and durability. *Solid State Ionics* **293,** 27–36 (Oct. 2016).

24. Primdahl, S. Gas Diffusion Impedance in Characterization of Solid Oxide Fuel Cell Anodes. *Journal of The Electrochemical Society* **146,** 2827 (1999).

25. Nielsen, J., Klemensø, T. & Blennow, P. Detailed impedance characterization of a well performing and durable Ni:CGO infiltrated cermet anode for metal-supported solid oxide fuel cells. *Journal of Power Sources* **219,** 305–316 (Dec. 2012).

26. Jacobsen, T., Hendriksen, P. V. & Koch, S. Diffusion and conversion impedance in solid oxide fuel cells. *Electrochimica Acta* **53,** 7500–7508 (2008).

6 Conclusions

As outlined in chapter 1, the SOC technology will lead to a number of beneficial effects for society. To reach wide-spread deployment it will be necessary to utilize economies of scale, which will be possible once market penetration has occurred. By increasing the lifetime of SOCs we can accelerate the technology towards the market and increase the probability of achieving these advantages. However, the devices often fail due to unintended interruptions of operation or by a too high rate of degradation. The current international status of lifetime was elucidated in chapter 2 by quantifying information published in literature within the field. Fortunately, by working on the many mechanisms leading to the high degradation rate, it was shown that the technology is approaching the targets required for commercialization. The progress can be accelerated further by focusing on specific markets, operating modes and mechanisms. This concept was applied in the remaining parts of the project.

A specific operating mode, the conversion of CO_2 to CO, has been identified as cost-competitive within a niche market. This then constitutes a possible route to market with a low barrier for entry. The efficiency of the operating mode is however thermodynamically limited due to a specific mechanism inherent to the state-of-the-art electrocatalyst utilized, namely carbon formation on Ni. In chapter 3 we devised a technique to map out the limited operating window, and thereby maximize the potential efficiency. The results were confirmed by two independent multi-physics models developed by colleagues. By combining the findings with multi-physics model simulations of whole stacks, it was found that the possible output CO concentration can in practice be up to 50% lower than expected based on the thermodynamic carbon deposition threshold at the inlet temperature, depending on the specific design and operation strategy. To successfully address the issue by modifying the material turned out to be challenging, and it is possible that the most cost-effective solution is to entirely replace the Ni in the electrode.

Ceria has shown promising tolerance and performance in both literature and in earlier studies by the authors. In chapter 4 we examined the differences in carbon forming mechanisms between the common-place Ni-YSZ electrode structure and ceria with and without Ni. This was carried out using *operando* NAPXPS on model electrodes. We studied novel electrochemically driven carbon formation

reactions and elucidated the fundamental mechanisms. We found that carbon formation on ceria is indeed inhibited and proceeds through multiple steps involving intermediate species such as carbonate and oxidized carbon groups. Meanwhile, electrochemical carbon formation on Ni-YSZ occurred without such intermediate carbonate and oxidized carbon species. We furthered the current understanding of the underlying reasons for the increased tolerance of ceria by suggesting based on the data that the formation and presence of various C-O species on the ceria surface hinders the formation of solid carbon. Lastly, we found that a thin amorphous carbon layer tends to form on ceria, which is far less destructive in a porous electrode than the CNTs formed at the Ni/YSZ interface. The results are naturally also of interest to other modes of operation where carbon formation is an issue, or to other technologies where carbon deposition might even be desired.

After focusing on a specific mechanism at several different scales, in chapter 5 we zoomed back out. Returning to developing mitigation strategies for degradation and failure mechanisms in general, we succeeded in applying a well-known electrode modifying technique in a novel manner. We fully reactivated the electrode by means of infiltration after degradation or otherwise unintented operation interruptions had occurred. Firstly, we tied the study back to chapter 3 and chapter 4 by fully restoring the performance of a cell degraded by carbon formation. Secondly, we showed that the method was applicable to other failure mechanisms, and thirdly, we underlined the promising potential by entirely eliminating degradation of the electrode over the course of nearly 2500 h. Lastly, the technique was applied on stack level with similar promising results.

6.1 Outlook

The greatest compliment you can get for the work that you do, is that others are willing to devote themselves to it and continue it. I hope the studies presented here can motivate further examination.

With additional data for the quantitative analysis of lifetime and degradation, it may be possible to more accurately identify the primary causes for the early failure of the devices. With a larger dataset, machine learning could be applied to examine links between failure and mechanisms that is not obvious by human inspection.

The correlation of specific operating parameters and carbon formation could be further investigated on stack level, although the degree of complexity increases dramatically. Moreover, the single-cell multi-physics models based on the discoveries could be incorporated into a multi-physics model of the TSP-1 stack already established at Haldor Topsoe A/S.

Similar studies of surface species involved in important degradation mechanisms could be carried out, e.g. poisoning of the surface with impurities. Regarding carbon formation, it would be interesting to examine the species involved in thermochemical reactions and compare them to the ones found for electrochemical reactions presented here. Furthermore, using for instance microscopic techniques, the rate of deposition could be investigated in more detail. Lastly, there are a vast amount of possibilities for alternative designs and materials for samples.

Lastly, there is great promise in extending the lifetime by continued reactivation of electrodes, either by the technique presented here or others like it. In regards to reactivation by means of infiltration, further optimization is possible, e.g. wetting capabilities, materials, amount, etc.

Nomenclature

pO_2	Partial oxygen pressure
2PB	Double-phase-boundary
3PB	Triple-phase-boundary
ASR	Area-specific resistance
BE	Binding energy
BSE	Backscattered electrons
CE	Counter-electrode
CGO	Gadolinium-doped ceria
CNT	Carbon nanotubes
DRT	Distribution of relaxation times
EIS	Electrochemical impedance spectroscopy
EoL	End-of-Life
FU	Fuel utilization
FWHM	Full-width-half-maximum
IC	Interconnect
KE	Kinetic energy
LSCF	Lanthanum-strontium-cobalt-ferrite-oxide
LSM	Lanthanum-strontium-manganese-oxide
LV-SEM	Low-voltage scanning electron microscopy

MIEC	Mixed ionic- and electronic conductivity
NAPXPS	Near-ambient pressure x-ray photoelectron spectroscopy
Ni	Nickel
OCV	Open-circuit voltage
PLD	Pulsed-laser deposition
QA	Quality assurance
RU	Repeating unit
RWGS	Reverse water gas shift
SDC	Samarium-doped ceria
SE	Secondary electrons
SEM	Scanning electron microscope
SERS	Surface-enhanced Raman spectroscopy
SOC	Solid oxide cell
SOEC	Solid oxide electrolysis cell
SOFC	Solid oxide fuel cell
TSP-1	Topsoe stack platform
V_{tn}	Thermoneutral voltage
VBM	Valence band maximum
WE	Working-electrode
XPS	X-ray photoelectron spectroscopy
YSZ	Yttria-stabilized zirconia